

NASA TECHNICAL NOTE



NASA TN D-5498

NASA TN D-5498

01
1007 OCT 1969
RESEARCH CENTER
RESEARCH CENTER



**HYPERSONIC AERODYNAMIC
CHARACTERISTICS OF TWO DELTA-WING
X-15 AIRPLANE CONFIGURATIONS**

*by Theodore J. Goldberg, Jerry N. Hefner,
and David R. Stone*

*Langley Research Center
Langley Station, Hampton, Va.*

NATIONAL AERONAUTICS AND SPACE ADMINISTRATION • WASHINGTON, D. C. • OCTOBER 1969



0132137

1. Report No. NASA TN D-5498	2. Government Accession No.	3. Recipient's Catalog No.	
4. Title and Subtitle HYPERSONIC AERODYNAMIC CHARACTERISTICS OF TWO DELTA-WING X-15 AIRPLANE CONFIGURATIONS		5. Report Date October 1969	6. Performing Organization Code
7. Author(s) Theodore J. Goldberg, Jerry N. Hefner, and David R. Stone		8. Performing Organization Report No. L-6489	10. Work Unit No. 722-01-10-09-23
9. Performing Organization Name and Address NASA Langley Research Center Hampton, Va. 23365		11. Contract or Grant No.	13. Type of Report and Period Covered Technical Note
12. Sponsoring Agency Name and Address National Aeronautics and Space Administration Washington, D.C. 20546		14. Sponsoring Agency Code	
15. Supplementary Notes			
16. Abstract An investigation of the hypersonic aerodynamic characteristics of two delta-wing X-15 research configurations was conducted at a Mach number of 6 and a Reynolds number of 2.71×10^7 per meter (8.27×10^6 per ft). Limited tests of one model were also made at a Mach number of 8. Results are presented to show the aerodynamic effects of wing geometry and longitudinal position, wing fins, nose cant, strakes, speed brakes, and a suspended test ramjet. The type of boundary layer ahead of the elevons was determined from oil-flow studies of the separation boundaries with and without boundary-layer trips. Experimental aerodynamic characteristics are compared with analytical estimates.			
17. Key Words Suggested by Author(s) X-15 airplane Hypersonic aerodynamic characteristics Boundary-layer trips Wing fins, strakes, speed brakes, ramjet Nose cant		18. Distribution Statement Unclassified - Unlimited	
19. Security Classif. (of this report) Unclassified	20. Security Classif. (of this page) Unclassified	21. No. of Pages 102	22. Price* \$3.00

HYPERSONIC AERODYNAMIC CHARACTERISTICS OF TWO DELTA-WING X-15 AIRPLANE CONFIGURATIONS

By Theodore J. Goldberg, Jerry N. Hefner,
and David R. Stone
Langley Research Center

SUMMARY

An investigation of the hypersonic aerodynamic characteristics of two 1/50-scale delta-wing X-15 research airplane configurations has been conducted at a Mach number of 6 and a free-stream Reynolds number of 2.71×10^7 per meter (8.27×10^6 per ft). Limited tests of one model were also made at a Mach number of 8 and a free-stream Reynolds number of 3.43×10^7 per meter (10.4×10^6 per ft). Longitudinal data were obtained at angles of attack from -6° to 19° , and lateral and directional data were obtained at sideslip angles of 0° and -3.8° . The effects of wing geometry and longitudinal position, wing fins, nose cant, strakes, speed brakes, and a suspended test ramjet were investigated at elevon deflection angles to -45° . The type of boundary layer ahead of the elevons was determined from oil-flow studies of the separation boundaries with and without boundary-layer trips.

The results of this investigation showed that the first configuration (flat-bottom, positive-camber, 76° delta wing on a modified X-15 fuselage with wedge-shaped vertical tails and a 10° included wedge angle) was directionally unstable without either tip fins or a large lower vertical tail. This model also required large elevon deflection angles to trim, which reduced the maximum trimmed lift-drag ratio. Increasing the Mach number from 6 to 8 had essentially little effect on the aerodynamic characteristics. In order to decrease the large elevon deflection angles necessary to trim and to increase the lateral-directional stability, the delta wing and center-line vertical tails of the initial configuration were modified and incorporated into the second configuration. In addition, the wing fins of this revised configuration were moved to an inboard position. The second configuration (flat-top, negative-camber, 72.8° delta wing and enlarged vertical tails) attained a maximum trimmed lift-drag ratio of 3.9 and was directionally stable without inboard fins.

INTRODUCTION

Prior to the termination of the X-15 program in 1968 a study was made of configurations with a delta wing for improved lift-drag ratio and with provisions for wing fins and a small hypersonic research ramjet engine. During this study, two configurations were generated. The first configuration, a preliminary version, was intended to define problem areas in performance, stability, and control. The second configuration contained modifications designed to improve hypersonic performance, longitudinal control capability, and directional stability. These modifications included wing planform and airfoil section changes, revisions in vertical-tail geometry, and the use of nose strakes and nose cant. Experimental and analytical aerodynamic data were obtained for both configurations at Mach 6, and limited experimental data were obtained for the first configuration at Mach 8. The aerodynamic characteristics of these configurations and their modifications are presented herein. Comparisons of the experimental aerodynamic characteristics with analytical estimates are also included.

The type of boundary layer ahead of the elevons for this investigation was determined from oil-flow studies of the separation boundaries with and without boundary-layer trips. The boundary-layer trips assured a turbulent boundary layer ahead of the elevons. A few force tests were also made with boundary-layer trips to determine their effect on configuration aerodynamics. For the Mach 6 investigation, the free-stream Reynolds number was 2.71×10^7 per meter (8.27×10^6 per ft), the angle of attack varied from -4° to 16° , and the sideslip angles were 0° and -3.8° ; for the Mach 8 investigation, the free-stream Reynolds number was 3.43×10^7 per meter (10.4×10^6 per ft), the angle of attack varied from -6° to 19° , and the sideslip angles were 0° and -3.7° .

SYMBOLS

The longitudinal forces and moments are referenced to the stability-axis system, and the lateral forces and moments are referenced to the body-axis system. The body- and stability-axis systems are illustrated in figure 1. The center of moments, unless otherwise specified, is on the X-axis at 40 percent wing mean aerodynamic chord. Weight and balance studies indicate this to be a realistic location of the center of gravity.

b wing span

C_D drag coefficient, $\frac{\text{Drag}}{q_\infty S}$

C_L lift coefficient, $\frac{\text{Lift}}{q_\infty S}$

C_N	normal-force coefficient, $\frac{\text{Normal force}}{q_\infty S}$
C_Y	side-force coefficient, $\frac{\text{Side force}}{q_\infty S}$
$C_{Y\beta}$	side-force stability parameter at $\beta = 0^\circ$, $\frac{\Delta C_Y}{\Delta\beta}$, per degree
$C_{Y\delta'_E}$	rate of change of side-force coefficient with differential elevon deflection, $\frac{\Delta C_Y}{\Delta\delta'_E}$
$C_{Y\delta'_V}$	rate of change of side-force coefficient with vertical-tail deflection, $\frac{\Delta C_Y}{\Delta\delta'_V}$
C_l	rolling-moment coefficient, $\frac{\text{Rolling moment}}{q_\infty S b}$
$C_{l\beta}$	effective-dihedral parameter at $\beta = 0^\circ$, $\frac{\Delta C_l}{\Delta\beta}$, per degree
$C_{l\delta'_E}$	rate of change of rolling-moment coefficient with differential elevon deflection, $\frac{\Delta C_l}{\Delta\delta'_E}$
$C_{l\delta'_V}$	rate of change of rolling-moment coefficient with vertical-tail deflection, $\frac{\Delta C_l}{\Delta\delta'_V}$
C_m	pitching-moment coefficient, $\frac{\text{Pitching moment}}{q_\infty S \bar{c}}$
$C_{m,0}$	pitching-moment coefficient at zero lift
$\frac{\partial C_m}{\partial C_L}$	rate of change of pitching moment with lift coefficient
$\frac{\partial C_m}{\partial C_N}$	rate of change of pitching moment with normal-force coefficient
C_n	yawing-moment coefficient, $\frac{\text{Yawing moment}}{q_\infty S b}$
$C_{n\beta}$	directional stability parameter at $\beta = 0^\circ$, $\frac{\Delta C_n}{\Delta\beta}$, per degree
$C_{n\delta'_E}$	rate of change of yawing-moment coefficient with differential elevon deflection, $\frac{\Delta C_n}{\Delta\delta'_E}$

$C_{n\delta_V}$	rate of change of yawing-moment coefficient with vertical-tail deflection, $\frac{\Delta C_n}{\Delta \delta_V}$
C_p	pressure coefficient, $\frac{p - p_\infty}{q_\infty}$
\bar{c}	mean aerodynamic chord of wing
L/D	lift-drag ratio
M	Mach number
p	static pressure
p_t	stagnation pressure
q	dynamic pressure
R	Reynolds number based on free-stream conditions
S	total wing area including area within body and side fairings
T_t	stagnation temperature
X,Y,Z	body axes
X_S, Y_S, Z_S	stability axes
x,y	longitudinal and lateral distances, respectively
α	angle of attack
β	angle of sideslip
δ	deflection angle
δ_E	elevon deflection angle (positive when trailing edge is deflected down)
δ'_E	differential elevon deflection angle (positive to produce positive rolling moment), $\delta_{E,L} - \delta_{E,R}$

δ_N	nose cant angle
$\delta_{N,1}$	nose cant angle from $x = 4.22$ cm (1.66 in.)
$\delta_{N,2}$	nose cant angle from $x = 11.51$ cm (4.53 in.)
δ_{SB}	speed-brake deflection angle

Subscripts:

av	average
L	left
max	maximum
R	right
T	trim
∞	free stream

Model component designations:

B	fuselage, including canopy
B ₂	fuselage with strakes, including canopy
E ₂	elevons with W ₂
E ₃	elevons with W ₃
V _L	small lower vertical tail, without movable part
V _{L,2}	small lower vertical tail, with movable part
V _{L,6}	large lower vertical tail, without movable part
V _{L,B}	V _L with speed brakes deflected

$V_{L,6B}$	$V_{L,6}$ with speed brakes deflected
V_P	pylon
$V_{R,C}$	ramjet configuration with spike closed
$V_{R,O}$	ramjet configuration without spike
V_T	tip fin for model 1
$V_{T,3}$	tip fin with wing in forward position for model 1
$V_{T,4}$	tip fin with wing in midposition for model 1
$V_{T,6}$	inboard fin with 0° toe-in for model 2
$V_{T,7}$	inboard fin with 5° toe-in for model 2
V_U	small upper vertical tail
$V_{U,2}$	large upper vertical tail
$V_{U,B}$	V_U with speed brakes deflected
$V_{U,2B}$	$V_{U,2}$ with speed brakes deflected
W_2	flat-bottom, 76° swept delta wing for model 1
W_3	flat-top, 72.8° swept delta wing with -10° dihedral for model 2
X_2	side fairing with W_2
X_3	side fairing with W_3

APPARATUS AND METHODS

Models

Drawings of the delta-wing models and the various components used for the present tests are shown in figures 2 and 3. The fuselage for both models is similar to the X-15

(ref. 1) except for an increase in the length of the cylindrical part to provide additional fuel capacity and a change in the forward fuselage to a 10° half-angle cone. Model 1 has a flat-bottom, positive-camber, 76° delta wing with circular arcs on the forward and rearward parts of the upper surface. The center-line upper and lower vertical tails are wedges each having a 10° included angle. Model 2 has a flat-top, negative-camber, 72.8° delta wing with a -10° dihedral. The lower surface of the 72.8° delta wing consists of five flat-surface planes at the root and four at the tip. The center-line upper and lower vertical tails of model 2 have 12° and 15° included wedge angles, respectively. Trapezoidal elevons are incorporated in both delta wings to provide pitch control. Details of the wings are presented in figures 2(c) and 3(b). Both wings have a thickness-chord ratio of 0.03 at the root and 0.05 at the tip and a constant leading-edge radius of 0.038 cm (0.015 inch). Both wings were tested with wing fins – tip fins on model 1 and inboard fins on model 2. (See figs. 2(d) and 3(b).) Both models were tested with the wings in at least two longitudinal positions in order to assure proper wing placement with or without a test ramjet. These wing positions along with other geometric characteristics of both models are given in table I. A ramjet with a spike to simulate a closed inlet (no flow through the engine) and without a spike to simulate an open inlet (when the flow is swallowed) replaced the lower vertical tail for some tests. Details of the ramjet and pylon are given in figures 2(e) and 3(c), and their locations can be seen in figures 2(b) and 3(c). The pylon for model 2 was the same as that for model 1 except that it was extended 1.285 cm (0.506 in.) to be flush with the base of the fuselage. Details of speed brakes, strakes, and canted noses which were tested on model 2 are shown in figure 3(c). A photograph of model 1 with the wing in the midposition in the Langley 20-inch Mach 6 tunnel is shown as figure 4.

Wind Tunnels

The Mach 6 tests were conducted in the Langley 20-inch Mach 6 tunnel, which is a blowdown type exhausting into the atmosphere and has a two-dimensional nozzle and a test section 52.1 cm (20.5 in.) high and 50.8 cm (20 in.) wide. More detailed descriptions of this tunnel are presented in references 2 and 3.

The Mach 8 tests were conducted in the Langley Mach 8 variable-density hypersonic tunnel. This tunnel, described in reference 3, is a blowdown type capable of exhausting into a vacuum sphere or the atmosphere. It has an axially symmetric contoured nozzle and a test-section diameter of 45.7 cm (18 in.).

Tests

Tests at Mach 6 were conducted at a stagnation pressure of 3 MN/m^2 (435 psia) and a stagnation temperature of 478° K (400° F). The corresponding free-stream Reynolds

number was 2.71×10^7 per meter (8.27×10^6 per ft). Force data were obtained for both models over an angle-of-attack range from -4° to 16° and at angles of sideslip of 0° and -3.8° . Elevon deflections were varied from 5° to -45° for model 1 and from 10° to -30° for model 2. The investigation at Mach 6 included the effects of longitudinal wing shift, wing fins, ramjet, nose cant, strakes, and speed brakes.

Limited Mach 8 tests were conducted at $M_\infty = 8.06$ with a total pressure of 17.3 MN/m^2 (2510 psia), total temperature of 810° K (1000° F), and free-stream Reynolds number of 3.43×10^7 per meter (10.4×10^6 per ft). Force data at Mach 8.06 were obtained only for model 1 with the wing in the midposition, with tip fins, and without the lower movable vertical tail. The angle of attack was varied from -6° to 19° for angles of sideslip of 0° and -3.7° . Elevon deflection angles were varied from 0° to -45° .

Methods

Force and moment data were obtained by use of a six-component strain-gage balance housed inside the model. For tests in the Mach 6 facility, the model was mounted in the tunnel test section on a movable support system which was pneumatically driven through an angle of attack during the run for each test point. Angles of sideslip were obtained by offsetting the model support system to the desired angle; thus, the data were obtained at an essentially constant sideslip angle over the angle-of-attack range. The true angles of attack and sideslip were set optically by the use of a point source of light and small lens-prism mounted on the model behind the fuselage side fairing. The image of the light source was reflected by the prism and focused by the lens onto a calibrated chart. The Mach number was obtained for each test point with a total-pressure probe located in a position to avoid interference from the model bow shock. The Mach number variation for this facility is discussed in reference 4.

For tests in the Mach 8 facility, the model was connected to a sting support system which was manually adjusted to the desired angle of attack and angle of sideslip prior to each run. The true angles of attack and sideslip for each test point were measured on a comparator from photographs of the model taken through the test-section top and side windows across which wires were stretched for reference angles. The Mach number used to reduce the present data was obtained from a total-pressure survey across the tunnel at the model nose location for the total pressure and temperature used in this investigation. The Mach number distribution obtained from the ratio of pitot pressure to total pressure is presented in figure 5.

For tests in both facilities, straight line slopes between the basic data at the two sideslip angles were used to obtain the lateral and directional stability parameters. Model base pressures were measured during each test, and the axial-force component

was adjusted to correspond to a base pressure equal to free-stream static pressure. The average of two base-pressure tubes, one on the top and one on the bottom of the sting, were used for all tests.

An oil-flow technique was employed to examine the separation boundaries ahead of the elevons. A mixture of silicone oil and lampblack was distributed over the model surface in random dots of various sizes. To insure turbulent boundary layers ahead of the elevons, some tests were made with boundary-layer trips. These trips consisted of one row of 0.119-cm-diameter (0.0468 in.) spheres spaced 0.508 cm (0.2 in.) apart and located a perpendicular distance of 0.635 cm (0.25 in.) from the leading edge of the wing of model 1. Thirty roughness elements were located on each semispan upper and lower surface of the delta wing. In addition, a band of seven 0.119-cm-diameter (0.0468 in.) spheres were equally spaced around the fuselage 1.27 cm (0.5 in.) from the nose.

Accuracy

On the basis of accuracy in balance calibration, zero shift of the balance during tests, computer readout, dynamic pressure, and pressure transducers, the probable uncertainties in the force and moment coefficients are estimated by the method of least squares as follows:

	Mach 6 tests	Mach 8 tests
C_L	± 0.003	± 0.005
C_D	± 0.0007	± 0.0008
L/D	± 0.15	± 0.27
C_m	± 0.0003	± 0.0006
C_{l_β}	± 0.0001	± 0.0001
C_{n_β}	± 0.0002	± 0.0003
C_{Y_β}	± 0.0008	± 0.0015

The accuracy of the angles of attack and sideslip is estimated to be $\pm 0.1^\circ$ for the Mach 6 tests and to be $\pm 0.1^\circ$ and 0.25° , respectively, for the Mach 8 tests. The free-stream Mach number is estimated to be accurate to ± 0.02 for tests at both Mach numbers.

RESULTS AND DISCUSSION

Type of Boundary Layer

Previous studies have indicated that airplanes similar to the present models operating at Mach numbers up to at least 6 would have turbulent boundary layers ahead of the control surfaces. In order to determine the type of boundary layer for this wind-tunnel investigation, oil-flow studies were made both with and without roughness elements on

model 1. The criteria used to determine the type of boundary layer were the elevon deflection angle necessary for separation and the extent of separation ahead of the elevon.

Typical oil-flow patterns are shown in figure 6. These oil-flow photographs at Mach 6 and 8 (figs. 6(a) and 6(d)) show that without roughness very little, if any, separation occurs for elevon deflection angles to -25° at $\alpha = 0^\circ$ except possibly near the tip. This occurrence indicates transitional or turbulent flow just ahead of the elevon, since previous studies (refs. 2, 5, and 6) have shown that a laminar boundary layer will separate at deflection angles of approximately 10° (fig. 7) for similar Reynolds numbers. (Although the data of fig. 7 are for a flat plate, separation studies with delta wings (refs. 7, 8, and 9) have shown similar trends.)

Roughness elements, which increased the effective local Reynolds number, were used to insure a turbulent boundary layer ahead of the elevons. The required roughness size, shape, and location were determined from unpublished data taken with a 77° delta wing having a 0.0762-cm (0.030 in.) leading-edge diameter in the same Mach 6 facility used in the present investigation. At the higher effective Reynolds number obtained with the roughness elements, the extent of separation increased. (See figs. 6(b) and 6(d).) This result indicates that without roughness the boundary layer was already turbulent because if the boundary layer was transitional, the extent of separation would have decreased with increasing Reynolds number. (See fig. 7.)

At an angle of attack as small as 4° the flow apparently separated off the lee surface after remaining attached for only a very short distance. (See fig. 6(c).) This type of separation has been observed in reference 7. Much of the elevon, even at $\delta_E = -15^\circ$, was buried in this separated flow although the elevon itself does not induce the separation. The addition of roughness elements appeared to have no effect on the separation off the lee surface at an angle of attack of 6° as seen in figure 6. Since the flow remained attached for only a short distance from the leading edge, it must be assumed that the boundary layer ahead of the separation was laminar. However, in this type of separated flow off the lee surface, very little is known quantitatively about the boundary layer.

Another indication of the type of boundary layer was obtained from previous investigations of transition on delta wings. The transition data in reference 7 were obtained in the same facility as the present tests and indicate, on the basis of an estimated local transition Reynolds number, that at $\alpha \leq 15^\circ$ the boundary layer on the windward surface just ahead of the elevon of model 1 was turbulent. Results from reference 10 indicate that the same conclusions apply to the type of boundary layer for the present tests at $M_\infty = 8$. Although this conclusion was based on results obtained with sharp leading-edge models, references 11 and 12 have shown that for the same unit Reynolds number, blunting the leading edge on a delta wing will cause transition to occur farther upstream.

More recent work (ref. 13) discusses the interference effects on the transition Reynolds number at a delta wing-body junction.

In summary, the boundary layer just ahead of the elevons was turbulent, even without boundary-layer trips, for both wing surfaces at $\alpha = 0^\circ$ and for the windward surface at angles of attack. Therefore, roughness elements were used only for a few force tests to assess their effect on configuration aerodynamics.

Aerodynamic Characteristics

The results of this experimental investigation are presented in figures 8 to 20 in the form of plots comparing the effects of component parts, wing location, elevon deflections, nose cant, strakes, speed brakes, Mach number, and center-of-gravity location on the aerodynamic characteristics. Computer drawings that were used in making analytical estimates are shown in figure 21. A comparison of the experimental data with analytical estimates from a computer program is presented in figures 22 to 24. In addition, the detailed data used in developing these figures are presented in figures 25 to 40. For convenience in locating these various effects for both models, an index to these measured data is presented in table II.

Model 1 at $M_\infty = 6$. - The results for model 1 at $M_\infty = 6$ indicate several problem areas. These include relatively low values of maximum trimmed L/D (fig. 8), large negative elevon deflections necessary for trim (fig. 8), and directional instability of the basic configuration, $BX_2W_2E_2V_UV_L$, (fig. 25). The maximum trimmed L/D was 3.4 with the wing in the midposition (fig. 8). This value was achieved for the configurations which had either the movable lower vertical tail or tip fins, and both of these configurations were directionally stable. (Calculations indicate that removing either the movable part of the lower vertical tail or the tip fins to achieve the basic configuration ($BX_2W_2E_2V_UV_L$) increases maximum trimmed L/D to 3.75; however, this configuration is directionally unstable.) The low value of trimmed L/D was primarily the result of the large elevon deflection angles required to trim. These elevon deflection angles resulted from a negative $C_{m,0}$ (fig. 9(b)), a large rate of change of pitching moment with angle of attack (fig. 9(b)), and the low elevon effectiveness (fig. 26) due in part to the flow separation on the wing lee surface as previously discussed.

All configurations tested exhibited negative dihedral effect ($+C_{l\beta}$) under trimmed conditions. (See fig. 8.) As expected, the configuration with the movable lower vertical tail produced the largest negative dihedral effect especially at the higher angles of attack. The negative dihedral effect for the configuration with tip fins resulted because the center line of the symmetrical tip fin is located 0.1588 cm (0.0620 in.) below the center of gravity, as noted in figure 2(a). Moving the tip-fin center line up to the X-Y plane would

eliminate the negative dihedral effect for even the worst case, $BX_2W_2E_2V_UV_{L,2}V_T$, at trim conditions as shown in figure 8.

Model 1 at $M_\infty = 8$.- Increasing the Mach number from 6 to 8 had essentially little effect on the trimmed characteristics of model 1 ($BX_2W_2E_2V_UV_{L,2}V_T$) as seen in figure 11. With increased Mach number the maximum trimmed L/D and the longitudinal stability remained unchanged (fig. 12(a)), and the directional stability was reduced (fig. 11).

Model 2 at $M_\infty = 6$.- For model 2 the delta wing and center line vertical tails of model 1 were modified to decrease the negative elevon trim requirements and increase the lateral-directional stability of the basic configuration. The wing airfoil was redesigned to have a flat-top, negative-camber section to produce a more positive $C_{m,0}$. To provide directional stability without the need for wing fins, a -10° dihedral was added to the wing, and both the areas and wedge angles of the vertical tails were increased. The tip fins were moved inboard to make the configuration more representative of currently envisioned hypersonic cruise vehicle design and to relieve structural loads. Nose cant and strakes along the forward fuselage were tested as methods of decreasing the trim penalty in maximum trimmed L/D . The wing area and planform were changed as a result of subsonic (landing) considerations.

In general, the modifications significantly improved the performance as can be seen from the trimmed aerodynamic characteristics for model 2 at $M_\infty = 6$ in figures 14 to 17. The basic configuration ($BX_3W_3E_3V_U,2V_{L,6}$) with elevon deflection angles of approximately -5° produced a maximum trimmed L/D of 3.9. (See fig. 14(a).) These results were essentially independent of wing position. The increase in maximum trimmed L/D of model 2 over that of model 1 was a result of the positive $C_{m,0}$ produced by the wing of model 2, coupled with the essentially unchanged longitudinal stability (fig. 18(a)) which resulted in trim at angles of attack closer to maximum L/D . The larger vertical tails ($V_U,2$ and $V_{L,6}$) reduced the untrimmed maximum L/D of model 2 only by about 0.25 from that obtained with V_U and V_L (fig. 19(a)) but significantly increased $C_{n\beta}$ (fig. 19(b)). This increase resulted in directional stability for the basic configuration of model 2 with the wing in the aft position at angles of attack below about 8° . The inboard fins reduced the maximum trimmed L/D of model 2 approximately 17 percent (fig. 14(a)) but significantly increased the directional stability as indicated by the limited lateral-directional data obtained at $\delta_E = 0^\circ$ (figs. 14(b) and 19(b)). Replacing the lower vertical tail with the ramjet ($BX_3W_3E_3V_U,2V_{R,O}$) decreased the maximum trimmed L/D by approximately 11 percent and slightly increased the directional stability. (See fig. 14.) In the event the ramjet had to be ejected, the directional stability of the configuration with the pylon alone ($BX_3W_3E_2V_U,2V_P$) would be reduced. (See fig. 19(b).)

Both nose cant and strakes decreased the negative elevon deflection angles required to trim model 2 (figs. 15 to 17), but because the elevon deflections required to trim the basic configuration were already small ($\delta_E \approx -5^\circ$), the maximum trimmed L/D was increased only slightly. Strakes decreased the longitudinal stability at all angles of attack, whereas nose cant decreased it only at the higher angles of attack.

A summary of the stability and control-deflection variations at maximum trimmed L/D with center-of-gravity location and longitudinal wing position is presented for selected configurations in figure 20.

Effect of roughness elements on model 1 at $M_\infty = 6$.- To assess the effect of boundary-layer trips on configuration aerodynamics, force data were also obtained with roughness elements located on the delta wing and nose of the same configuration of model 1 used in the oil-flow studies. The addition of roughness elements, which increased the effective local Reynolds number, had little effect on the longitudinal stability at $\delta_E = 0^\circ$ for all angles of attack at $M_\infty = 6$. (See fig. 13.) For angles of attack below 7° , the roughness had no effect on longitudinal stability, but it decreased both the elevon effectiveness and the drag coefficient. These changes were caused by increased separation over the elevons as a result of the higher effective local Reynolds number. (See fig. 6.) For $\delta_E < 0^\circ$, the effect of the roughness on the elevon effectiveness was reduced as the angle of attack was increased probably because the roughness was located in the separated region near the leading edge on the lee surface of the wing.

At $\delta_E = 0^\circ$, the measured drag of the configuration with roughness was increased 0.002 over most of the angle-of-attack range of this investigation. (See fig. 13.) In an attempt to separate the drag increase into the pressure drag of the roughness and skin friction due to the change in boundary layer, the method of reference 14 was used. As shown in this reference, the drag coefficient for spherical roughness elements is a very strong function of the ratio of roughness height to boundary-layer thickness. Since this ratio at the roughness location could not be determined accurately enough, the pressure-drag coefficient of the roughness could not be determined.

Comparison of Analytical and Experimental Aerodynamic Characteristics

A limited comparison is made of the present Mach 6 experimental data with analytical longitudinal, directional, and lateral stability and control characteristics computed by using the computer program of references 15 and 16. For the calculation of pressure forces in compression regions, tangent-wedge, tangent-cone, or two-dimensional shock-expansion theory was used; in expansion regions, either Prandtl-Meyer expansion or two-dimensional shock-expansion theory was used; and in the base regions, a value of pressure coefficient equal to $1/M^2$ was used. Free-stream conditions were used ahead of each component as a simple method of determining vehicle performance. To partly

account for the interference of the body on the wing, the local Mach number ahead of the wing was reduced to the average value in the conical flow field of the nose at zero angle of attack ($M_{\text{wing}} = 5.2$). Because the expansions of the flow field along the cylindrical body would increase the Mach number approaching the wing surface, the value of 5.2 probably represents a lower limit of Mach number for this flow field. No attempt was made to account for the mutual interference of any other components.

Since it was concluded that turbulent flow existed over a large part of the model, computations for skin friction were made for turbulent flow conditions from the leading edge. All skin-friction calculations, adiabatic wall conditions being assumed, were made according to the method outlined in reference 15 by using either Eckert's reference-temperature (T') method (ref. 17) or the Spalding-Chi (S-C) method (ref. 18). Typical examples of the computer drawings of the two configurations are presented in figure 21 and the number and size of the surface elements considered for these computations are indicated.

Configurations with zero elevon deflection.- A comparison of the computer program results with wind-tunnel data for a component buildup of model 1 is presented in figure 22. All characteristics of the body alone were predicted reasonably well by tangent-cone theory with the addition of T' turbulent skin friction. (See fig. 22(a).)

For the wing-body combination (fig. 22(b)), the two-dimensional theories gave better predictions than the tangent-cone theory when applied to the wing surface and based on free-stream conditions. Two-dimensional theories with an adjusted Mach number ahead of the wing ($M_{\text{wing}} = 5.2$) showed some improvement and were used for the rest of the calculations.

The two-dimensional theories applied to the wing gave reasonable agreement in longitudinal forces and pitching moment, but the yawing and rolling moments were not predicted very well. The use of Spalding-Chi theory, which has been added to the computer program in reference 19, for the prediction of turbulent skin friction resulted in a small increase in skin-friction drag for the wing-body combination. This difference is in agreement with the previously found differences in Spalding-Chi and Eckert T' heat transfer as given in reference 20 for adiabatic wall conditions. Therefore, the rest of the machine calculations used the Spalding-Chi theory.

A comparison of the computed and measured aerodynamic characteristics for the total configuration of model 1, either tangent-wedge or tangent-cone theory being applied to the vertical tails and tip fins, is shown in figures 22(c) and 22(d). Both theoretical methods predicted the longitudinal aerodynamic characteristics reasonably well; however, neither method consistently predicted the lateral-directional stability derivatives. Generally, the tangent-cone method applied to the vertical tails and tip fins of model 1 more accurately predicted all the aerodynamic characteristics except $C_{l\beta}$.

Calculations for model 2 with larger vertical tails than model 1 and inboard wing fins (BX₃W₃E₃V_{U,2}V_{L,6}V_{T,6}) are presented in figure 23. A comparison of the computed and measured characteristics indicated that the prediction of the longitudinal force characteristics was as good as that obtained for model 1. None of the methods predicted the pitching moment; therefore, the trimmed characteristics at $\delta_E = 0^\circ$ could not be predicted. The positive dihedral effect ($-C_{l\beta}$) was predicted for model 2 whereas the same method failed to predict the dihedral effect for model 1 for $\alpha > 4^\circ$. Therefore, it would seem that the prediction of $C_{l\beta}$ for model 2 was fortuitous. This same conclusion can apply to the prediction of $C_{n\beta}$.

Effect of elevon deflection.- The longitudinal aerodynamic characteristics of model 2 computed by using the tangent-wedge method for the vertical tails and tip fins are presented in figure 24 for positive and negative elevon deflections. The longitudinal forces were predicted as well for the positive elevon deflection as they were for zero elevon deflection. For increasing negative deflections the predicted force coefficients agreed less favorably with the measured coefficients. The maximum L/D was predicted reasonably well for elevon deflections between 10° and -10° . For all values of δ_E , the computed pitching moment not only failed to agree with the measured values, but the difference in the computed and measured pitching moment changed with each elevon deflection. Therefore, the trimmed characteristics could not be determined even after correcting the pitching moment to account for the difference in computed and measured values at $\delta_E = 0^\circ$.

CONCLUDING REMARKS

An investigation has been conducted to determine the hypersonic aerodynamic characteristics of two delta-wing X-15 research configurations at a Mach number of 6 and with limited tests of one configuration at a Mach number of 8. Effects of wing geometry and longitudinal position, wing fins, nose cant, strakes, speed brakes, and a suspended test ramjet engine were investigated at elevon deflections to -45° at angles of attack and sideslip. Oil-flow studies and estimates of transition Reynolds number indicated that the boundary layer just ahead of the elevons was turbulent on both the windward and leeward wing surfaces at zero angle of attack and on the windward surface at angles of attack.

The first configuration was directionally unstable without either a large lower vertical tail or tip fins. In addition, this configuration required large elevon deflection angles to trim, which greatly reduced the maximum trimmed lift-drag ratio. Increasing the Mach number from 6 to 8 had essentially little effect on the aerodynamic characteristics. The second configuration which had wing and vertical-tail modifications to remedy the problems of the initial configuration, attained a maximum trimmed lift-drag ratio of 3.9 with elevon deflection angles of about -5° and was directionally stable without inboard

wing fins. A comparison of analytical and experimental aerodynamic characteristics showed that the aerodynamic forces could be predicted reasonably well, but the predictions of longitudinal, lateral, and directional moments were not reliable.

Langley Research Center,
National Aeronautics and Space Administration,
Langley Station, Hampton, Va., August 4, 1969.

REFERENCES

1. Penland, Jim A.; and Fetterman, David E., Jr.: Static Longitudinal, Directional, and Lateral Stability and Control Data at a Mach Number of 6.83 of the Final Configuration of the X-15 Research Airplane. NASA TM X-236, 1960.
2. Sterrett, James R.; and Emery, James C.: Extension of Boundary-Layer-Separation Criteria to a Mach Number of 6.5 by Utilizing Flat Plates With Forward-Facing Steps. NASA TN D-618, 1960.
3. Schaefer, William T., Jr.: Characteristics of Major Active Wind Tunnels at the Langley Research Center. NASA TM X-1130, 1965.
4. Goldberg, Theodore J.; Ashby, George C., Jr.; and Hondros, James G.: Center-Line Pressure Distributions on Two-Dimensional Bodies With Leading-Edge Angles Greater Than That for Shock Detachment at Mach Number 6 and Angles of Attack up to 25°. NASA TN D-1793, 1963.
5. Sterrett, James R.; and Emery, James C.: Experimental Separation Studies for Two-Dimensional Wedges and Curved Surfaces at Mach Numbers of 4.8 to 6.2. NASA TN D-1014, 1962.
6. Goldberg, Theodore J.: Turbulent Separation Associated With Axisymmetric Flared Bodies. *J. Spacecraft Rockets (Eng. Notes)*, vol. 4, no. 11, Nov. 1967, pp. 1551-1553.
7. Whitehead, Allen H., Jr.; and Keyes, J. Wayne: Flow Phenomena and Separation Over Delta Wings With Trailing-Edge Flaps at Mach 6. *AIAA J.*, vol. 6, no. 12, Dec. 1968, pp. 2380-2387.
8. Keyes, J. Wayne; Goldberg, Theodore J.; and Emery, James C.: Turbulent Heat Transfer Associated With Control Surfaces at Mach 6. *AIAA J. (Tech. Notes)*, vol. 6, no. 8, Aug. 1968, pp. 1612-1613.
9. Meckler, Lawrence: Pressure Measurements at Mach 8 on an Aerodynamically Controllable Winged Re-Entry Configuration. FDL-TDR-64-124, U.S. Air Force, June 1965. (Available from DDC as AD620959.)
10. Deem, Ralph E.; and Murphy, James S.: Flat Plate Boundary Layer Transition at Hypersonic Speeds. *AIAA Paper No. 65-128*, Jan. 1965.
11. Jillie, Don W.; and Hopkins, Edward J.: Effects of Mach Number, Leading-Edge Bluntness, and Sweep on Boundary-Layer Transition on a Flat Plate. NASA TN D-1071, 1961.



12. Pate, S. R.; and Brillhart, R. E.: Investigation of Boundary-Layer Transition on Swept Wings at Mach Numbers 2.5 to 5. AEDC-TDR-63-109, U.S. Air Force, July 1963.
13. Bushnell, Dennis M.; and Huffman, Jarrett K.: Investigation of Heat Transfer to Leading Edge of a 76° Swept Fin With and Without Chordwise Slots and Correlations of Swept-Leading-Edge Transition Data for Mach 2 to 8. NASA TM X-1475, 1967.
14. Morrisette, E. Leon; Stone, David R.; and Whitehead, Allen H., Jr.: Boundary-Layer Tripping With Emphasis on Hypersonic Flows. Viscous Drag Reduction, C. Sinclair Wells, ed., Plenum Press, 1969, pp. 33-51.
15. Gentry, Arvel E.: Hypersonic Arbitrary-Body Aerodynamic Computer Program. Vol. I – User's Manual. Rep. DAC 56080 (Air Force Contract No. F33615 67 C 1008), Douglas Aircraft Co., Mar. 1967. (Available from DDC as AD817158.)
16. Gentry, Arvel E.: Hypersonic Arbitrary-Body Aerodynamic Computer Program. Vol. II – Program Formulation and Listings. Rep. DAC 56080 (Air Force Contract No. F33615 67 C 1008), Douglas Aircraft Co., Mar. 1967. (Available from DDC as AD817159.)
17. Eckert, E. R. G.: Engineering Relations for Friction and Heat Transfer to Surfaces in High Velocity Flow. J. Aeronaut. Sci. (Readers' Forum), vol. 22, no. 8, Aug. 1955, pp. 585-587.
18. Spalding, D. B.; and Chi, S. W.: The Drag of a Compressible Turbulent Boundary Layer on a Smooth Flat Plate With and Without Heat Transfer. J. Fluid Mech., vol. 18, pt. 1, Jan. 1964, pp. 117-143.
19. Gentry, Arvel E.; and Smyth, Douglas N.: Hypersonic Arbitrary-Body Aerodynamic Computer Program (Mark III Version). Vol. II – Program Formulation and Listings. Rep. DAC 61552, Vol. II (Air Force Contract Nos. F33615 67 C 1008 and F33615 67 C 1602), McDonnell Douglas Corp., Apr. 1968.
20. Bertram, Mitchel H.; Cary, Aubrey M., Jr.; and Whitehead, Allen H., Jr.: Experiments With Hypersonic Turbulent Boundary Layers on Flat Plates and Delta Wings. Hypersonic Boundary Layers and Flow Fields, AGARD CP No. 30, May 1968.

TABLE I.- GEOMETRIC CHARACTERISTICS OF MODELS

	Model 1	Model 2
Wing:		
Total area	224.082 cm ² (34.733 in ²)	241.660 cm ² (37.457 in ²)
Exposed area	115.943 cm ² (17.971 in ²)	133.520 cm ² (20.695 in ²)
Span	13.631 cm (5.366 in.)	14.834 cm (5.840 in.)
Aspect ratio	0.830	0.911
Root chord (fuselage center line)	30.183 cm (11.883 in.)	28.923 cm (11.387 in.)
Root chord (exposed)	22.746 cm (8.955 in.)	21.895 cm (8.620 in.)
Tip chord	4.155 cm (1.636 in.)	3.658 cm (1.440 in.)
Mean aerodynamic chord	20.362 cm (8.017 in.)	19.557 cm (7.700 in.)
Distance from nose to wing apex -		
Wing forward	3.962 cm (1.560 in.)	4.689 cm (1.846 in.)
Wing midposition	5.232 cm (2.060 in.)	5.959 cm (2.346 in.)
Wing aft		6.843 cm (2.694 in.)
Sweepback angle of leading edge	76.0°	72.8°
Dihedral angle	0°	-10.0°
Airfoil section	See fig. 2(c)	See fig. 3(b)
Leading-edge radius	0.038 cm (0.015 in.)	0.038 cm (0.015 in.)
Thickness-chord ratio at -		
Root	0.03	0.03
Tip	0.05	0.05
Elevon area (both)	22.408 cm ² (3.473 in ²)	23.152 cm ² (3.589 in ²)
Elevon deflection angles	5° to -45°	10° to -30°
Wing fins:		
V _{T,3} (tip fin with wing forward) -		
Area (each)	8.176 cm ² (1.267 in ²)	
Span	3.749 cm (1.476 in.)	
Root chord	4.361 cm (1.717 in.)	
Aspect ratio	1.720	
Toe-in angle	7.5°	
V _{T,4} (tip fin with wing midposition) -		
Area (each)	11.148 cm ² (1.728 in ²)	
Span	3.749 cm (1.476 in.)	
Root chord	5.161 cm (2.032 in.)	
Aspect ratio	1.260	
Toe-in angle	7.5°	
V _{T,6} and V _{T,7} (inboard fins) -		
Area (each)		11.148 cm ² (1.728 in ²)
Span		3.759 cm (1.480 in.)
Root chord		4.572 cm (1.800 in.)
Aspect ratio		1.280
Toe-in angle		0° and 5°

TABLE I.- GEOMETRIC CHARACTERISTICS OF MODELS - Concluded

	Model 1	Model 2
Upper vertical tail (exposed):		
Area	15.200 cm ² (2.356 in ²)	23.206 cm ² (3.597 in ²)
Span	2.794 cm (1.100 in.)	3.708 cm (1.460 in.)
Root chord (fuselage surface line)	6.223 cm (2.450 in.)	6.934 cm (2.730 in.)
Tip chord	4.597 cm (1.810 in.)	4.793 cm (1.887 in.)
Sweepback angle of leading edge	30°	30°
Included wedge angle	10°	12°
Leading-edge radius	0.025 cm (0.010 in.)	0.025 cm (0.010 in.)
Lower vertical tail (exposed):		
Area -		
With movable part	12.923 cm ² (2.003 in ²)	
Without movable part	5.523 cm ² (0.856 in ²)	7.658 cm ² (1.187 in ²)
Span -		
With movable part	2.375 cm ² (0.935 in ²)	
Without movable part	0.927 cm ² (0.365 in ²)	0.927 cm ² (0.365 in ²)
Root chord (fuselage surface line)	6.223 cm (2.450 in.)	6.934 cm (2.730 in.)
Tip chord -		
With movable part	4.874 cm (1.919 in.)	
Without movable part	5.687 cm (2.239 in.)	6.398 cm (2.519 in.)
Sweepback angle of leading edge	30°	30°
Included wedge angle	10°	15°
Leading-edge radius	0.025 cm (0.010 in.)	0.025 cm (0.010 in.)
Speed brakes:		
Area (each) -		
Upper vertical tail	1.942 cm ² (0.303 in ²)	2.303 cm ² (0.357 in ²)
Lower vertical tail	1.942 cm ² (0.303 in ²)	2.510 cm ² (0.389 in ²)
Deflection angles	0° to 40°	0° to 40°
Fuselage:		
Length	36.881 cm (14.520 in.)	36.881 cm (14.520 in.)
Maximum diameter	2.845 cm (1.120 in.)	2.845 cm (1.120 in.)
Base diameter	2.446 cm (0.963 in.)	2.446 cm (0.963 in.)
Side area	95.681 cm ² (14.831 in ²)	95.681 cm ² (14.831 in ²)
Planform area (including side fairings)	132.712 cm ² (20.570 in ²)	132.712 cm ² (20.570 in ²)
Nose cone half-angle	10°	10°
Nose radius	0.165 cm (0.065 in.)	0.165 cm (0.065 in.)

TABLE II.- INDEX OF DATA FIGURES

(a) Model 1

Mach number, M_∞	Effects of -	Configuration	Elevon deflection, deg		Vertical-tail deflection, deg		Angle of attack, α , deg	Figure
			$\delta_{E,L}$	$\delta_{E,R}$	$\delta_{V,U}$	$\delta_{V,L,2}$		
Parameters: C_L , L/D , δ_E , $aC_m/\partial C_N$, $C_{n\beta}$, $C_{l\beta}$, $C_{Y\beta}$								
6	Trim	BX ₂ W ₂ E ₂ V _U V _{L,2} BX ₂ W ₂ E ₂ V _U V _L V _T BX ₂ W ₂ E ₂ V _U V _{L,2} V _T BX ₂ W ₂ E ₂ V _U V _{R,O} BX ₂ W ₂ E ₂ V _U V _{R,O} V _T	0 to -45 ↓	0 to -45 ↓	0 ↓	0 0	-4 to 14	8
Parameters: C_L , C_D , C_m , L/D								
6	Component parts	BX ₂ BX ₂ W ₂ E ₂ BX ₂ W ₂ E ₂ V _U BX ₂ W ₂ E ₂ V _U V _L BX ₂ W ₂ E ₂ V _U V _{L,2} BX ₂ W ₂ E ₂ V _U V _L V _T BX ₂ W ₂ E ₂ V _U V _{L,2} V _T BX ₂ W ₂ E ₂ V _U V _{R,C} BX ₂ W ₂ E ₂ V _U V _{R,O} BX ₂ W ₂ E ₂ V _U V _{R,C} V _T BX ₂ W ₂ E ₂ V _U V _{R,O} V _T	0 ↓	0 ↓	0 ↓	0 0	-4 to 12	9
Parameters: $C_{n\beta}$, $C_{l\beta}$, $C_{Y\beta}$								
6	Component parts	BX ₂ BX ₂ W ₂ E ₂ BX ₂ W ₂ E ₂ V _U BX ₂ W ₂ E ₂ V _U V _L BX ₂ W ₂ E ₂ V _U V _{L,2} BX ₂ W ₂ E ₂ V _U V _L V _T BX ₂ W ₂ E ₂ V _U V _{L,2} V _T	0 ↓	0 ↓	0 ↓	0 0	-4 to 12	25
Parameters: $(L/D)_{T,max}$, $\delta_{E,T}$								
6	Center-of-gravity location	BX ₂ W ₂ E ₂ V _U V _L V _{T,4}	0 to -45	0 to -45	0		-4 to 14	10
Parameters: C_L , L/D , δ_E , $aC_m/\partial C_N$, $C_{n\beta}$, $C_{l\beta}$, $C_{Y\beta}$								
8	Trim	BX ₂ W ₂ E ₂ V _U V _L V _{T,4}	0 to -45	0 to -45	0		-2 to 14	11

TABLE II.- INDEX OF DATA FIGURES - Continued

(a) Model 1 - Concluded

Mach number, M_∞	Effects of -	Configuration	Elevon deflection, deg		Vertical-tail deflection, deg		Angle of attack, α , deg	Figure
			$\delta_{E,L}$	$\delta_{E,R}$	δ_{VU}	$\delta_{VL,2}$		
Parameters: $C_L, C_D, L/D, C_m$								
8	Elevon deflection	$BX_2W_2E_2V_UV_LV_T,4$	0 to -45	0 to -45	0		-6 to 16	12(a)
Parameters: $C_{n\beta}, C_{l\beta}, C_{Y\beta}$								
8	Elevon deflection	$BX_2W_2E_2V_UV_LV_T,4$	0 to -45	0 to -45	0		-6 to 19	12(b)
Parameters: $C_L, C_D, L/D, C_m$								
6	Roughness	$BX_2W_2E_2V_UV_L,2V_T,3$	0 to -45	0 to -45	0	0	-4 to 16	13
Parameters: C_D, C_m, C_L								
6	Elevon deflection	$BX_2W_2E_2V_UV_L,2$ $BX_2W_2E_2V_UV_LV_T$ $BX_2W_2E_2V_UV_L,2V_T$ $BX_2W_2E_2V_UV_R,C$ $BX_2W_2E_2V_UV_R,O$ $BX_2W_2E_2V_UV_R,CV_T$ $BX_2W_2E_2V_UV_R,O^VT$	0 to -45 ↓ ↓ ↓ ↓ ↓ ↓	0 to -45 ↓ ↓ ↓ ↓ ↓ ↓	0 ↓ ↓ ↓ ↓ ↓ ↓	0 0	-4 to 14	26
Parameters: $C_{Y\beta}, C_{n\beta}, C_{l\beta}$								
6	Elevon deflection	$BX_2W_2E_2V_UV_L,2$ $BX_2W_2E_2V_UV_LV_T$ $BX_2W_2E_2V_UV_L,2V_T$	0 to -45 ↓ ↓	0 to -45 ↓ ↓	0 ↓ ↓	0 0	-4 to 14	27
Parameters: $C_{n\delta'_E}, C_{l\delta'_E}, C_{Y\delta'_E}$								
6	Differential elevon deflection	$BX_2W_2E_2V_UV_L,2$ $BX_2W_2E_2V_UV_L,2V_T$	-5 -25 -45	5 -15 -35	0 ↓ ↓	0 ↓ ↓	-4 to 14	28
Parameters: $C_{n\delta_V}, C_{l\delta_V}, C_{Y\delta_V}$								
6	Vertical-tail deflection	$BX_2W_2E_2V_UV_L$ $BX_2W_2E_2V_UV_L,2$	0 0	0 0	-5 -5		-4 to 12	29

TABLE II. - INDEX OF DATA FIGURES - Continued

(b) Model 2

Mach number, M_∞	Effects of -	Configuration	Elevon deflection ($\delta_{E,L} = \delta_{E,R}$), deg	Angle of attack, α , deg	Figure
Parameters: C_L , L/D , δ_E , $\partial C_m / \partial C_L$					
6	Component parts on trim for c.g. at $0.40\bar{c}$	BX ₃ W ₃ E ₃ V _{U,2} V _{L,6} BX ₃ W ₃ E ₃ V _{U,2} V _{R,O} BX ₃ W ₃ E ₃ V _{U,2} V _{L,6} V _{T,6} BX ₃ W ₃ E ₃ V _{U,2} V _{L,6} V _{T,7}	10 to -30	-3 to 14	14(a)
	Nose cant on trim for c.g. at $0.40\bar{c}$	BX ₃ W ₃ E ₃ V _{U,2} V _{L,6}	10 to -30	-3 to 15	15
	Strakes on trim for c.g. at $0.40\bar{c}$	BX ₃ W ₃ E ₃ V _{U,2} V _{L,6} B ₂ X ₃ W ₃ E ₃ V _{U,2} V _{L,6}	10 to -30	-3 to 15	17
Parameters: $C_{n\beta}$, $C_{l\beta}$, $C_{Y\beta}$					
6	Component parts on trim for c.g. at $0.40\bar{c}$	BX ₃ W ₃ E ₃ V _{U,2} V _{L,6} BX ₃ W ₃ E ₃ V _{U,2} V _{R,O} BX ₃ W ₃ E ₃ V _{U,2} V _{L,6} V _{T,6} BX ₃ W ₃ E ₃ V _{U,2} V _{L,6} V _{T,7}	10 to -30	-3 to 12	14(b)
	Nose cant on trim for c.g. at $0.40\bar{c}$	BX ₃ W ₃ E ₃ V _{U,2} V _{L,6}	10 to -30	-3 to 15	16
Parameters: C_L , C_D , L/D , C_m					
6	Wing position	BX ₃ W ₃ E ₃ V _U V _L BX ₂ W ₂ E ₂ V _U V _L	0	-4 to 12	18(a)
	Component parts	BX ₃ W ₃ E ₃ V _{U,2} V _{L,6} BX ₃ W ₃ E ₃ V _U V _L BX ₃ W ₃ E ₃ V _{U,2} V _{R,O} BX ₃ W ₃ E ₃ V _{U,2} V _P BX ₃ W ₃ E ₃ V _{U,2} V _{L,6} V _{T,6} BX ₃ W ₃ E ₃ V _{U,2} V _{L,6} V _{T,7} BX ₃ W ₃ E ₃ V _{U,2} V _{L,6} (δ_N) B ₂ X ₃ W ₃ E ₃ V _{U,2} V _{L,6} (δ_N) BX ₃ W ₃ E ₃ V _{U,B} V _{L,B} BX ₃ W ₃ E ₃ V _{U,2B} V _{L,6B}	0 0 0 0 0 0 0 0 0	-4 to 14 -4 to 14	19(a) 30(a) 31(a) 32

TABLE II.- INDEX OF DATA FIGURES - Concluded

(b) Model 2 - Concluded

Mach number, M_∞	Effects of -	Configuration	Elevon deflection ($\delta_{E,L} = \delta_{E,R}$), deg	Angle of attack, α , deg	Figure
		Parameters: $C_{n\beta}$, $C_{l\beta}$, $C_{Y\beta}$			
6	Wing position	BX ₃ W ₃ E ₃ V _U V _L BX ₂ W ₂ E ₂ V _U V _L	0	-4 to 12	18(b)
	Component parts	BX ₃ W ₃ E ₃ V _U ,2V _L ,6 BX ₃ W ₃ E ₃ V _U V _L BX ₃ W ₃ E ₃ V _U ,2V _R ,O BX ₃ W ₃ E ₃ V _U ,2V _P BX ₃ W ₃ E ₃ V _U ,2V _L ,6V _T ,6 BX ₃ W ₃ E ₃ V _U ,2V _L ,6V _T ,7 BX ₃ W ₃ E ₃ V _U ,2V _L ,6(δ_N) B ₂ X ₃ W ₃ E ₃ V _U ,2V _L ,6(δ_N) BX ₃ W ₃ E ₃ V _U ,B V _L ,B BX ₃ W ₃ E ₃ V _U ,2B V _L ,6B	0 0 0 0 0 0 0 0	-4 to 14 -4 to 14 -4 to 14 -4 to 14 -4 to 14 -4 to 14 -4 to 14	19(b) 30(b) 31(b) 33
		Parameters: $(L/D)_{max}$, δ_E , $C_{n\beta}$, $\partial C_m / \partial C_L$			
6	Wing position on maximum trimmed L/D	BX ₃ W ₃ E ₃ V _U ,2V _L ,6 BX ₃ W ₃ E ₃ V _U ,2V _R ,O B ₂ X ₃ W ₃ E ₃ V _U ,2V _L ,6	10 to -15	-----	20
		Parameters: C_D , C_m , C_L			
6	Elevon deflection	BX ₃ W ₃ E ₃ V _U ,2V _L ,6 BX ₃ W ₃ E ₃ V _U ,2V _L ,6V _T BX ₃ W ₃ E ₃ V _U ,2V _R ,O B ₂ X ₃ W ₃ E ₃ V _U ,2V _L ,6	10 to -30 10 to -30 10 to -30 10 to -30	-4 to 14 -4 to 14 -4 to 14 -4 to 14	34 36 37(a) 38
		Parameters: $C_{Y\beta}$, $C_{n\beta}$, $C_{l\beta}$			
6	Elevon deflection	BX ₃ W ₃ E ₃ V _U ,2V _L ,6 BX ₃ W ₃ E ₃ V _U ,2V _R ,O B ₂ X ₃ W ₃ E ₃ V _U ,2V _L ,6	10 to -20 10 to -10 10 to -10	-4 to 14 -4 to 14 -4 to 14	35 37(b) 39
		Parameters: C_L , L/D, δ_E , $\partial C_m / \partial C_L$			
6	Center-of-gravity location on trim	BX ₃ W ₃ E ₃ V _U ,2V _L ,6 BX ₃ W ₃ E ₃ V _U ,2V _R ,O B ₂ X ₃ W ₃ E ₃ V _U ,2V _L ,6	10 to -30	-4 to 15	40

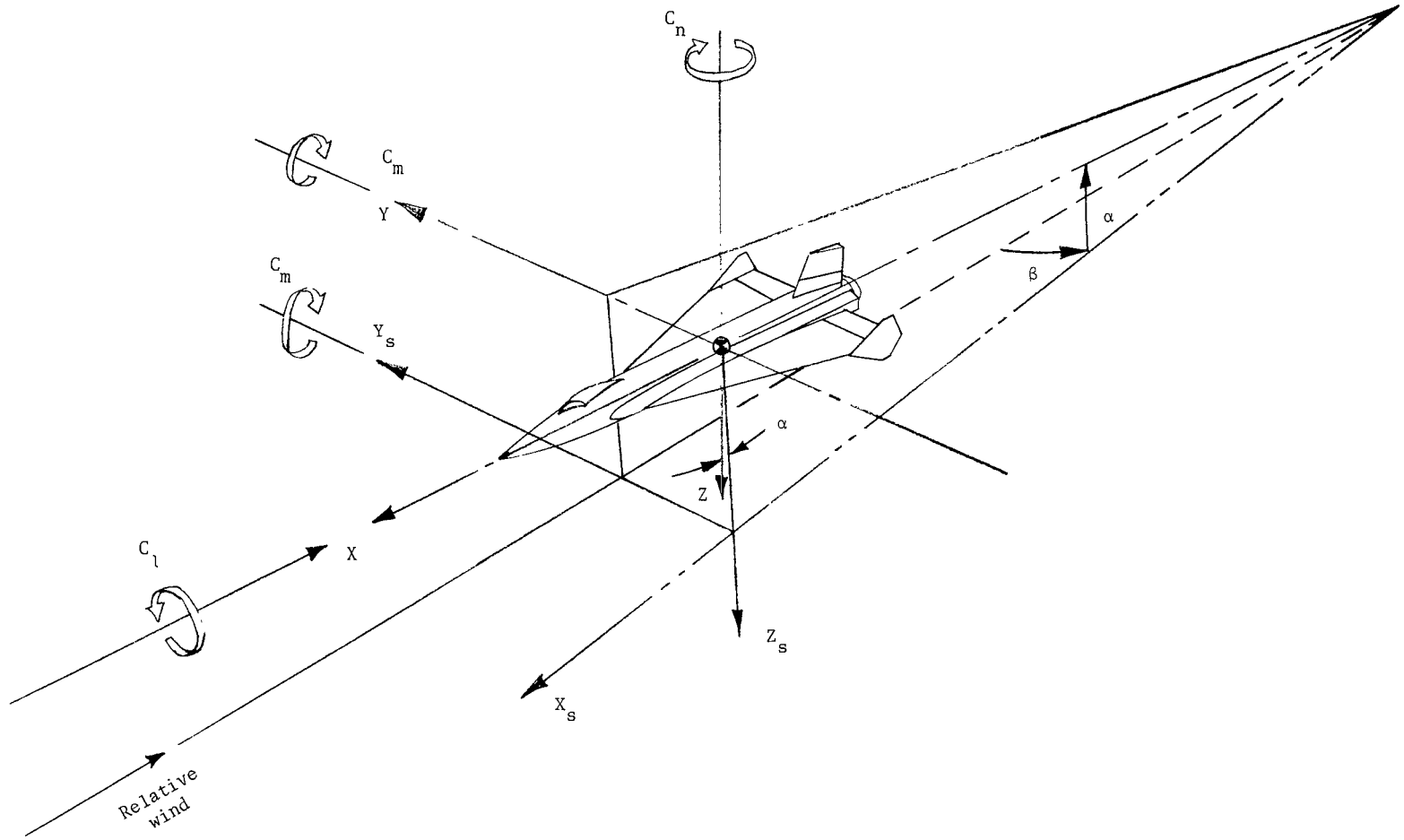
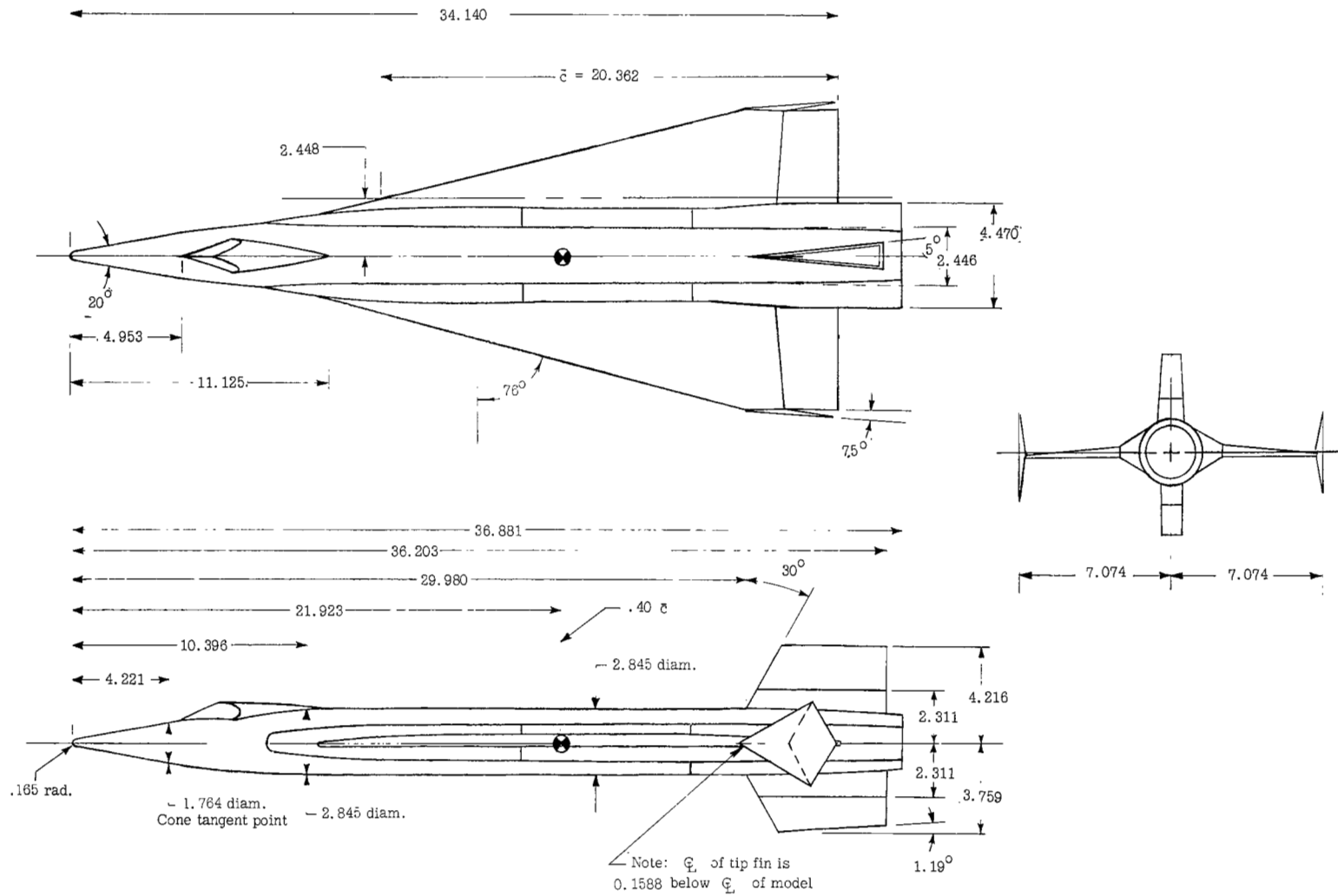
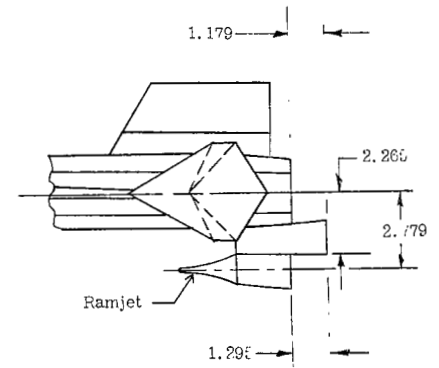
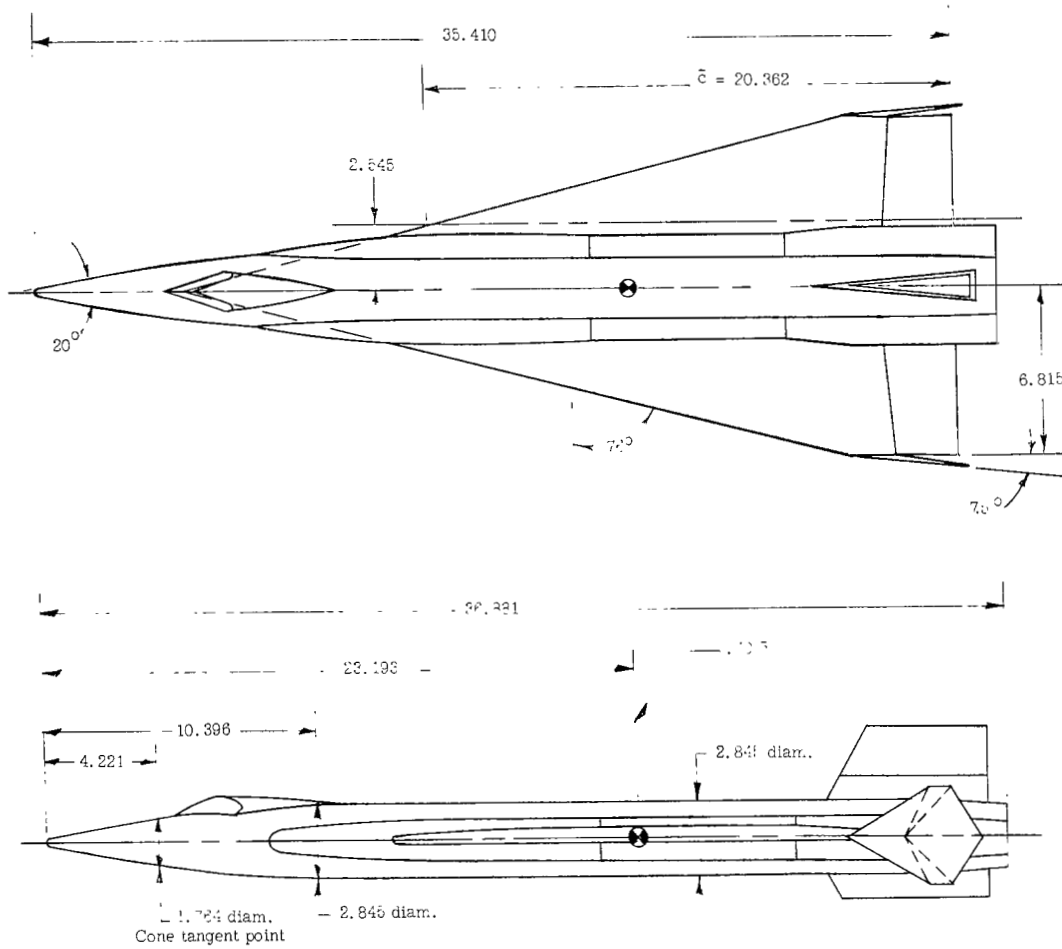


Figure 1.- Body- and stability-axis systems.



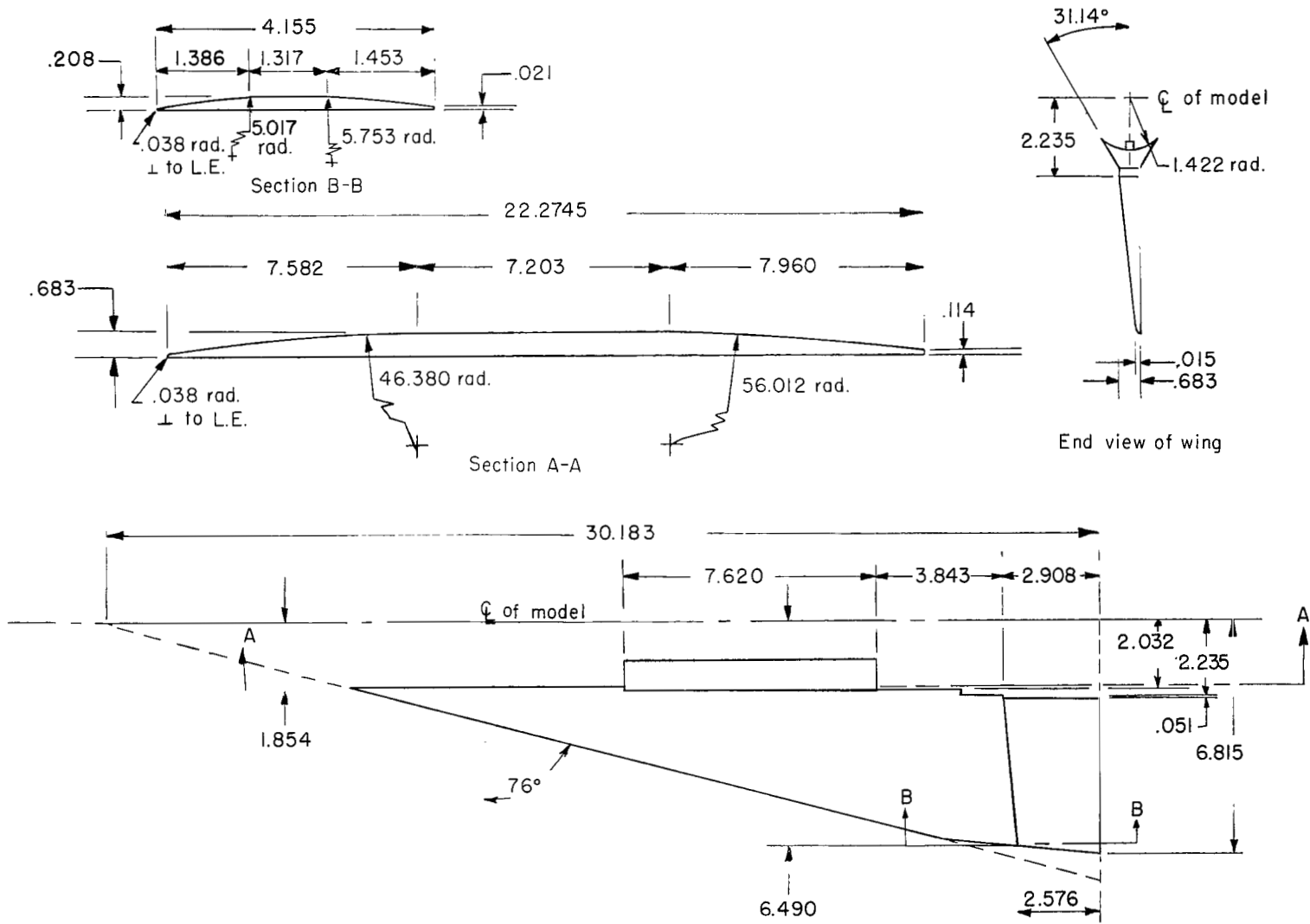
(a) Model (BX₂W₂E₂V_UV_{L,2}V_{T,3}) with wing in forward position.

Figure 2.- Model 1. Dimensions are in centimeters unless otherwise indicated. (1 cm = 0.39 in.)



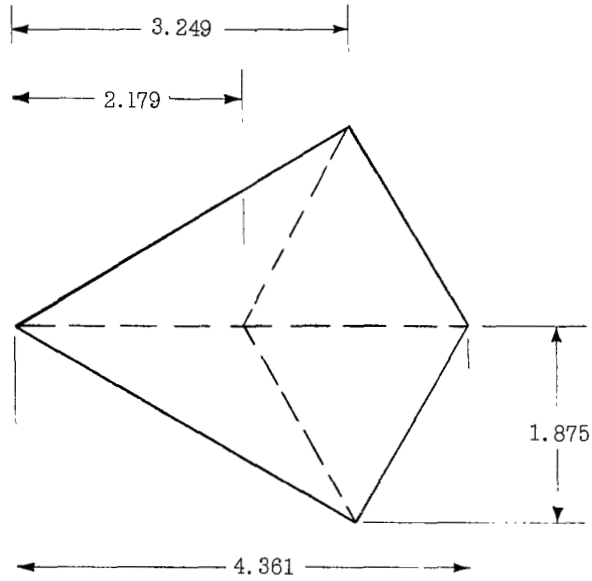
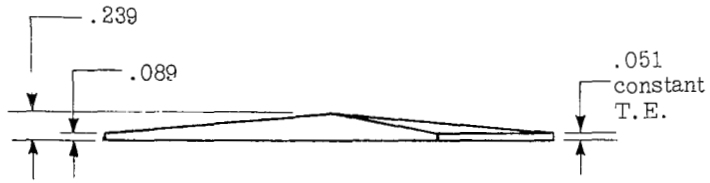
(b) Model with lower vertical tail (BX₂W₂E₂V_UV_LV_{T,4}) and ramjet (BX₂W₂E₂V_UV_{R,C}V_{T,4}) with wing in midposition.

Figure 2.- Continued.

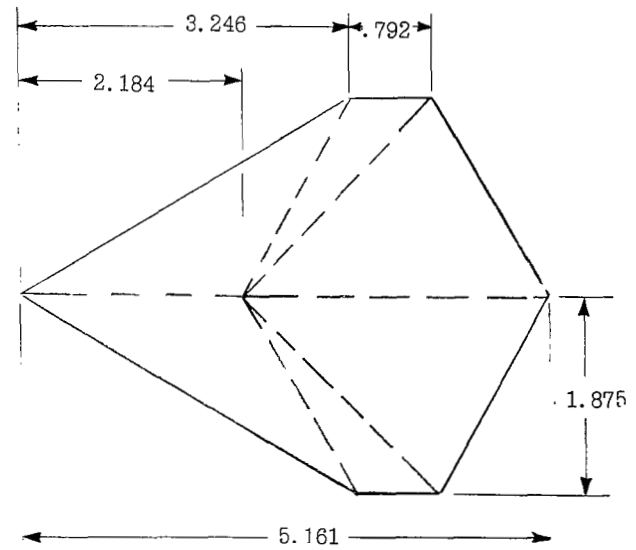


(c) Wing W₂E₂.

Figure 2.- Continued.



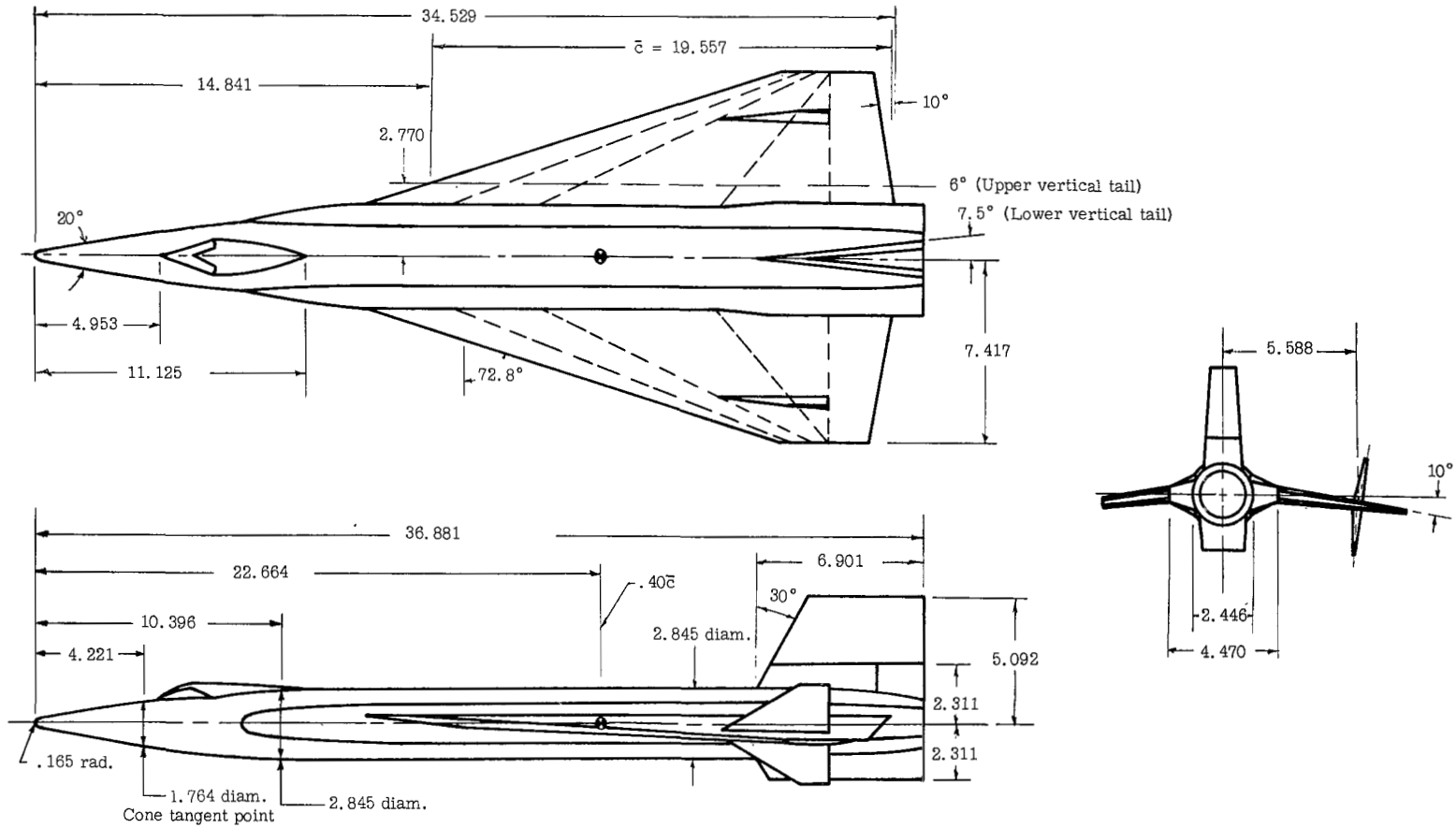
Tip fin $V_{T,3}$ for wing in forward position



Tip fin $V_{T,4}$ for wing in midposition

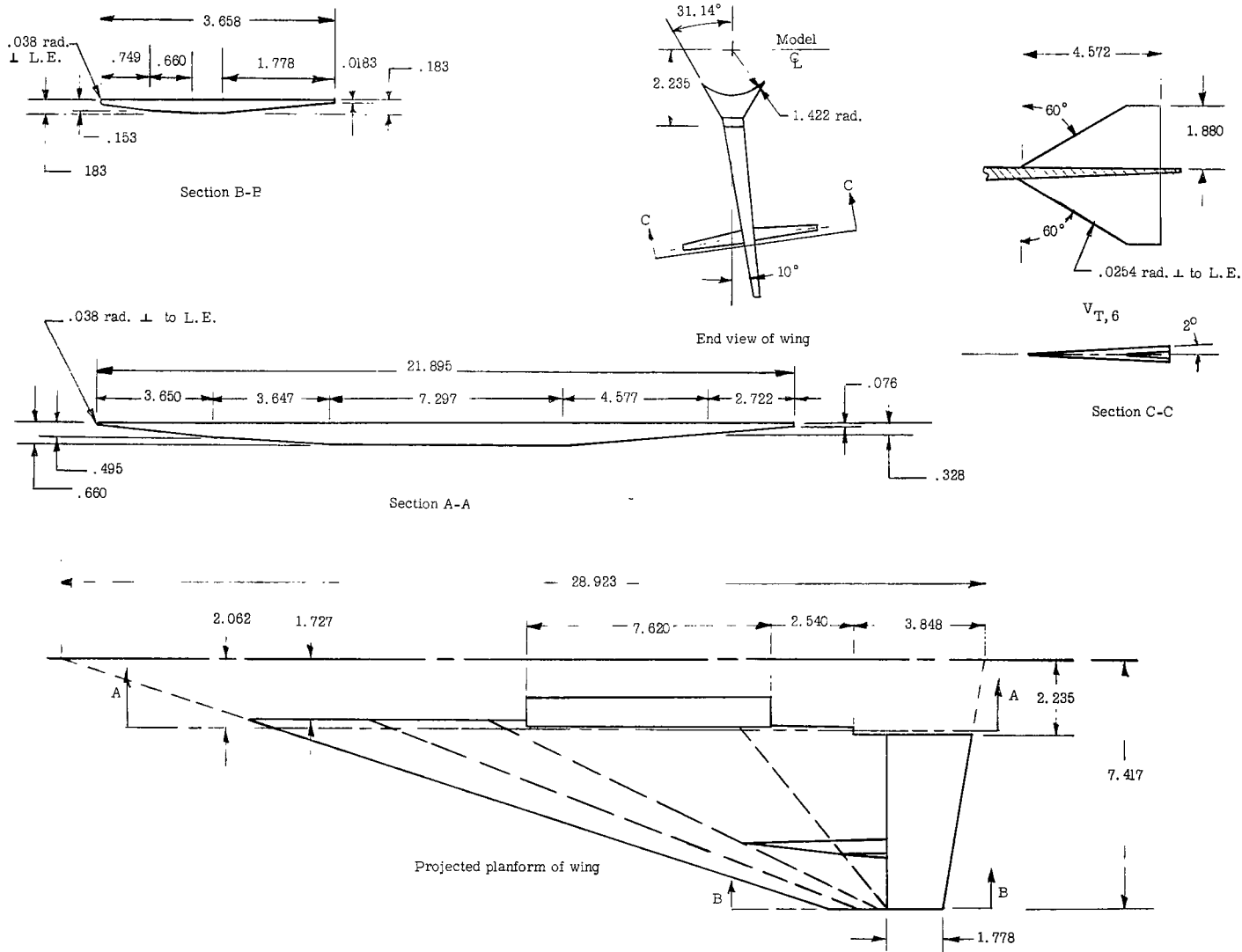
(d) Tip fins.

Figure 2.- Continued.



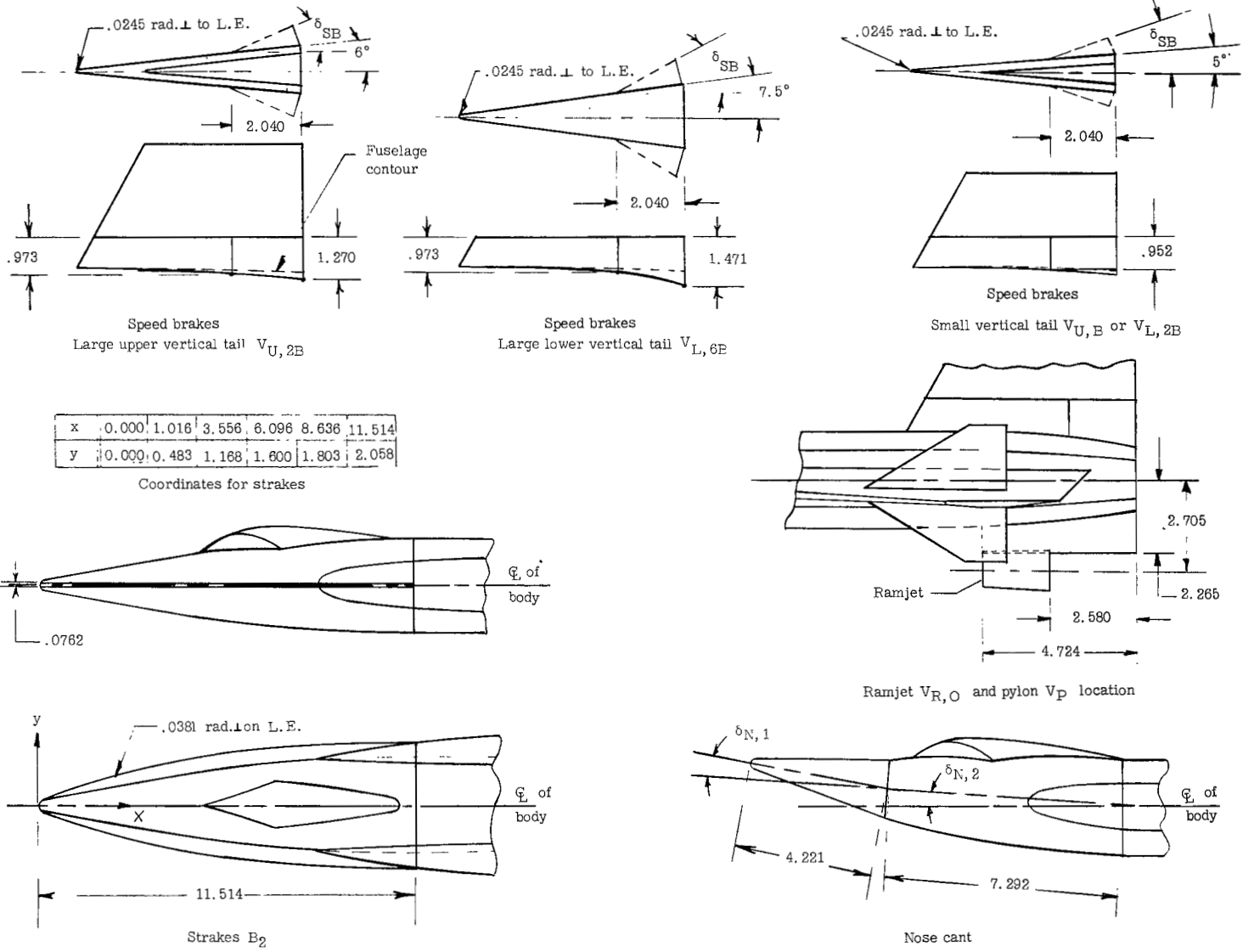
(a) Model (BX₃W₃E₃V_{U,2}V_{L,6}V_{T,6}) with wing in midposition.

Figure 3.- Model 2. Dimensions are in centimeters unless otherwise indicated. (1 cm = 0.39 in.)



(b) Wing W_3E_3 and inboard fins $V_{T,6}$.

Figure 3.- Continued.



(c) Miscellaneous details.

Figure 3.- Concluded.

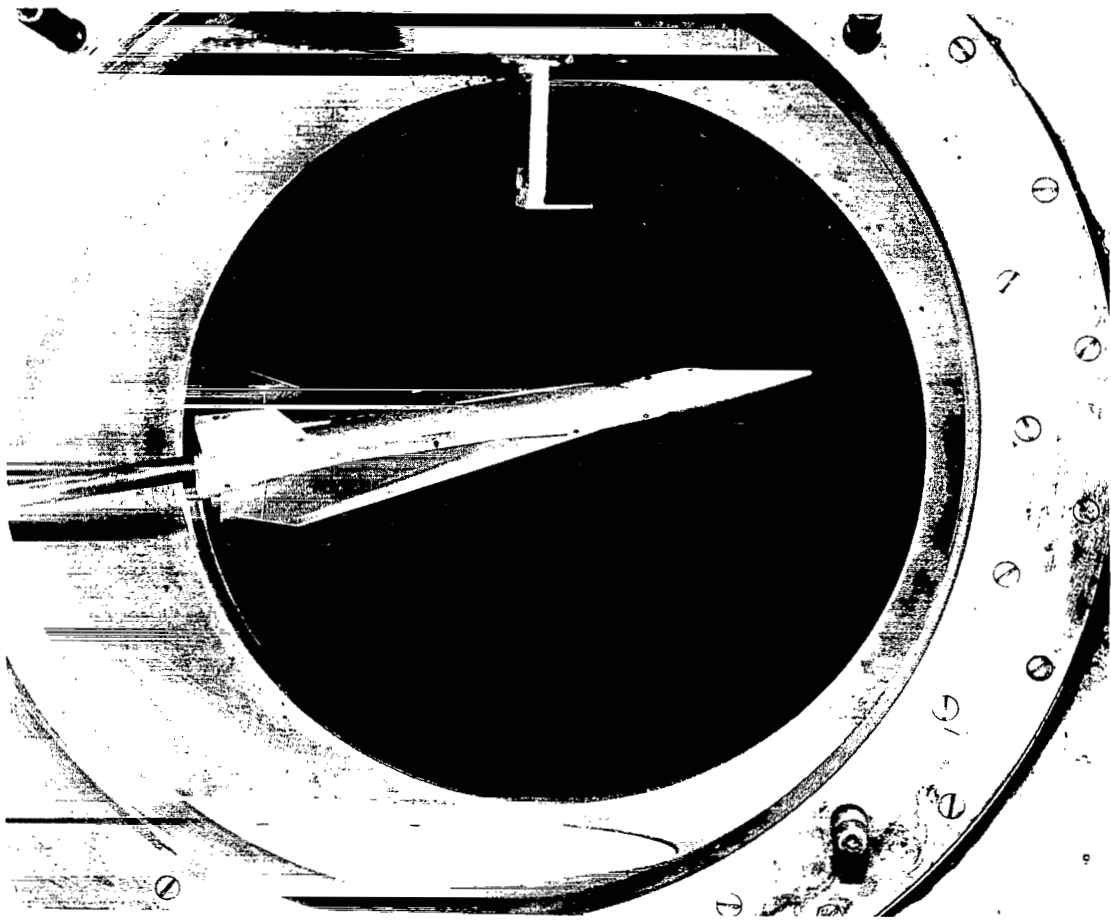


Figure 4.- Model 1 with tip fins (BX₂W₂E₂V_UV_LV_T,₄) with wing in midposition in the Langley 20-inch Mach 6 tunnel. L-67-3334

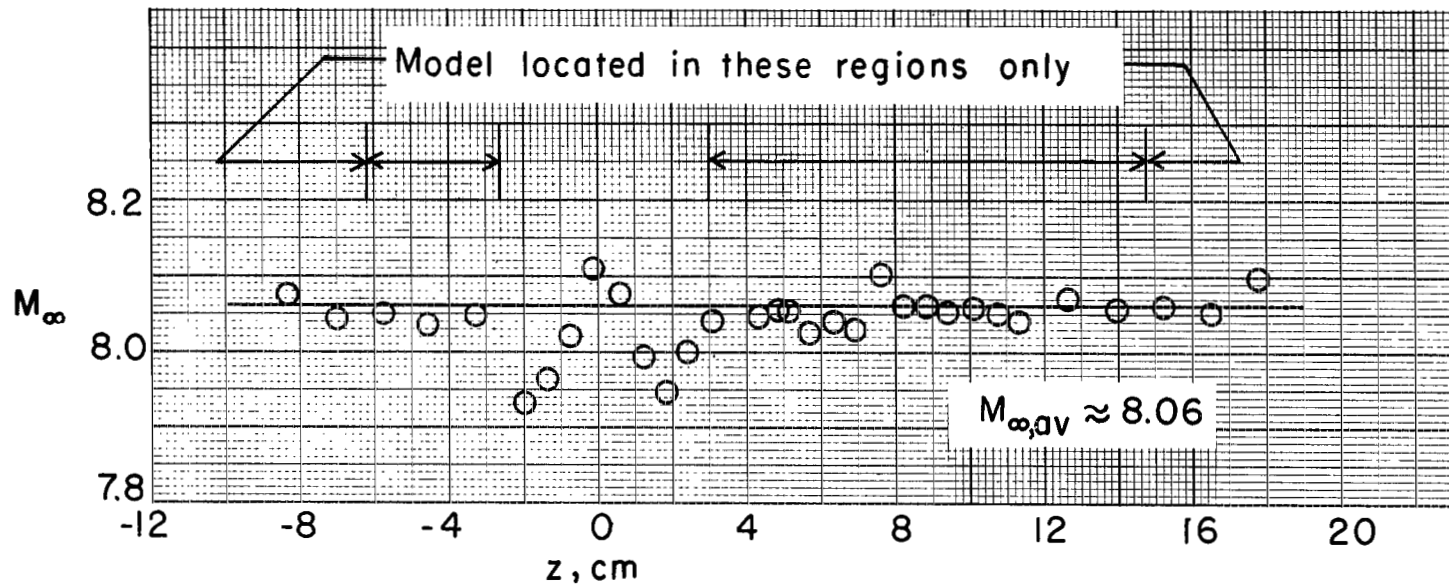
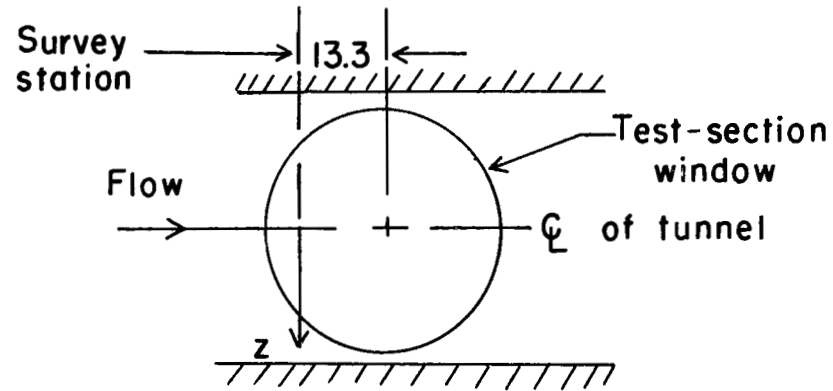


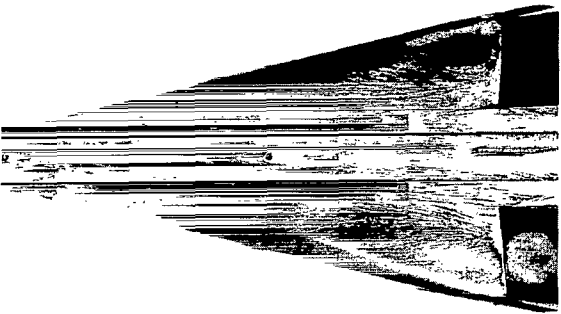
Figure 5.- Mach number calibration of Langley Mach 8 variable-density hypersonic tunnel.
 $p_t = 17.3 \text{ MN/m}^2$ (2510 psi); $T_t = 811^\circ \text{ K}$ (1000° F).



$\delta_E = 0^\circ$



$\delta_E = -15^\circ$

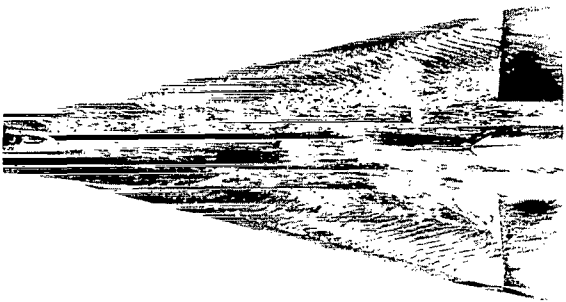


$\delta_E = -25^\circ$

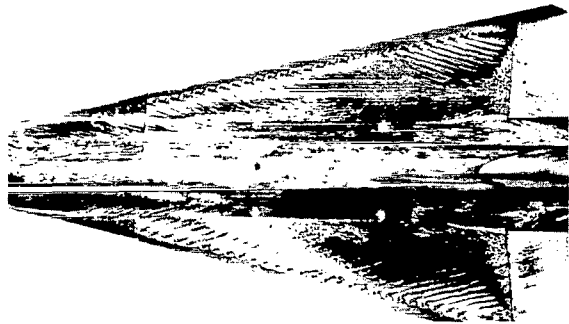


$\delta_E = -35^\circ$

(a) $M_\infty = 6$; $\alpha = 0^\circ$; without roughness.



$\delta_E = -15^\circ$

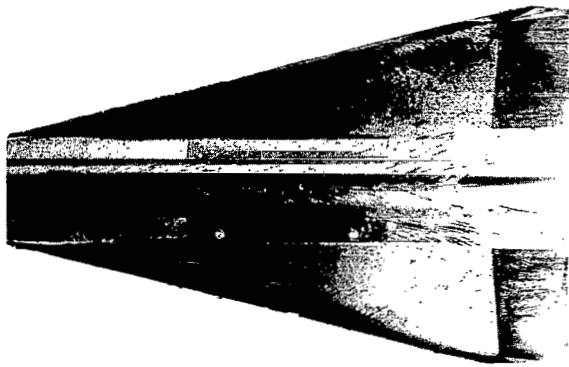


$\delta_E = -25^\circ$

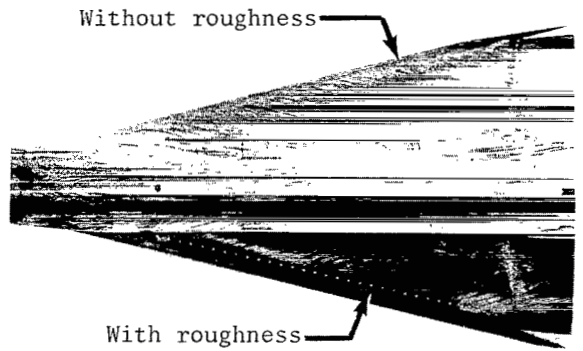
(b) $M_\infty = 6$; $\alpha = 0^\circ$; with roughness.

L-69-5076

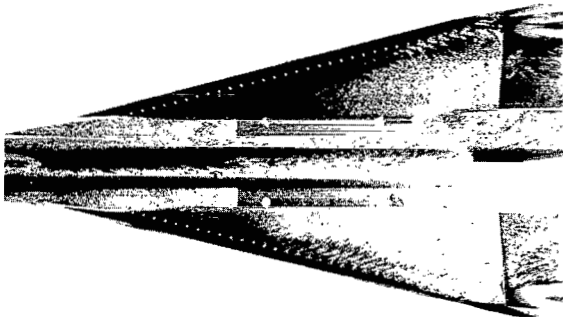
Figure 6.- Oil-flow patterns of upper surface of wing of model 1 (BX₂W₂E₂V_UV_{L,2}V_{T,3}) at $M_\infty = 6$ and $M_\infty = 8$.



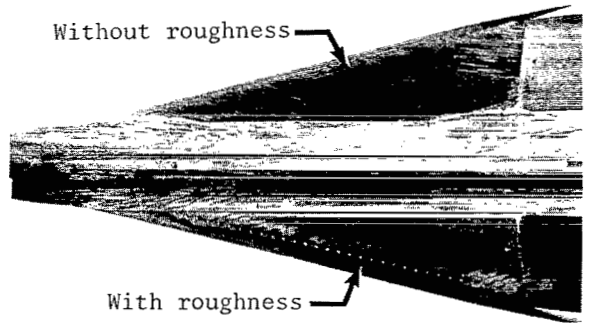
$\alpha = 6^\circ$, without roughness



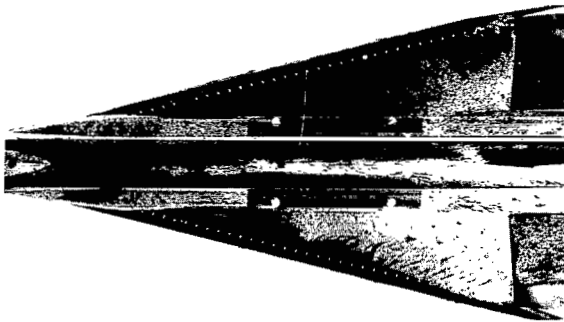
$\delta_E = -15^\circ$



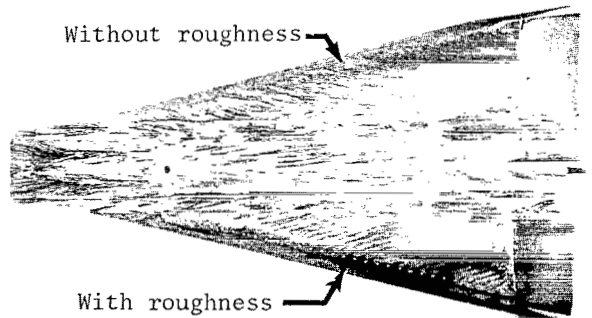
$\alpha = 6^\circ$, with roughness



$\delta_E = -25^\circ$



$\alpha = 4^\circ$, with roughness



$\delta_E = -35^\circ$

(c) $M_\infty = 6$; $\delta_E = -15^\circ$.

(d) $M_\infty = 8$; $\alpha = 0^\circ$.

L-69-5077

Figure 6.- Concluded.

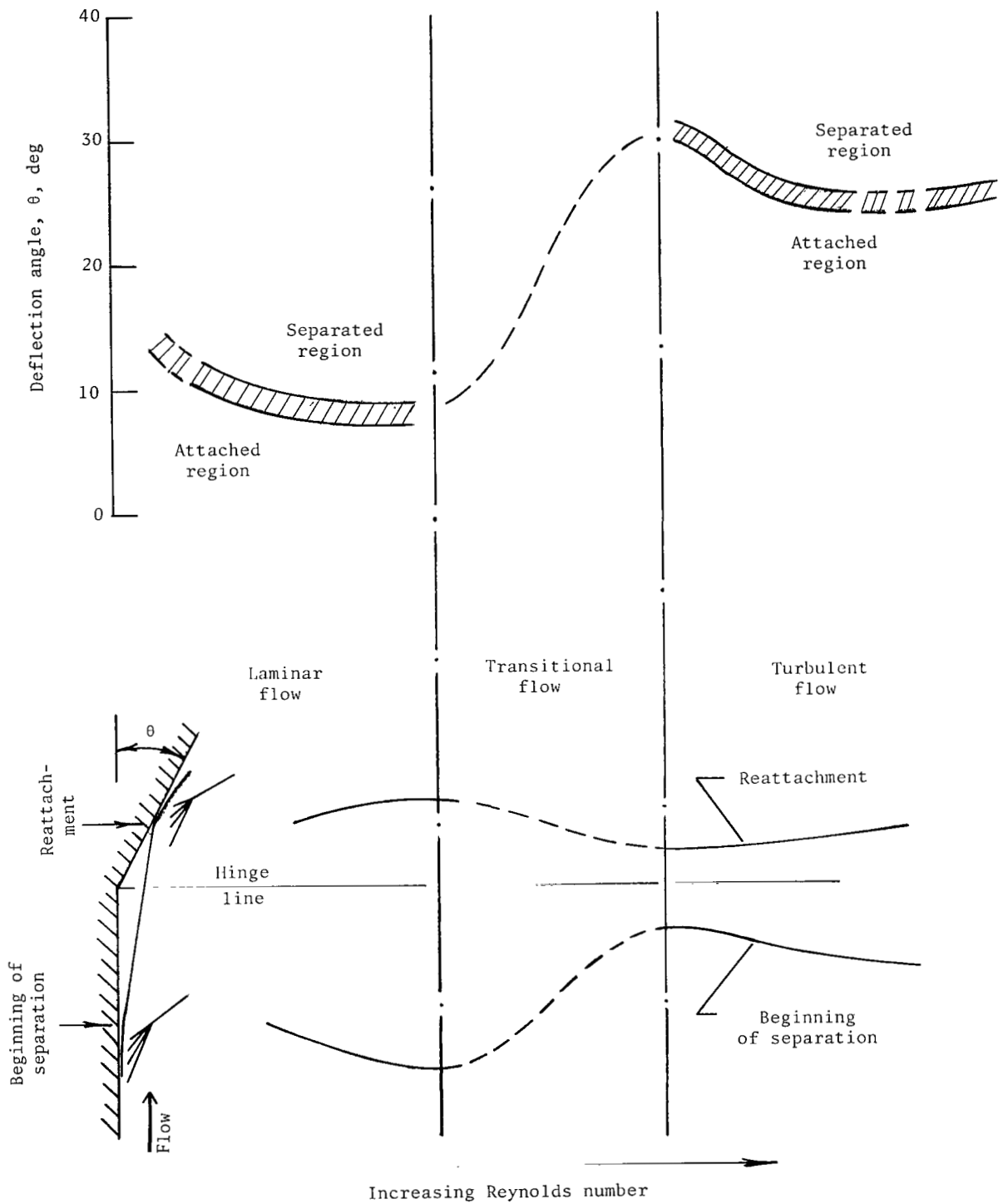
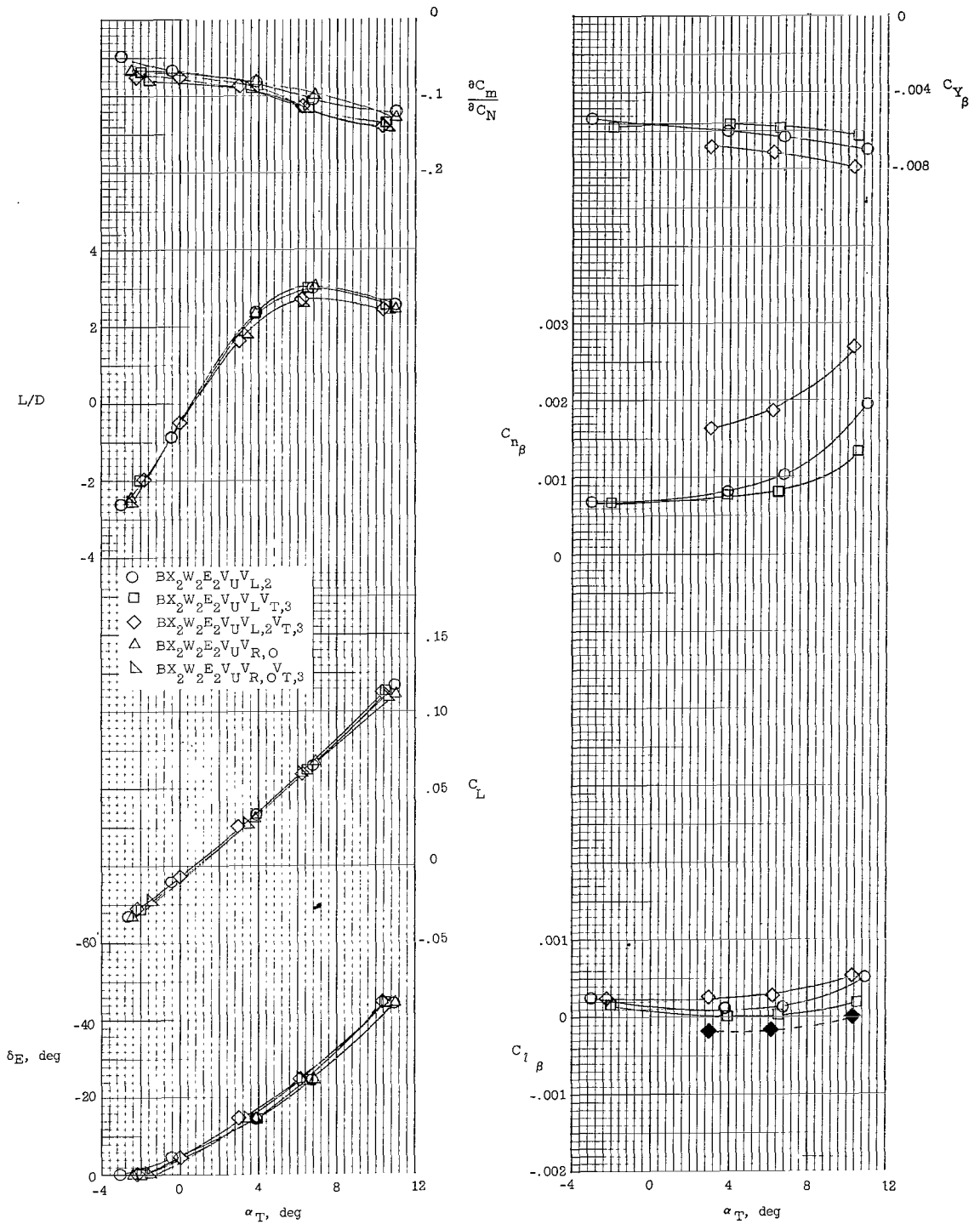
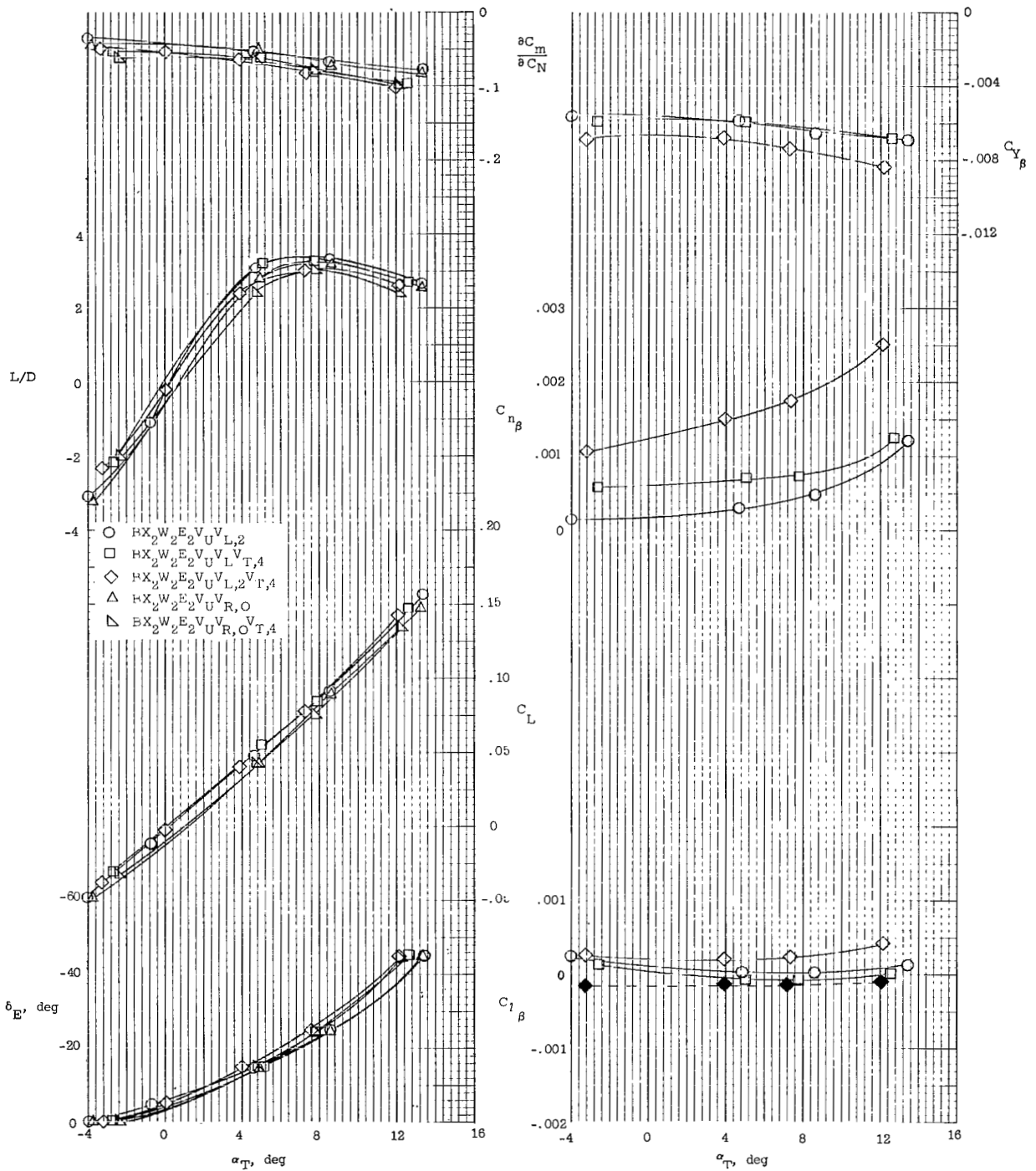


Figure 7.- Reynolds number effect on two-dimensional separation. $M_\infty = 6$; data from references 2, 5, and 6.



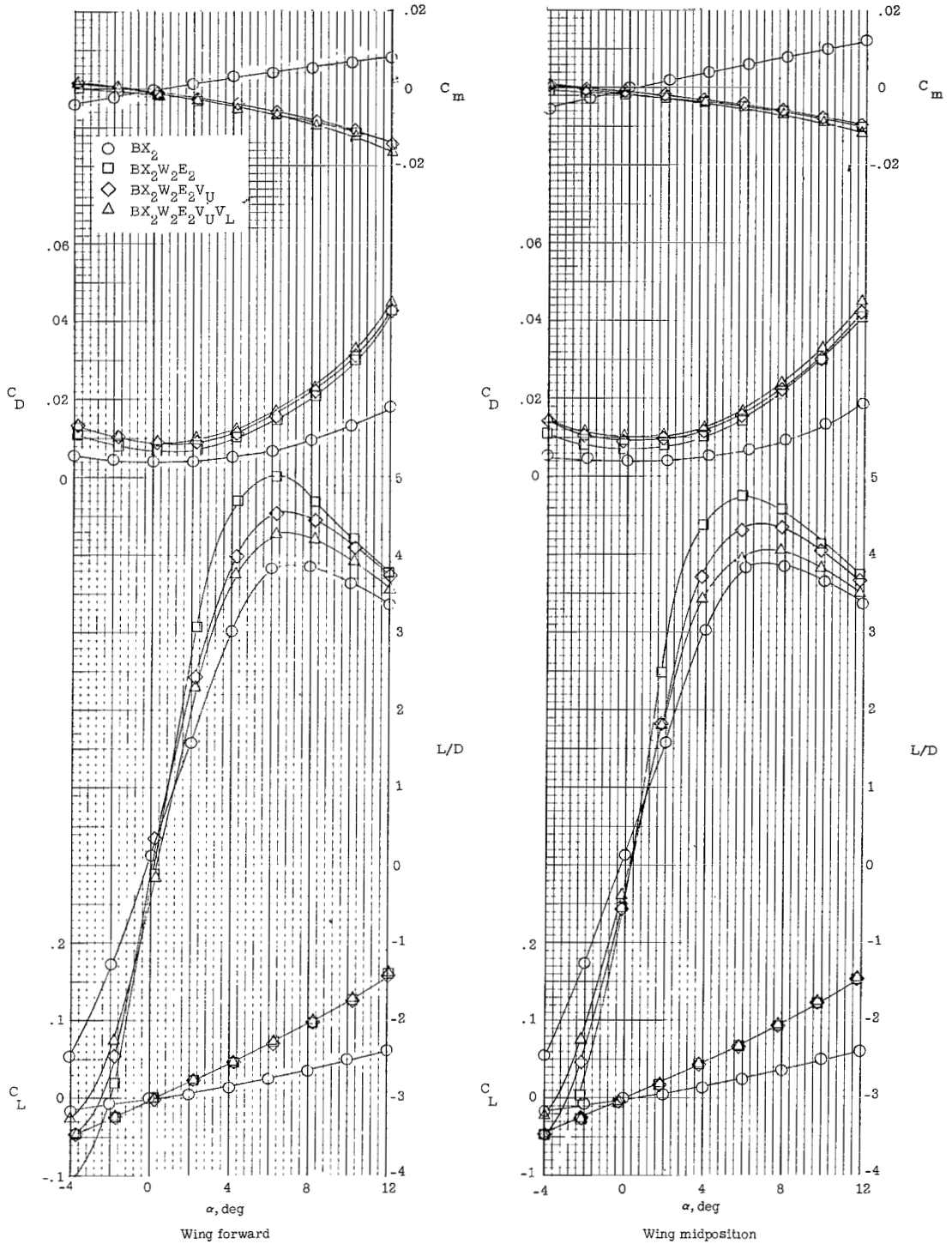
(a) Wing forward.

Figure 8.- Longitudinal, lateral, and directional stability characteristics at trim of model 1. $M_\infty = 6$; solid symbols indicate calculated points for tip-fin center line on X-axis.



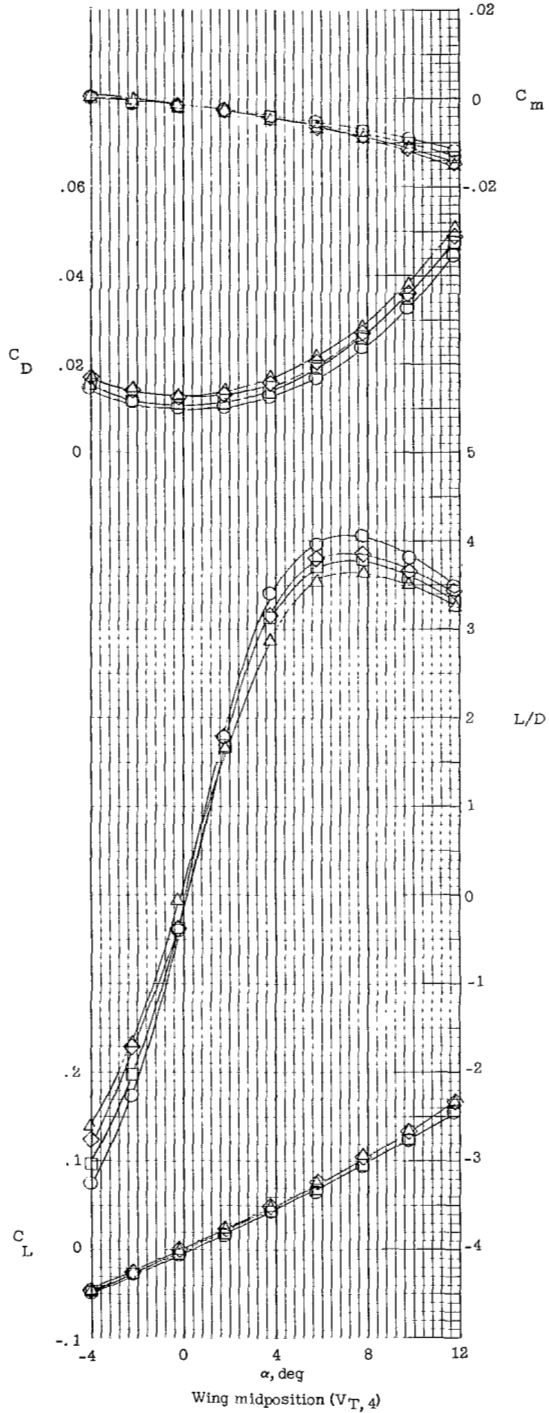
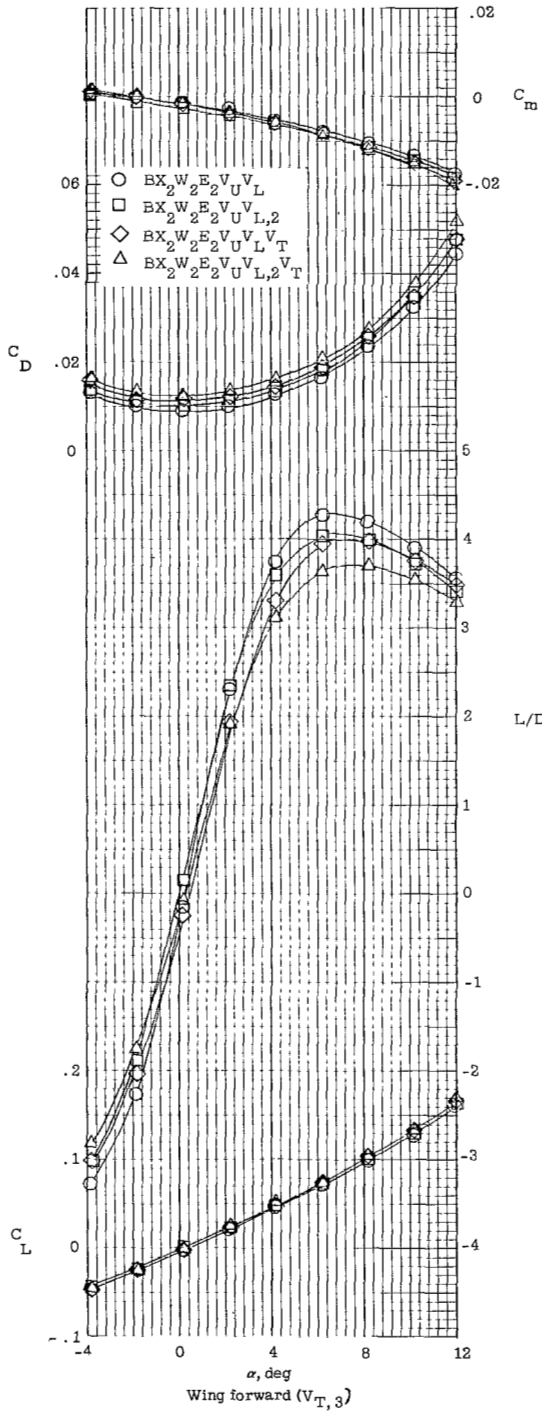
(b) Wing midposition.

Figure 8.- Concluded.



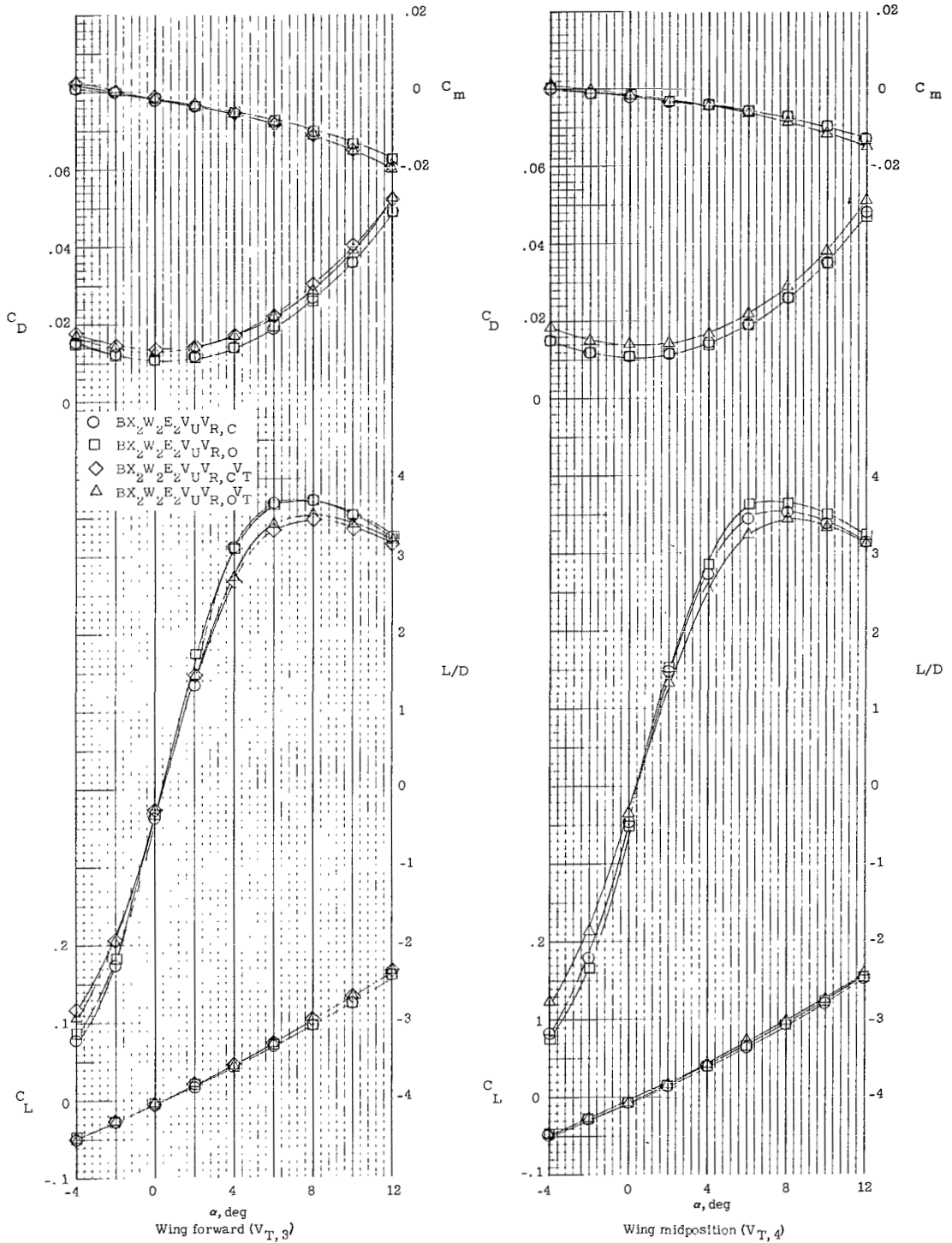
(a) Side fairing, wing, upper vertical tail, and lower vertical tail.

Figure 9.- Effect of component parts on longitudinal aerodynamic characteristics of model 1. $M_\infty = 6$; $\delta_{E,L} = \delta_{E,R} = \delta_{V,U} = \delta_{V,L,2} = 0^\circ$.



(b) Side fairing, wing, upper vertical tail, lower vertical tail, and tip fins.

Figure 9.- Continued.



(c) Side fairing, wing, upper vertical tail, ramjet, and tip fins.

Figure 9.- Concluded.

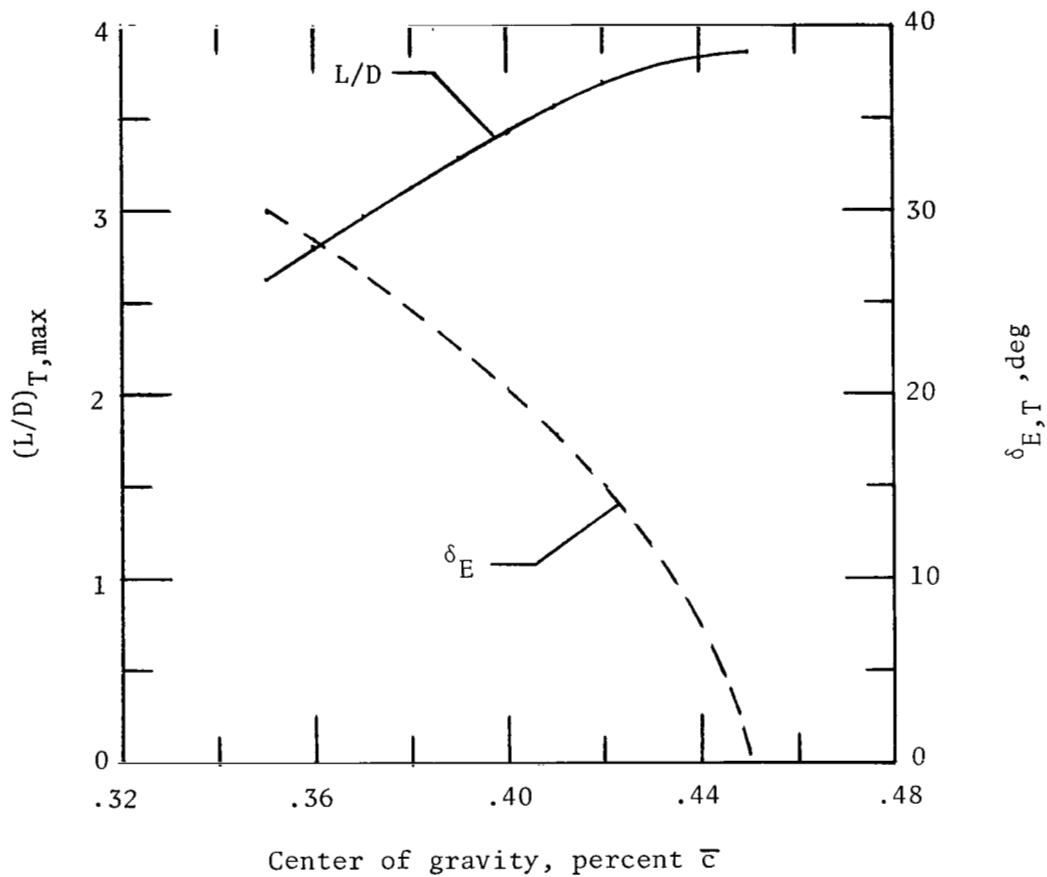


Figure 10.- Effect of center-of-gravity location on maximum trimmed L/D for model 1 (BX₂W₂E₂V_UV_LV_T,4) with wing in midposition.
 $M_\infty = 6$; $\alpha = -4^\circ$ to 14° .

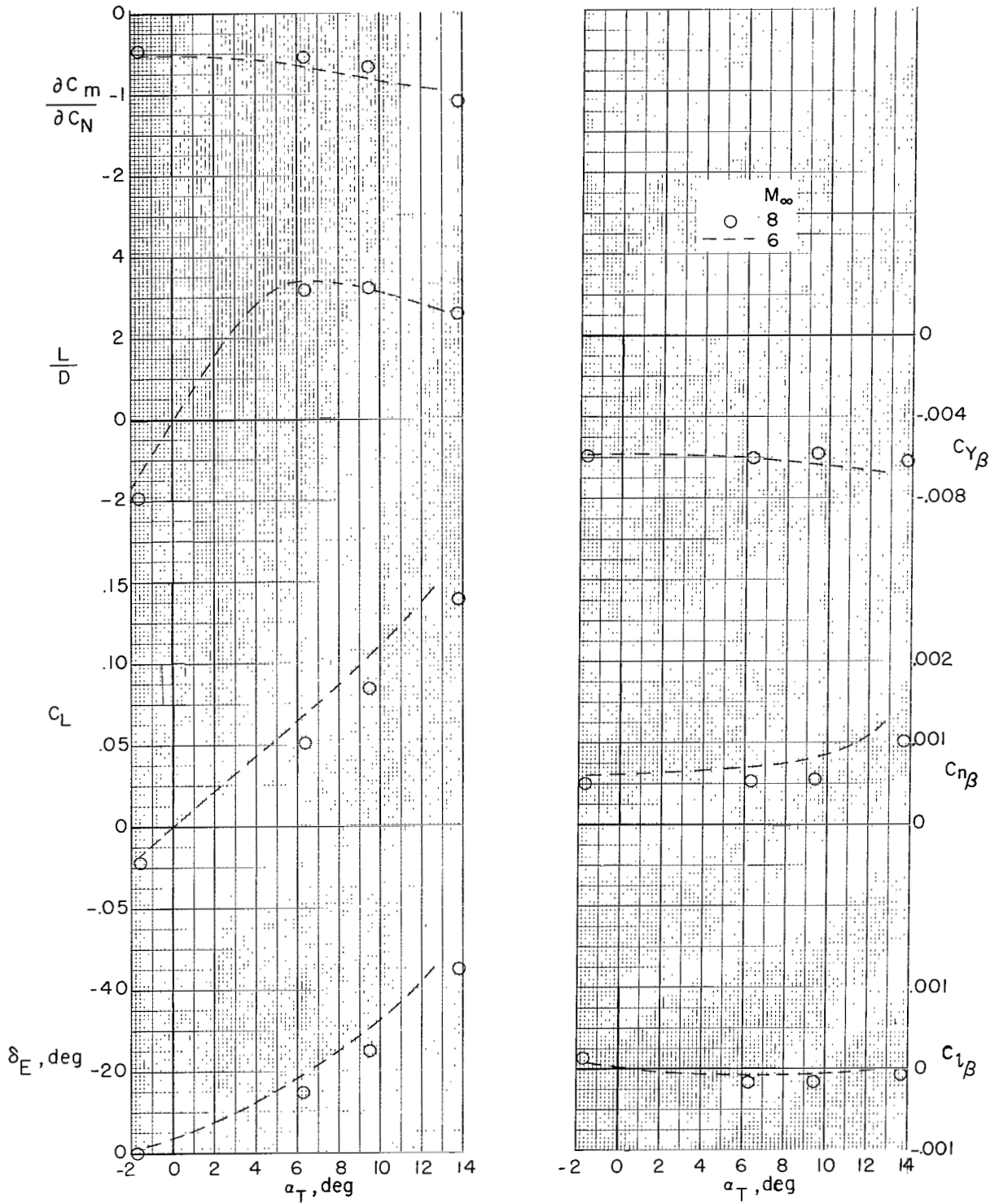
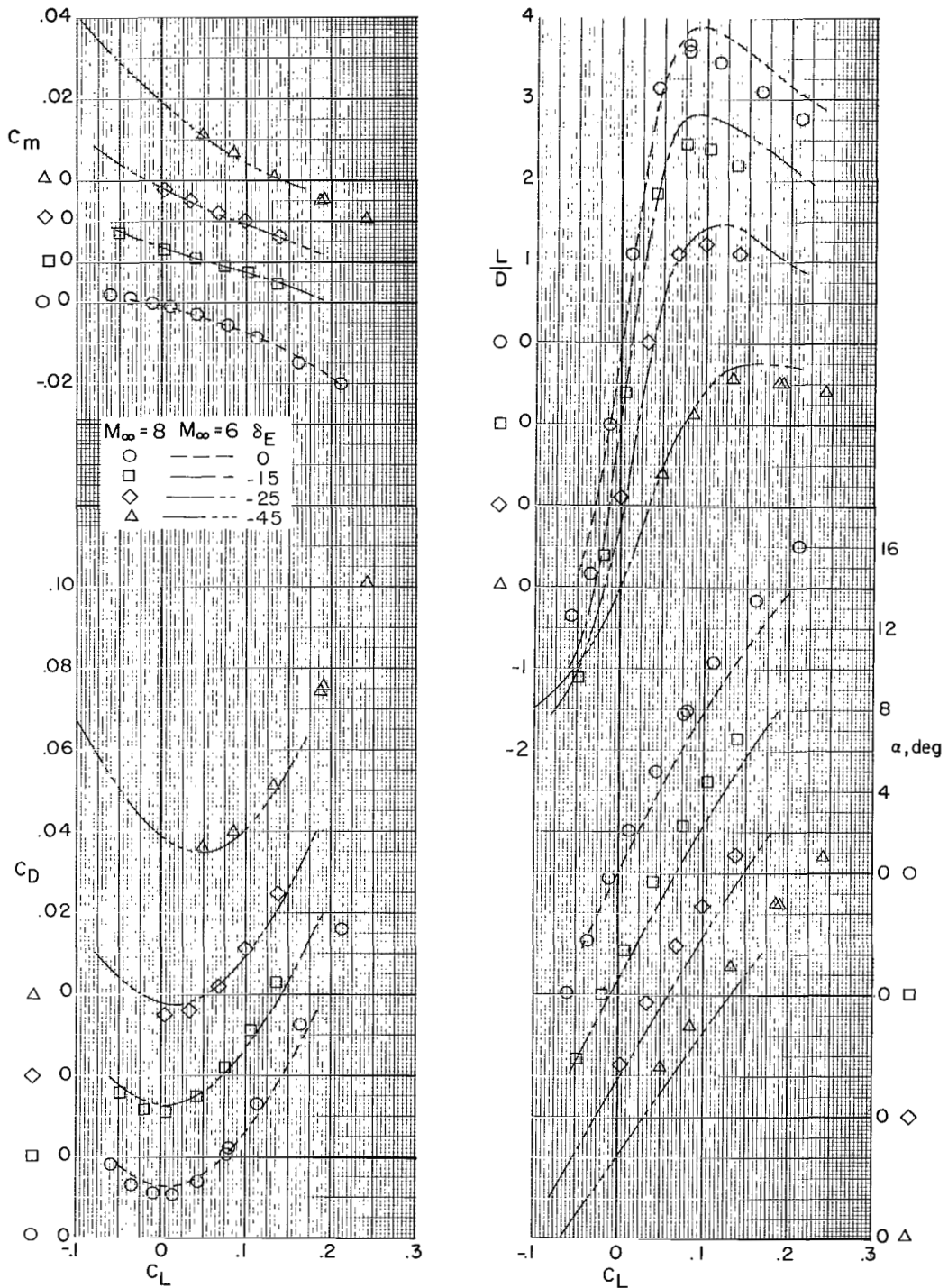
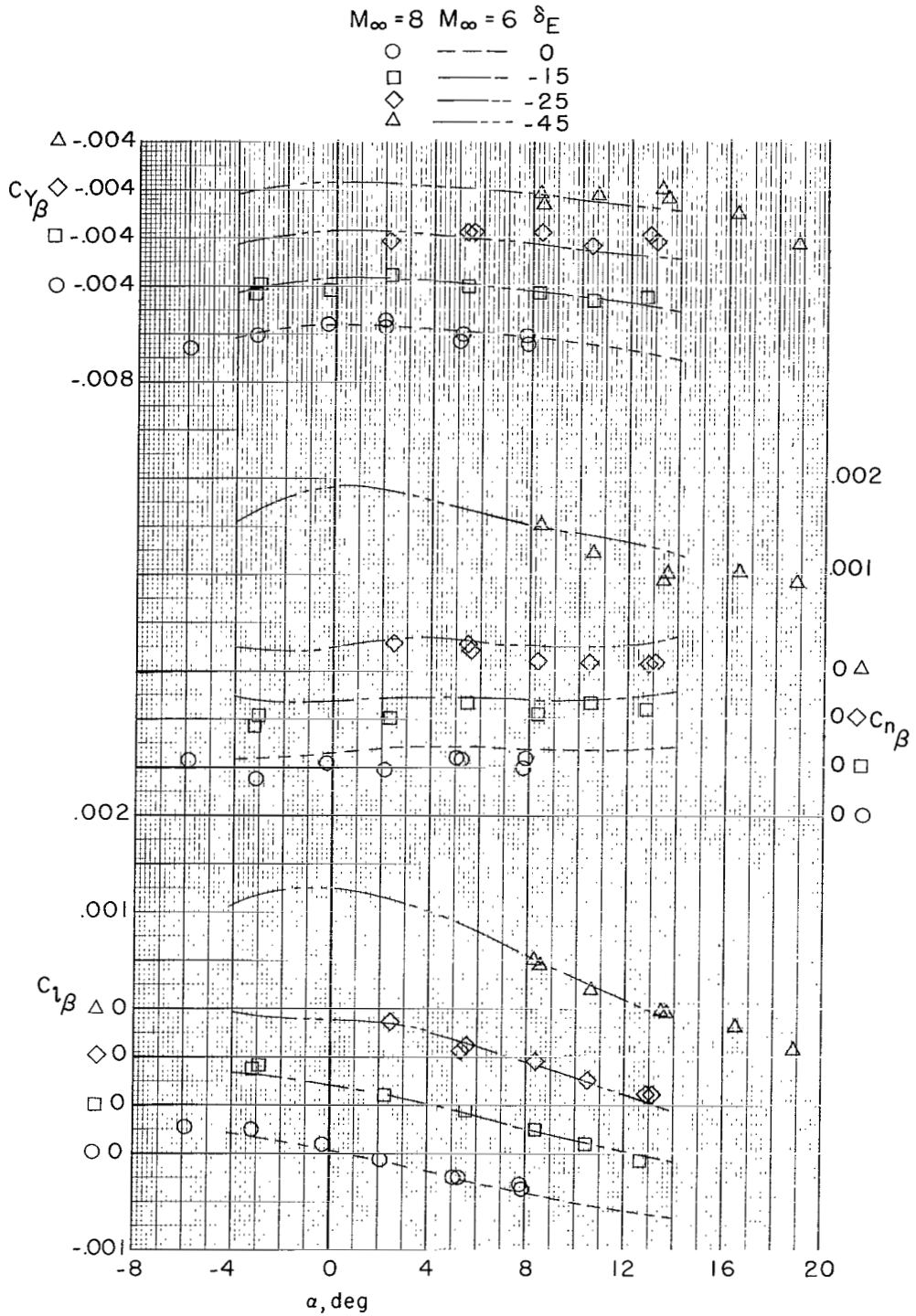


Figure 11.- Effect of Mach number on trimmed longitudinal, lateral, and directional stability characteristics of model 1 (BX₂W₂E₂V_UV_LV_{T,4}) with wing in midposition.



(a) Longitudinal characteristics.

Figure 12.- Effect of Mach number on aerodynamic characteristics of model 1 ($BX_2W_2E_2V_UV_LV_T,4$) with wing in midposition.



(b) Lateral and directional stability characteristics.

Figure 12.- Concluded.

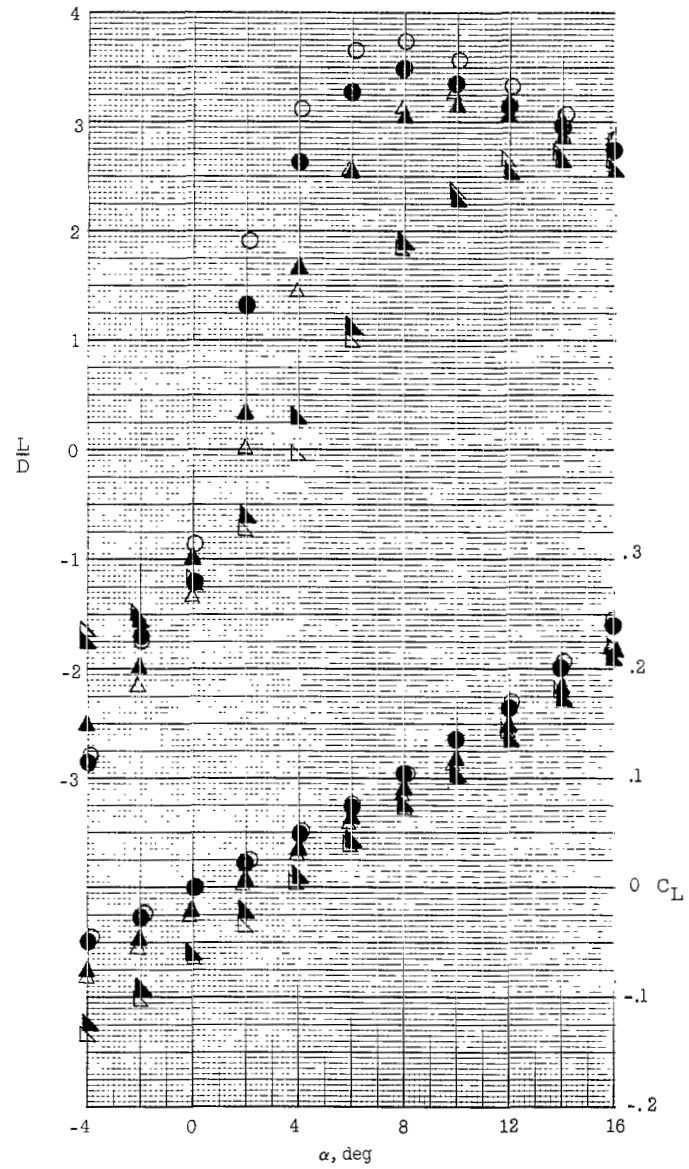
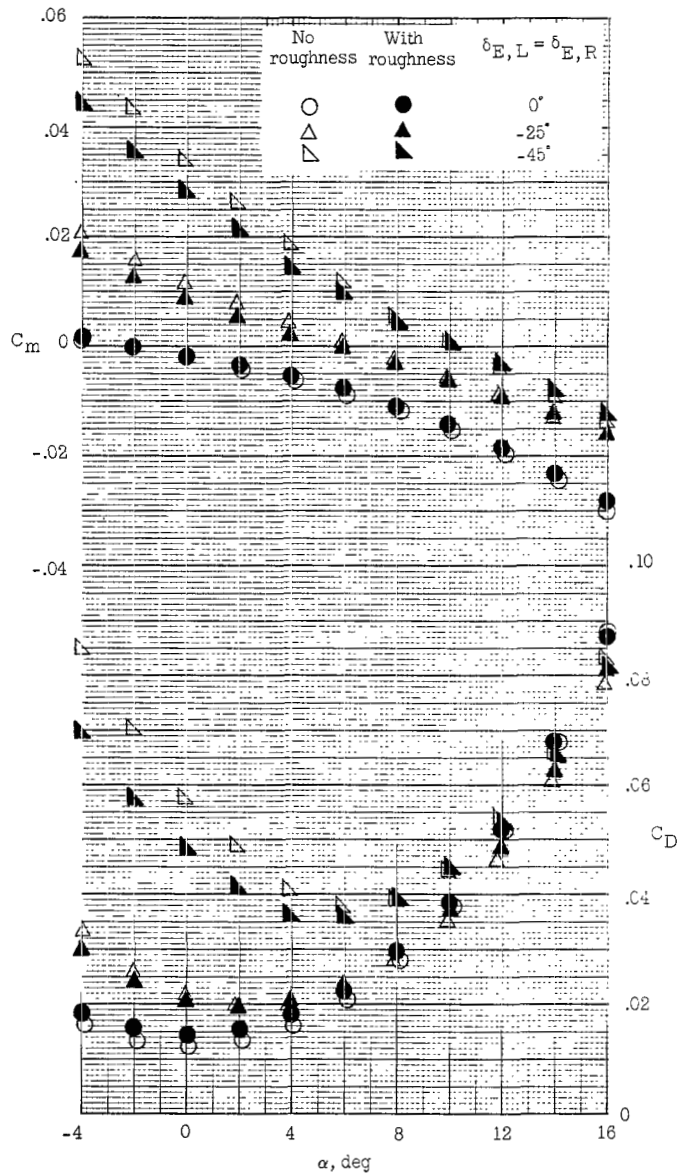
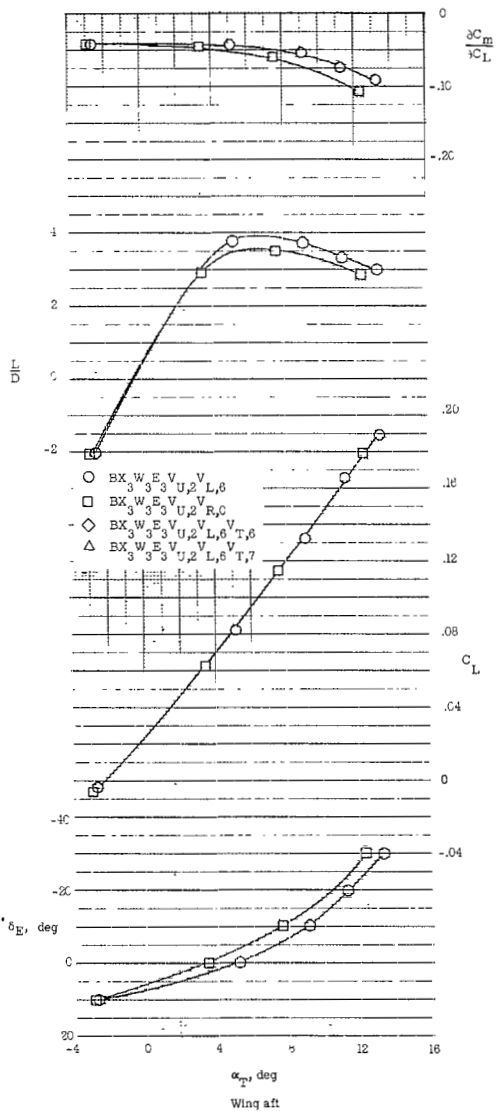
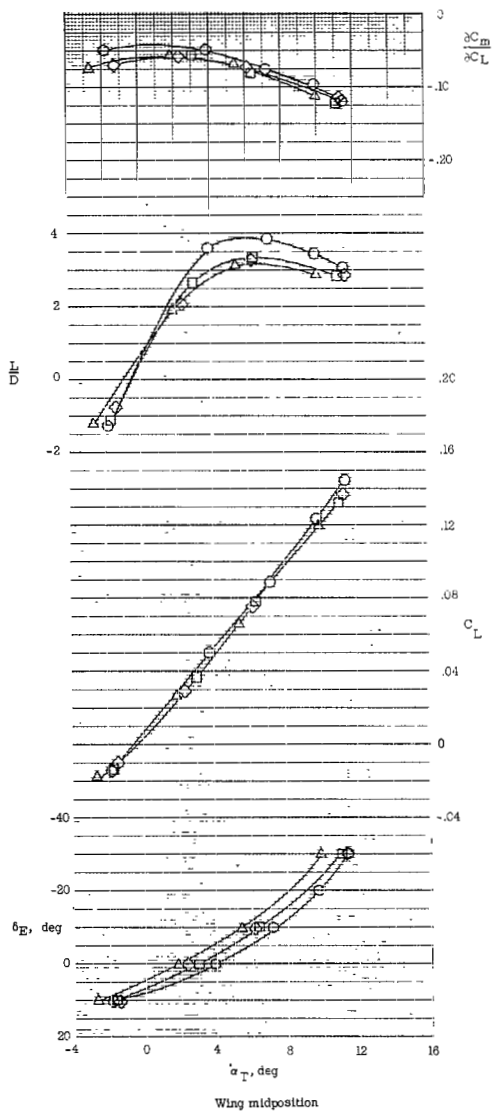
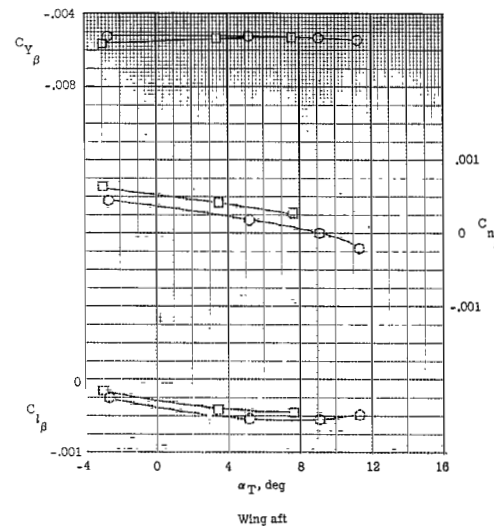
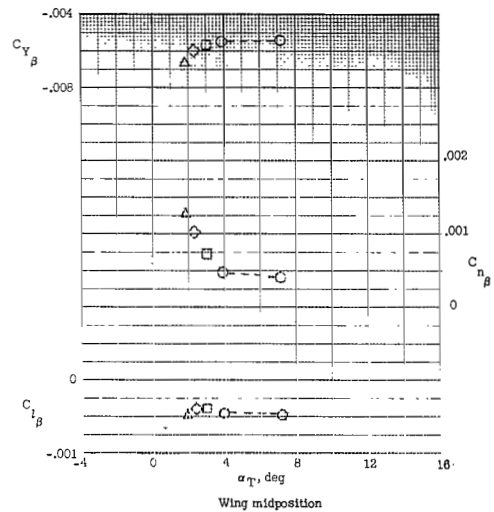


Figure 13.- Effect of roughness on longitudinal aerodynamic characteristics of model 1 ($BX_2W_2E_2V_UV_{L,2}V_{T,3}$) with wing in forward position. $M_\infty = 6$.

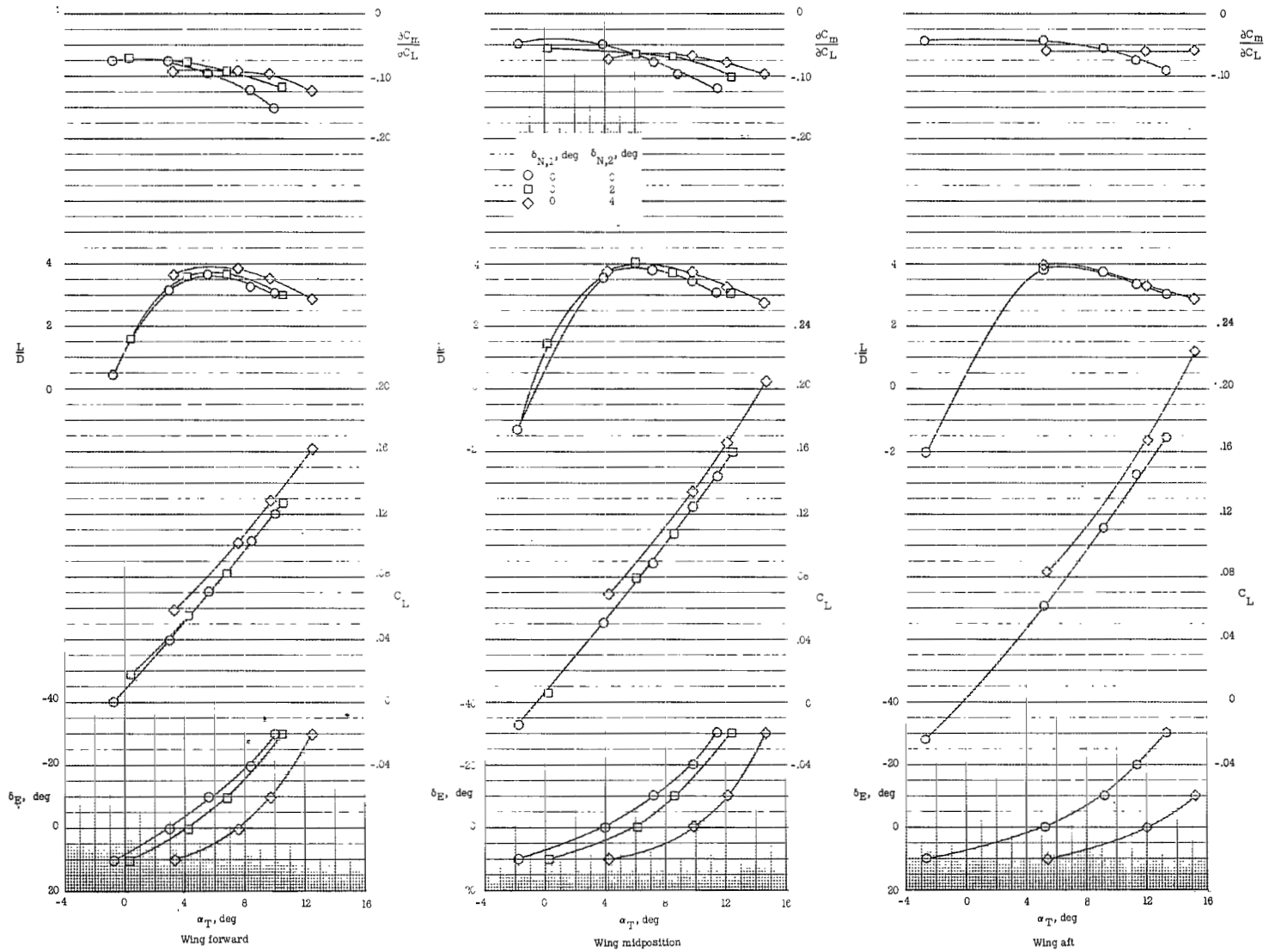


(a) Longitudinal characteristics.



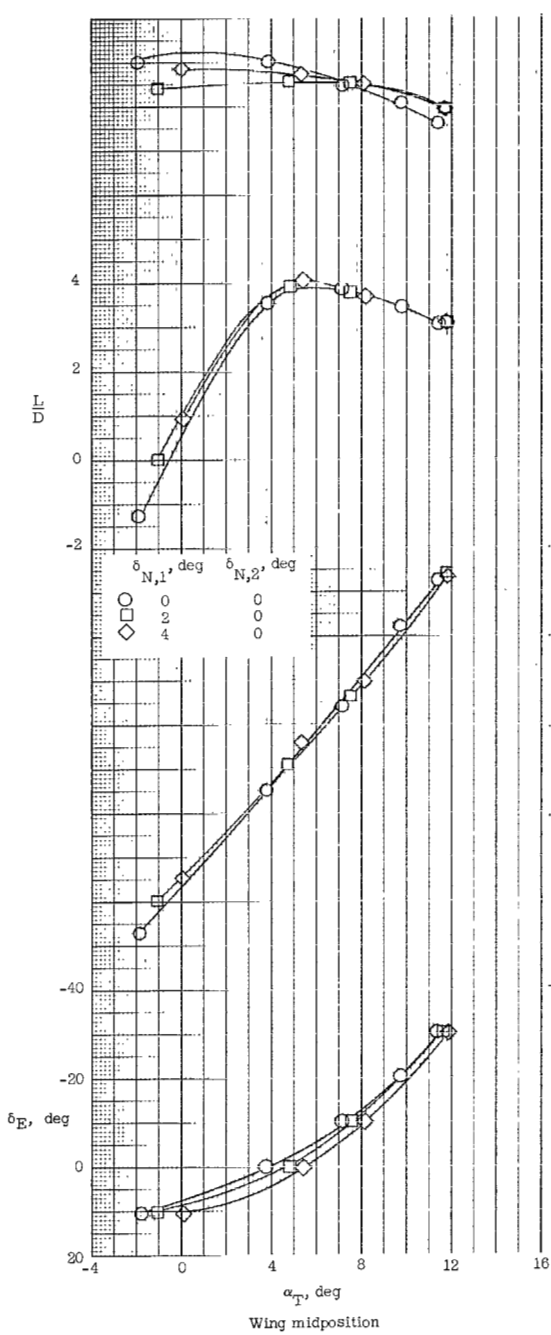
(b) Lateral and directional stability characteristics.

Figure 14.- Effect of component parts on trimmed aerodynamic characteristics of model 2. $M_{\infty} = 6$.



(a) $\delta_{N,2}$.

Figure 15.- Effect of nose cant on trimmed longitudinal aerodynamic characteristics of model 2 ($BX_3W_3E_3V_{U,2}V_{L,6}$). $M_\infty = 6$.



(b) $\delta_{N,1}$.

Figure 15.- Concluded.

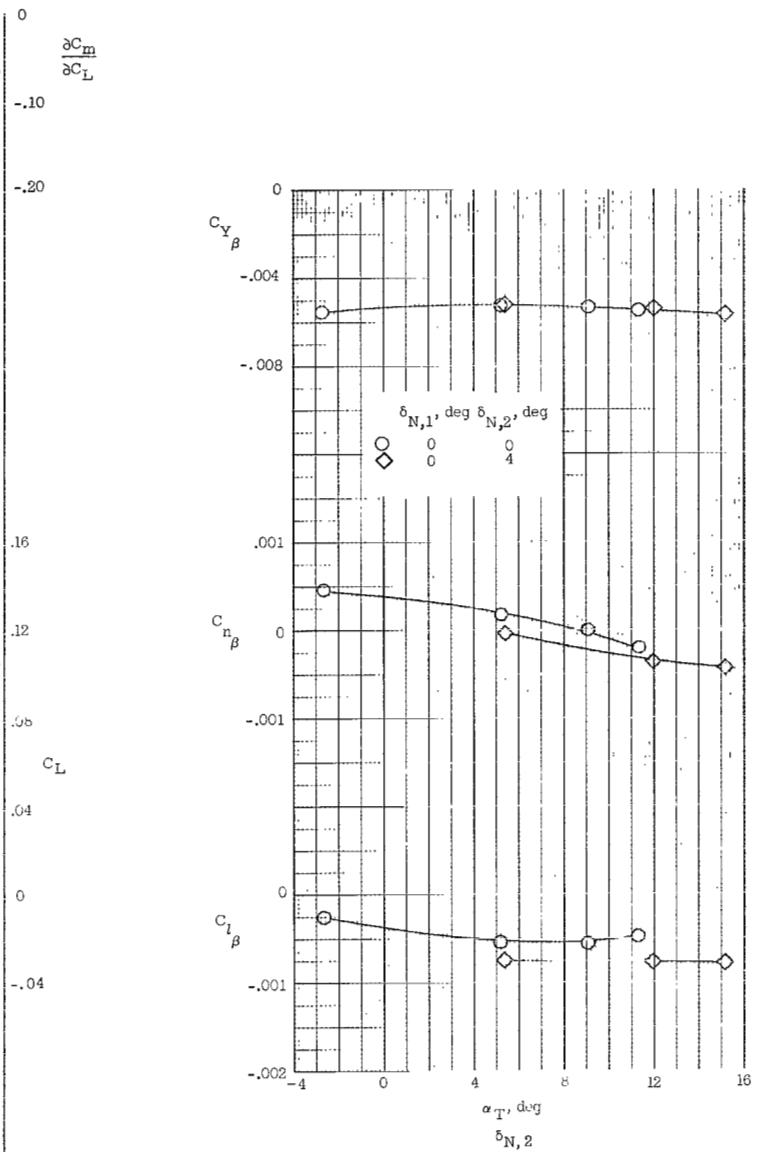


Figure 16.- Effect of nose cant on trimmed lateral and directional stability characteristics of model 2 (BX₃W₃E₃V_{U,2}V_{L,6}) with wing in aft position. $M_\infty = 6$.

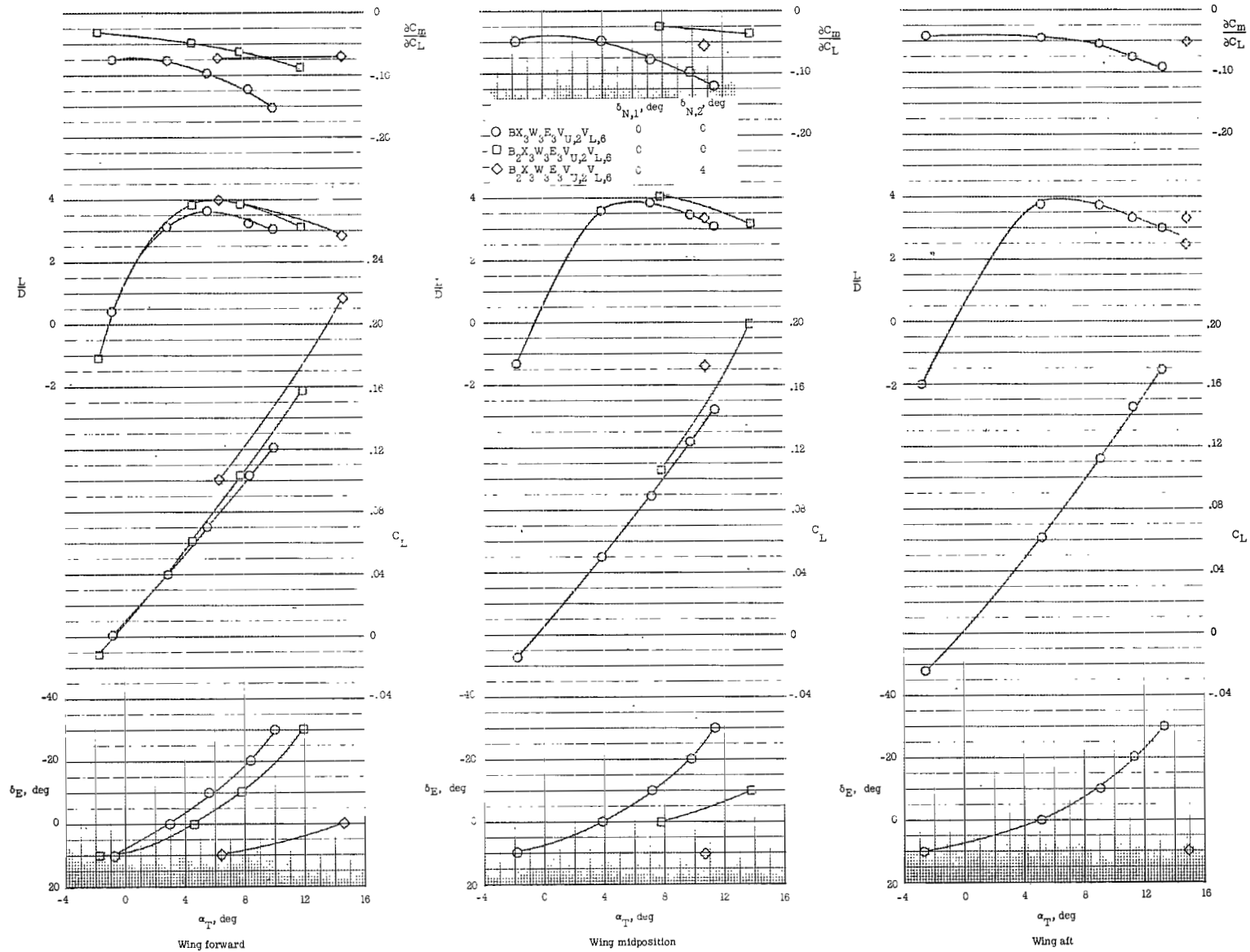
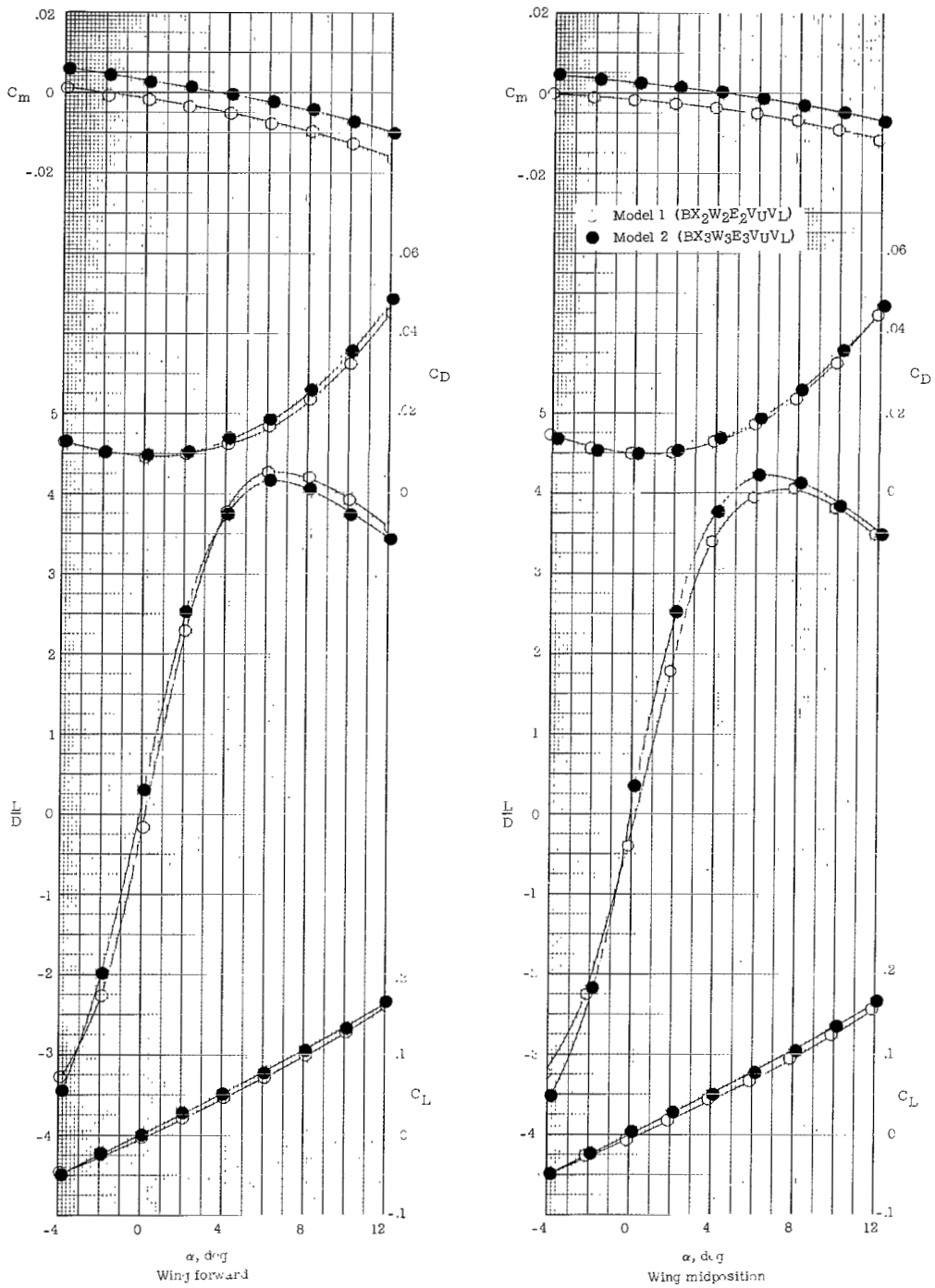
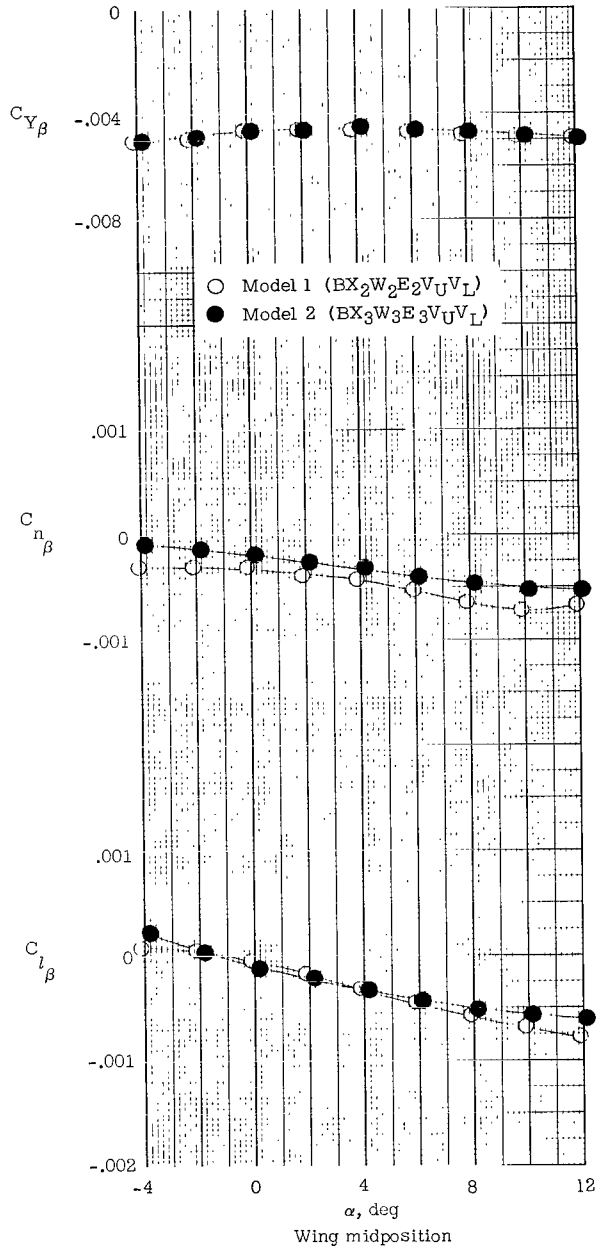
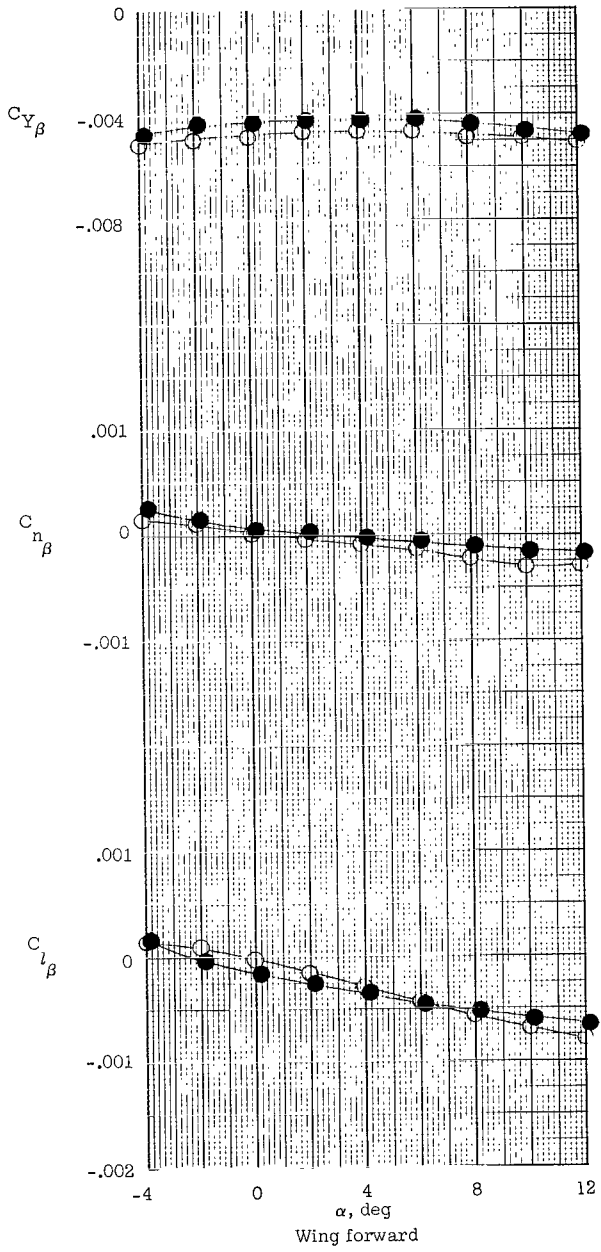


Figure 17.- Effect of strakes on trimmed longitudinal aerodynamic characteristics of model 2. $M_\infty = 6$.



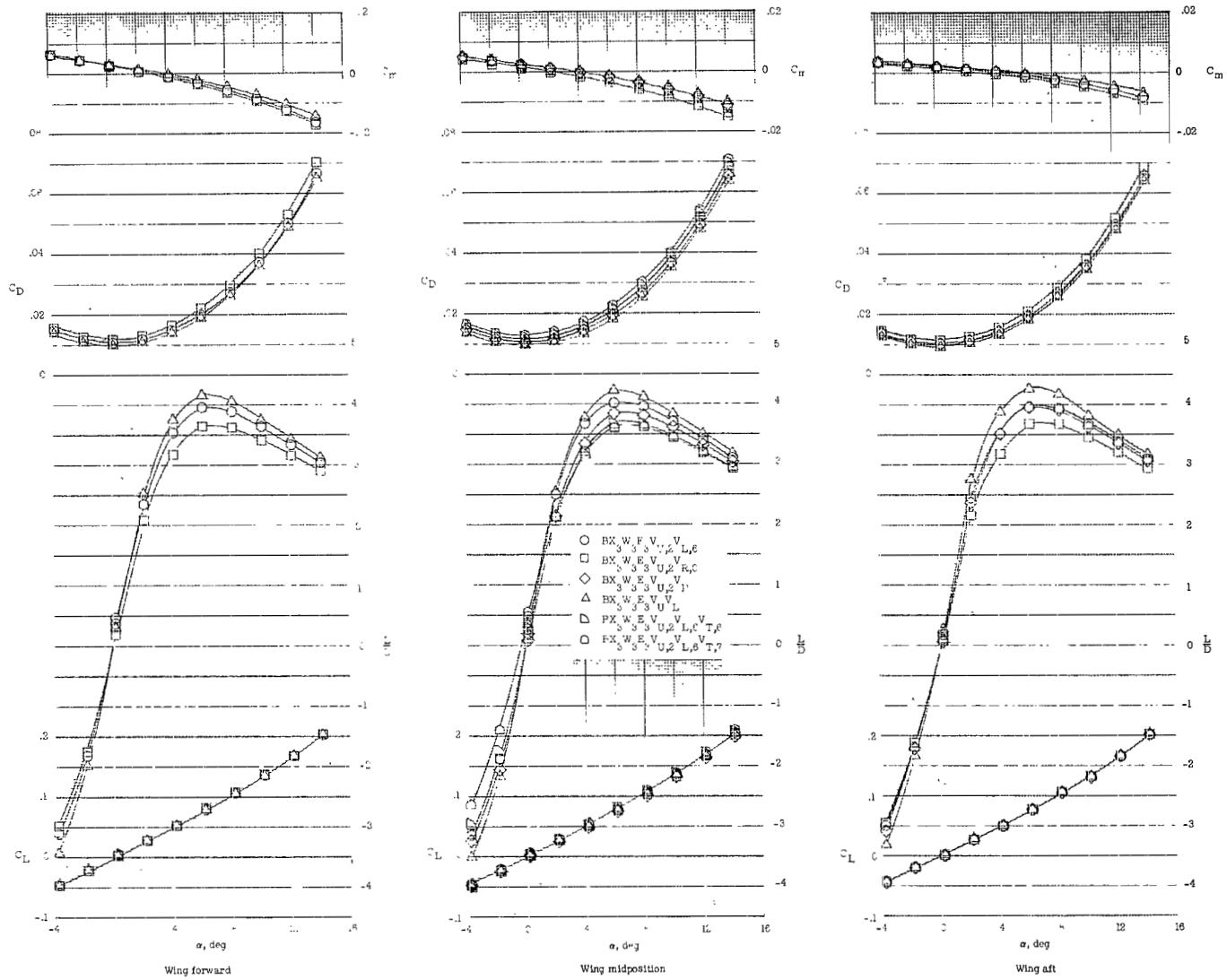
(a) Longitudinal characteristics.

Figure 18.- Effect of wing position on aerodynamic characteristics. $M_\infty = 6$; $\delta_E = 0^\circ$.



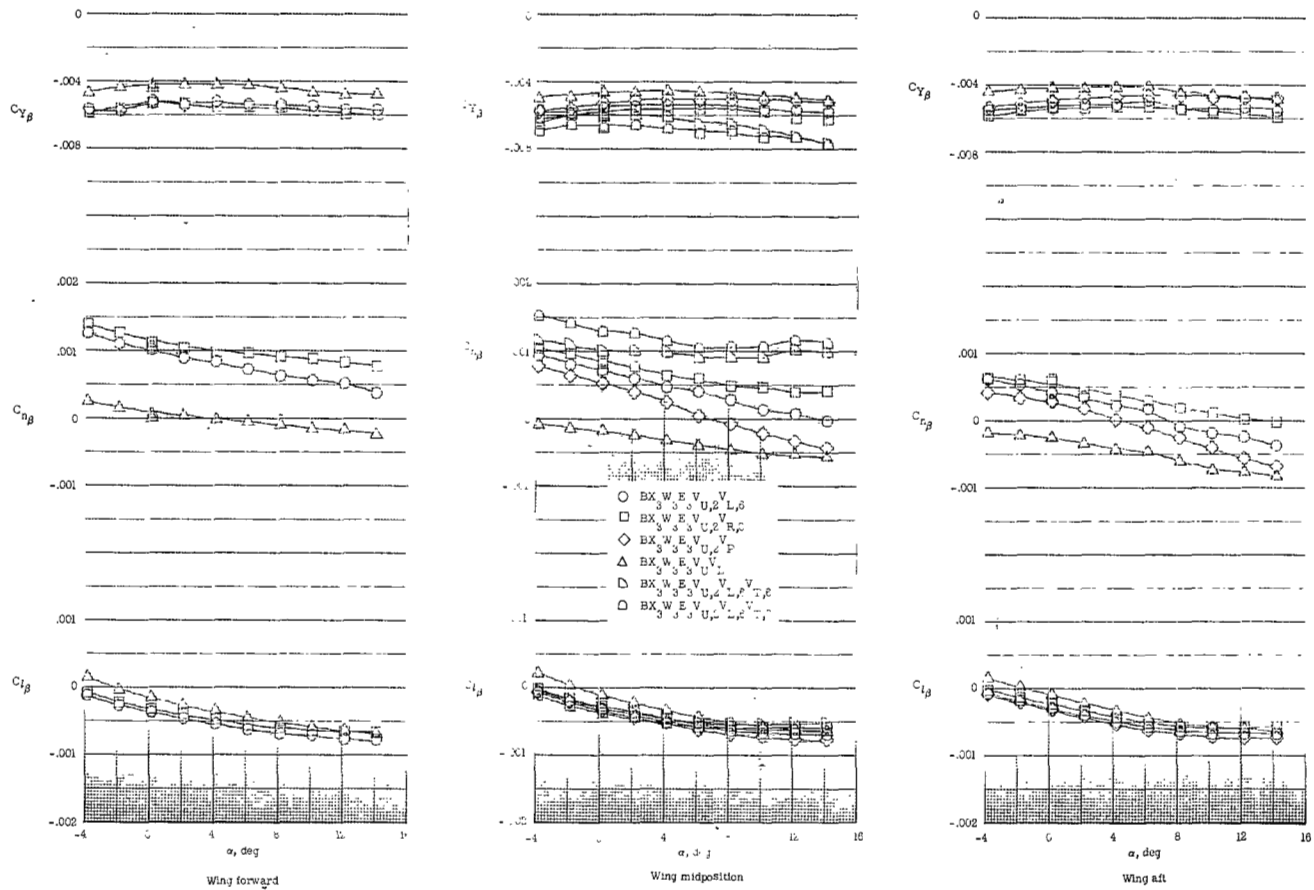
(b) Lateral and directional stability characteristics.

Figure 18.- Concluded.



(a) Longitudinal characteristics.

Figure 19.- Effect of component parts on aerodynamic characteristics of model 2. $M_\infty = 6$; $\delta_E = 0^\circ$.



(b) Lateral and directional stability characteristics.

Figure 19.- Concluded.

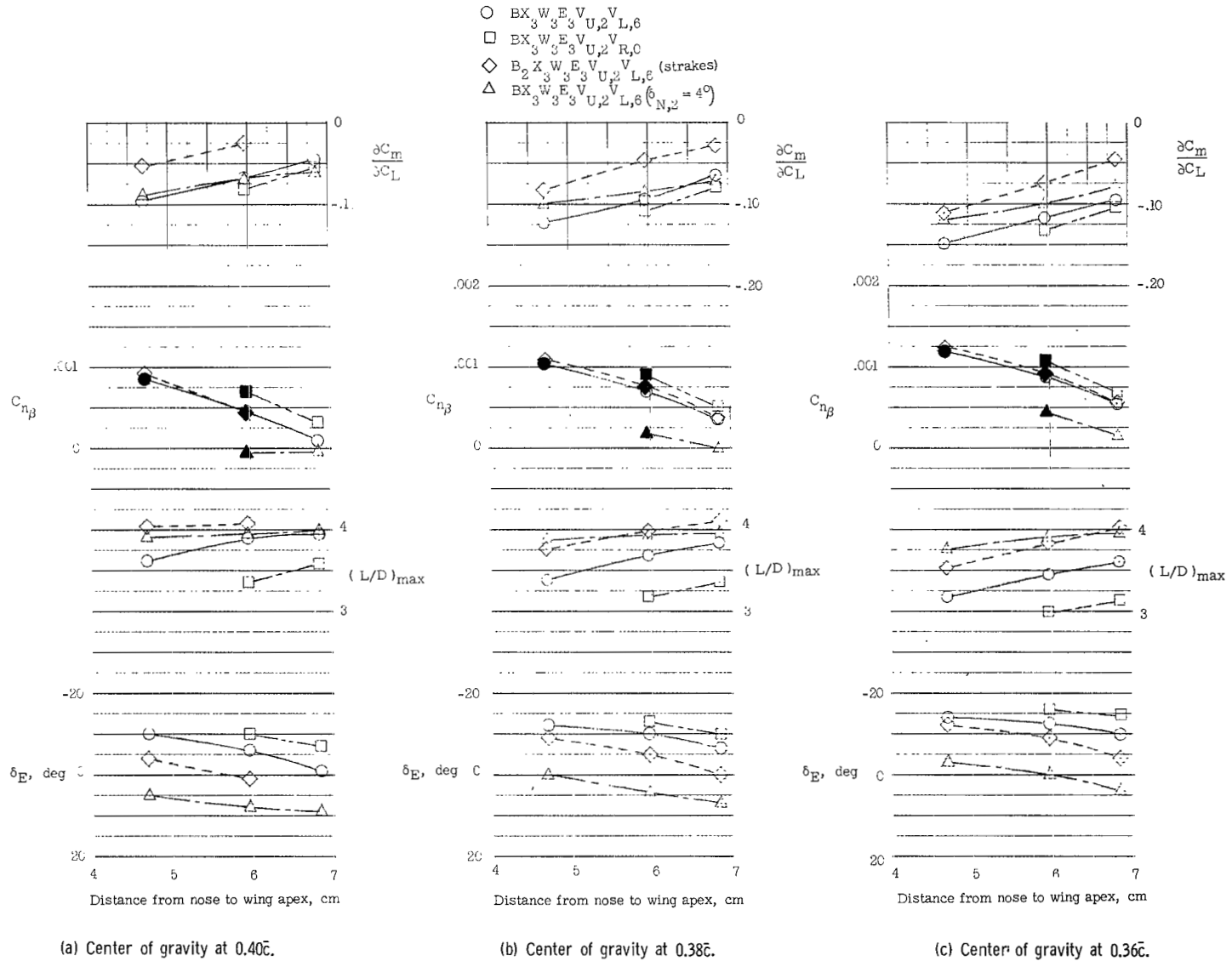


Figure 20.- Variation of aerodynamic characteristics at maximum trimmed L/D with longitudinal wing position and center-of-gravity location for model 2. $M_\infty = 6$; solid symbols represent trimmed data at $\delta_E = 0^\circ$ only.

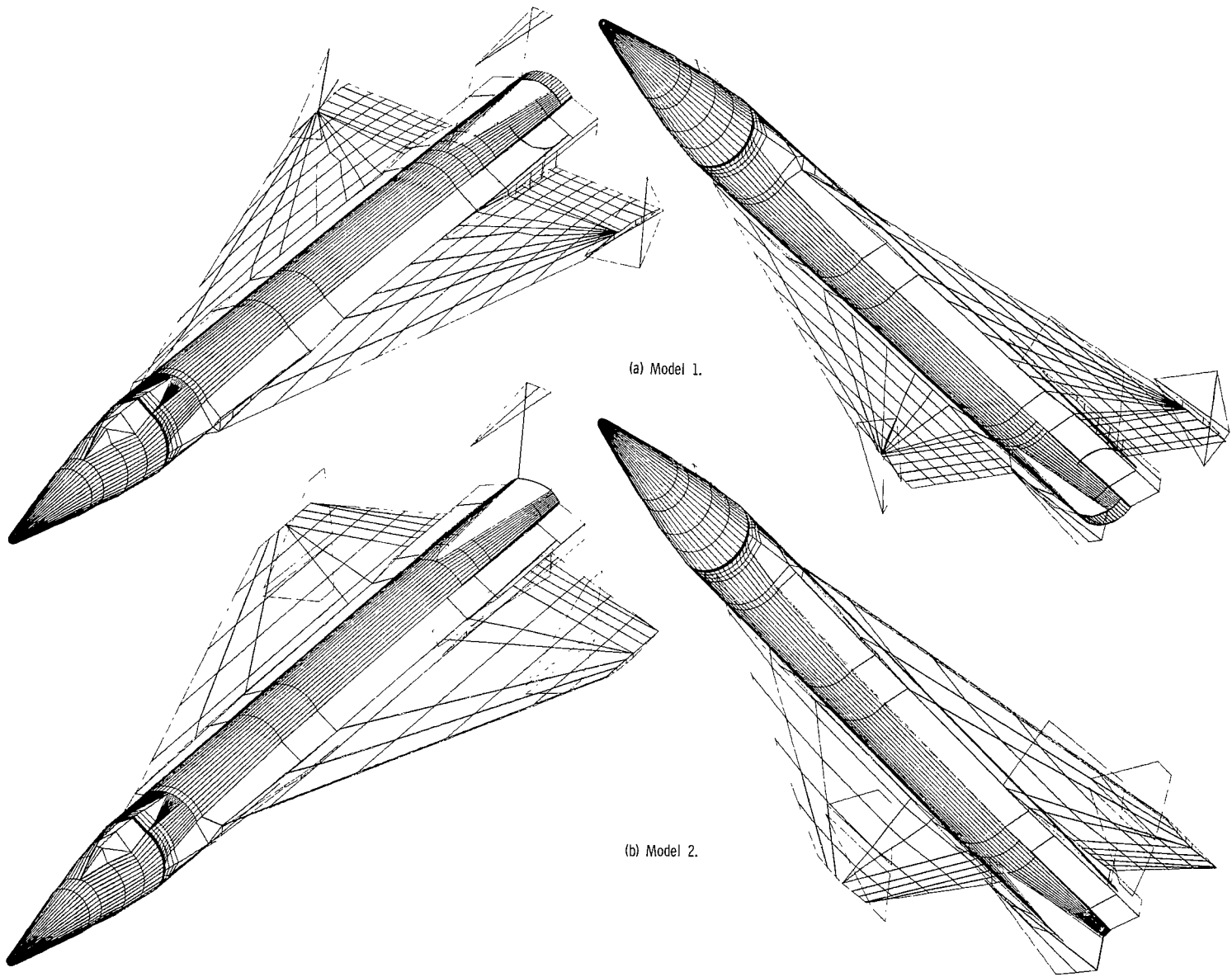
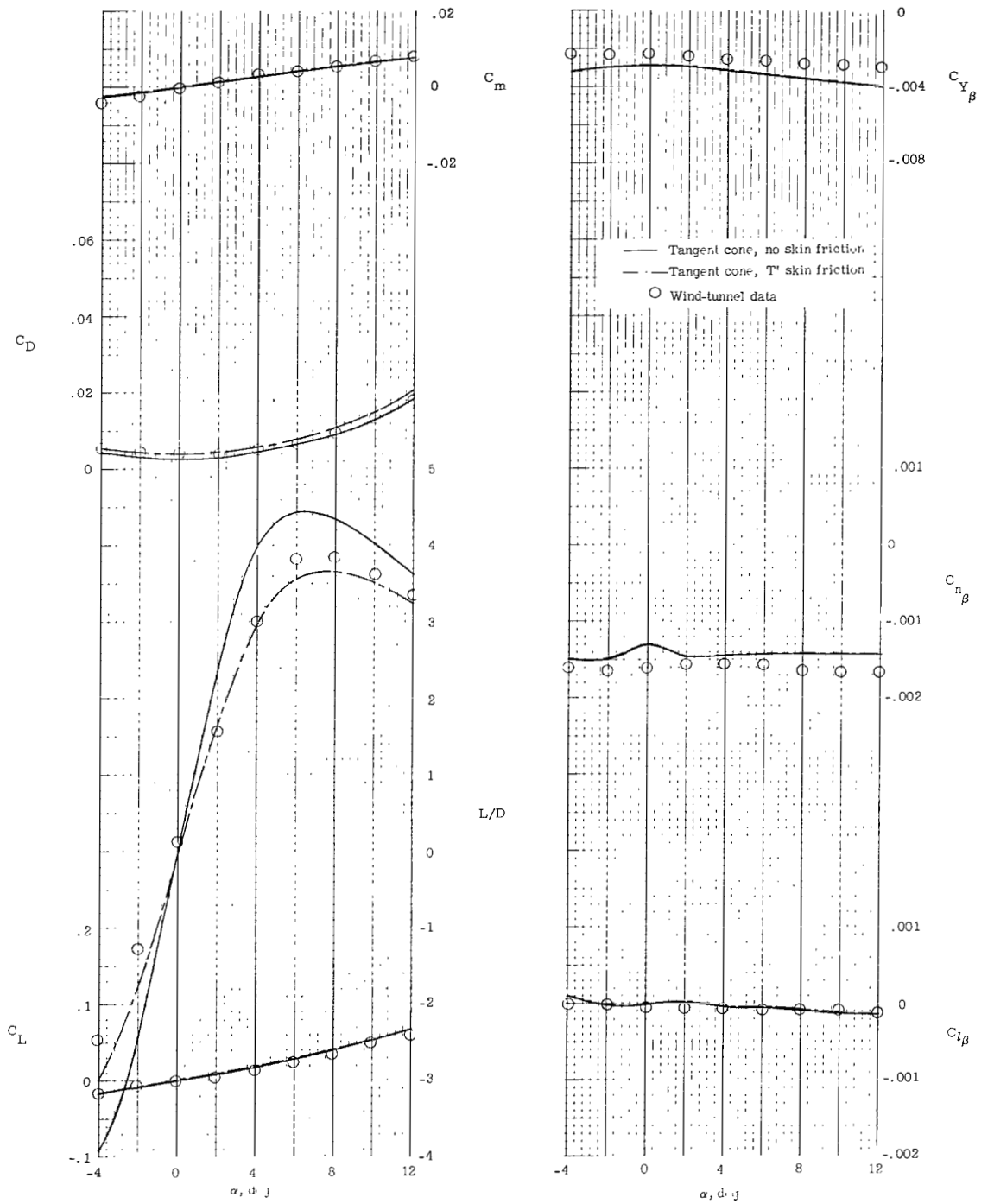
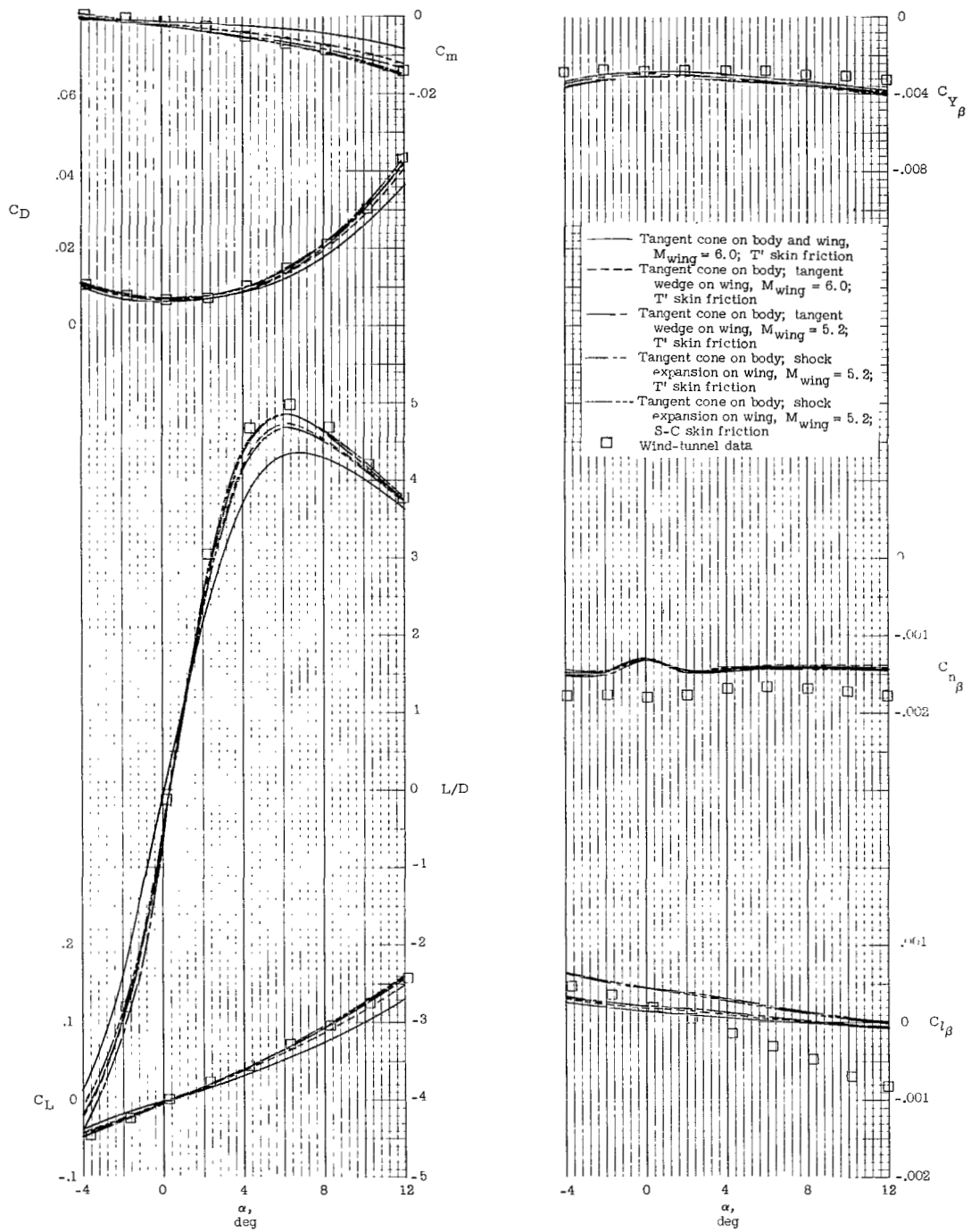


Figure 21.- Typical computer drawings of input geometry showing two isometric views of each model.



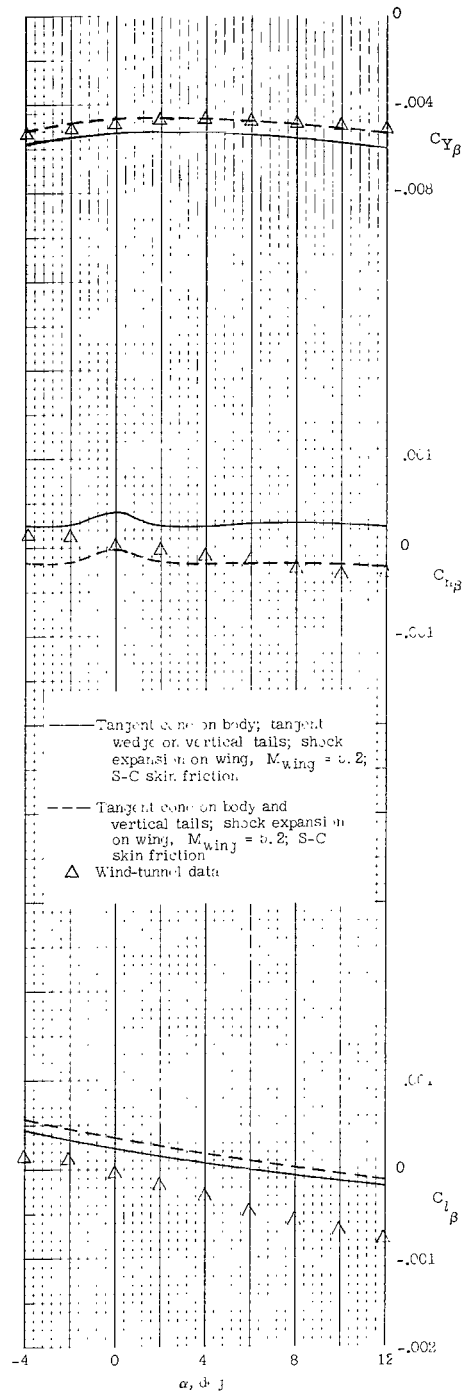
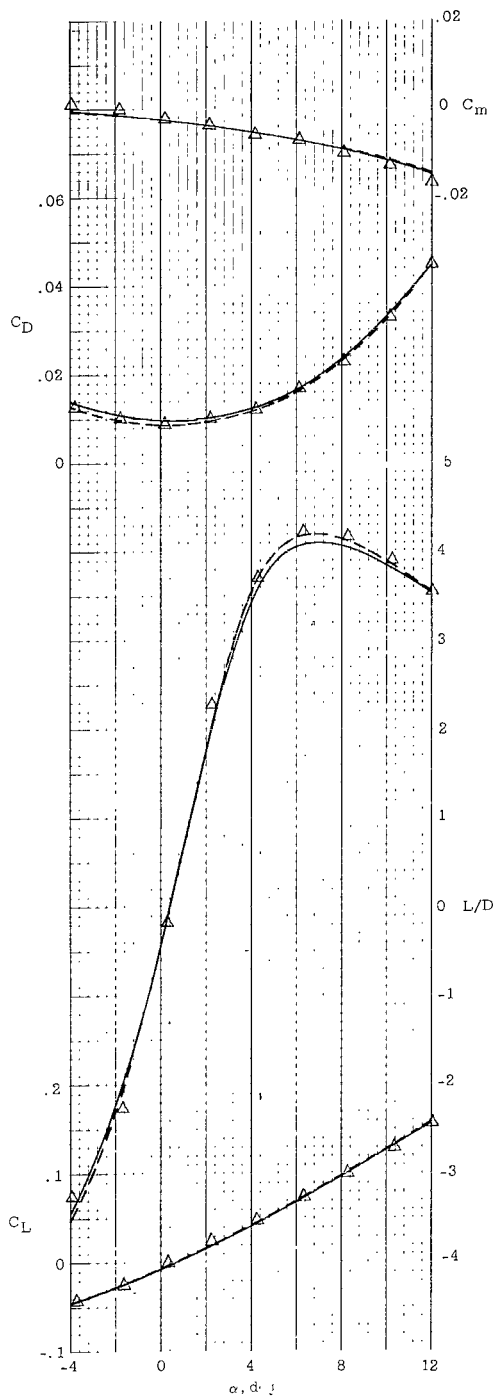
(a) BX₂.

Figure 22.- Comparison of computer program results with wind-tunnel data for component buildup of model I. Wing in forward position; center of gravity at 0.40C.



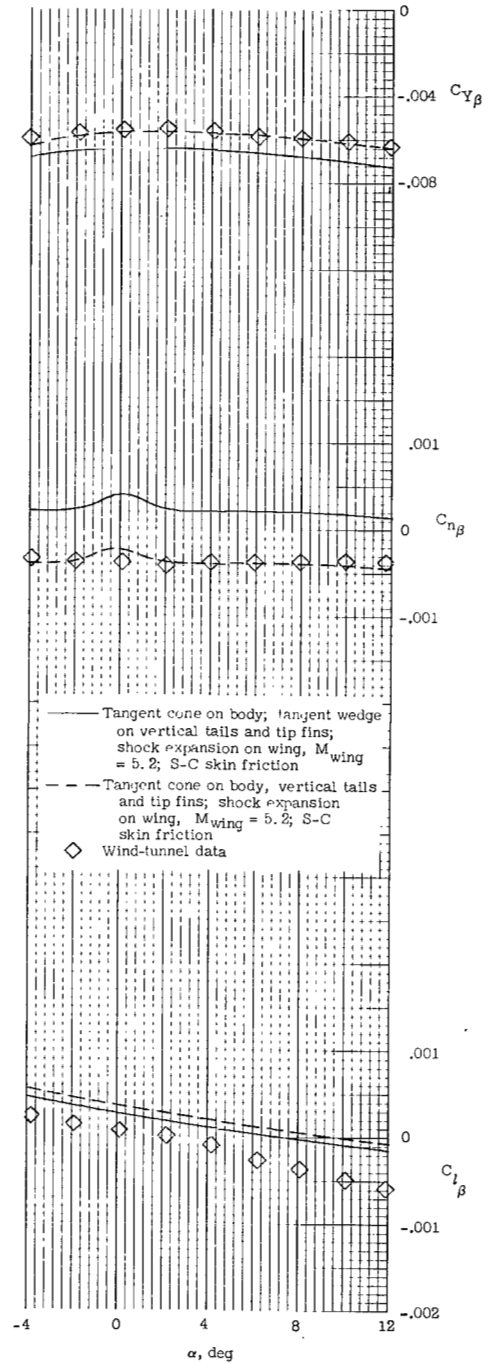
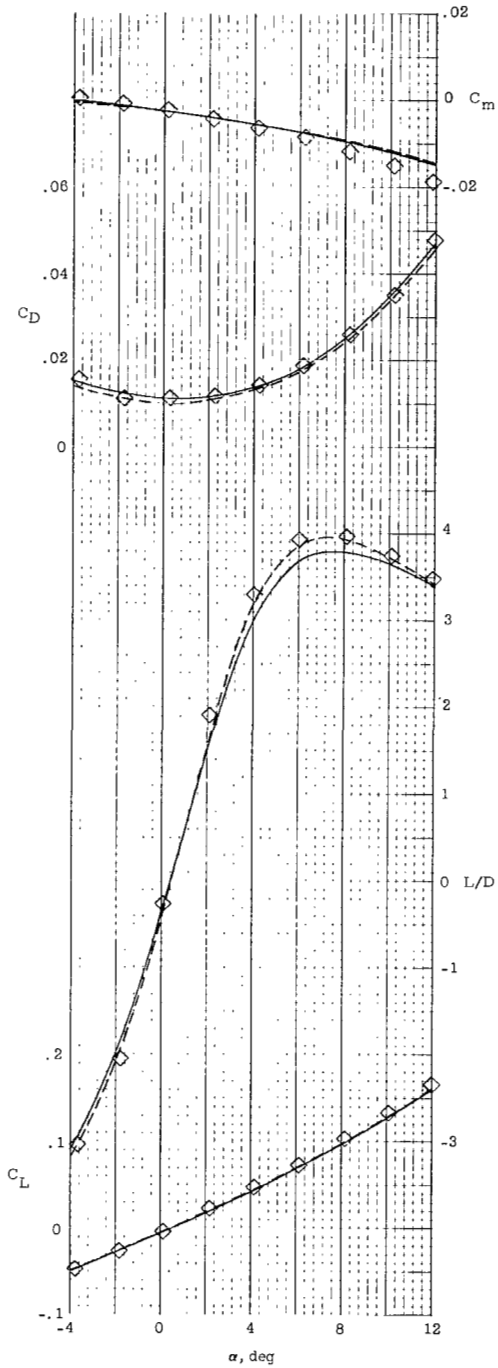
(b) BX₂W₂E₂.

Figure 22.- Continued.



(c) $BX_2W_2E_2V_1V_L$.

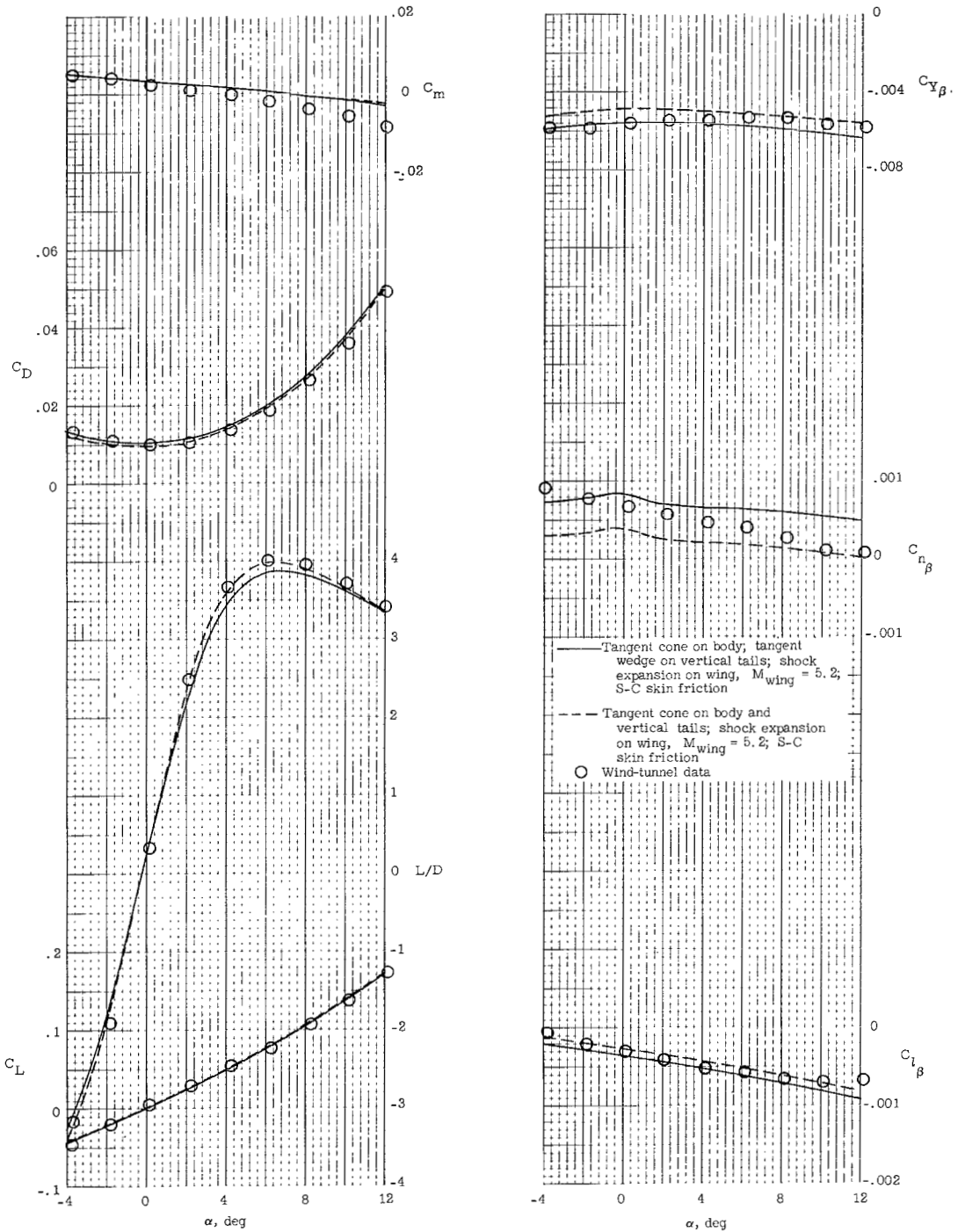
Figure 22.- Continued.



— Tangent cone on body, tangent wedge on vertical tails and tip fins; shock expansion on wing, $M_{wing} = 5.2$; S-C skin friction
 - - - Tangent cone on body, vertical tails and tip fins; shock expansion on wing, $M_{wing} = 5.2$; S-C skin friction
 ◇ Wind-tunnel data

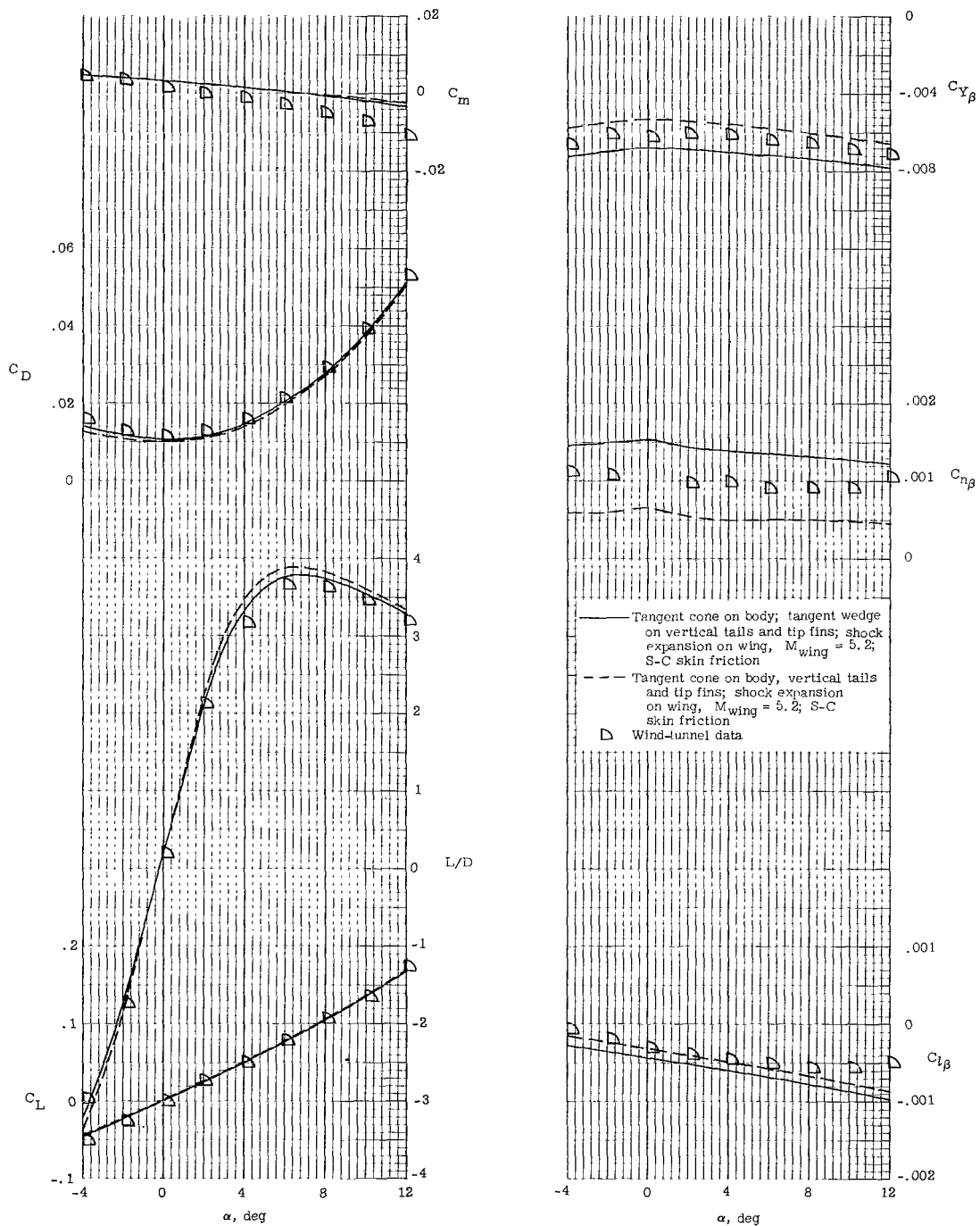
(d) BX₂W₂E₂V_UV_LV_{T,3}.

Figure 22.- Concluded.



(a) $BX_3W_3E_3V_{U,2}^VL_6$

Figure 23.- Comparison of machine calculations and experimental data for model 2 with large vertical tails and wing in midposition. Center of gravity at $0.40\bar{c}$.



(b) BX₃W₃E₃V_{U,2}V_{L,6}V_{T,6}

Figure 23.- Concluded.

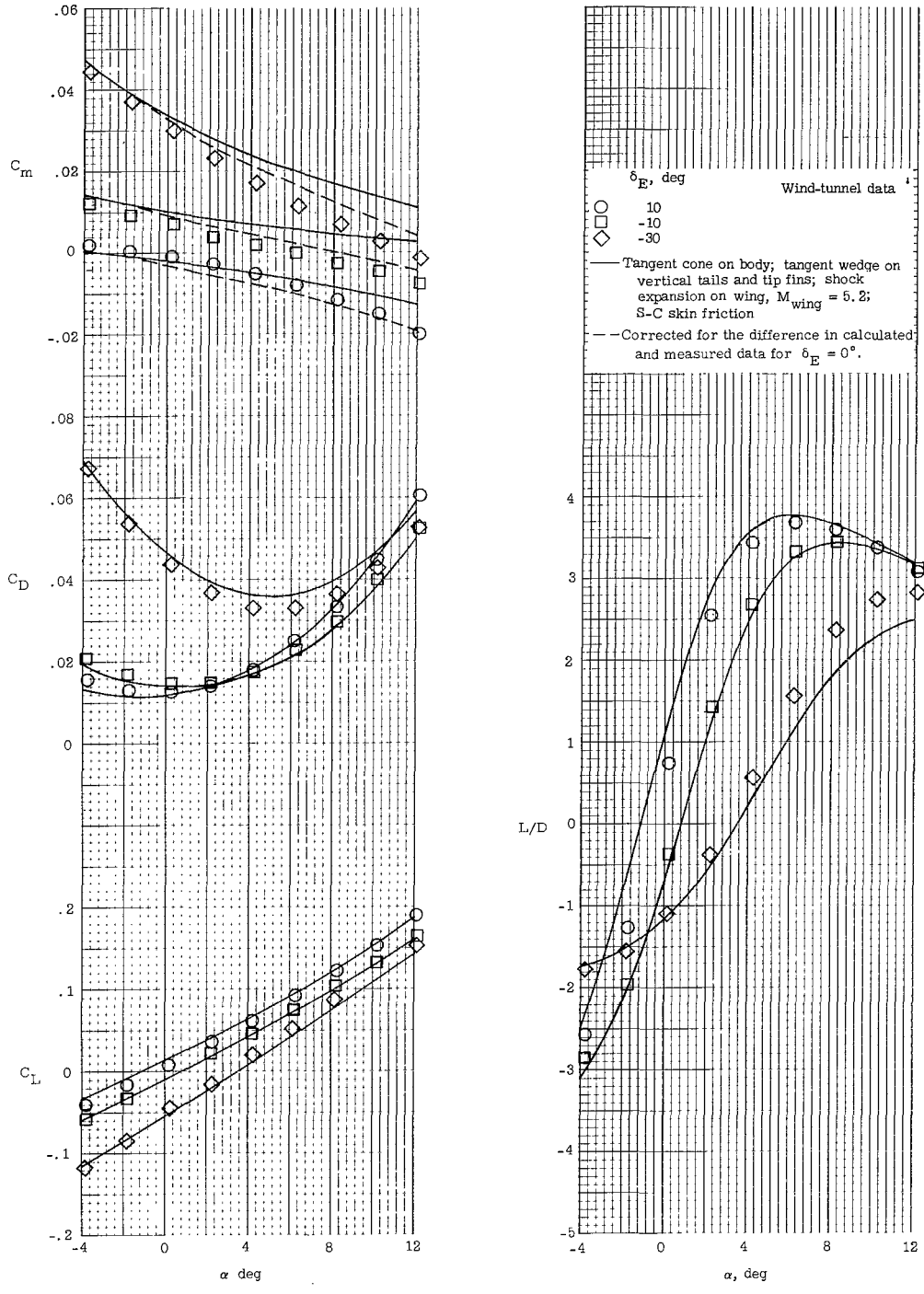
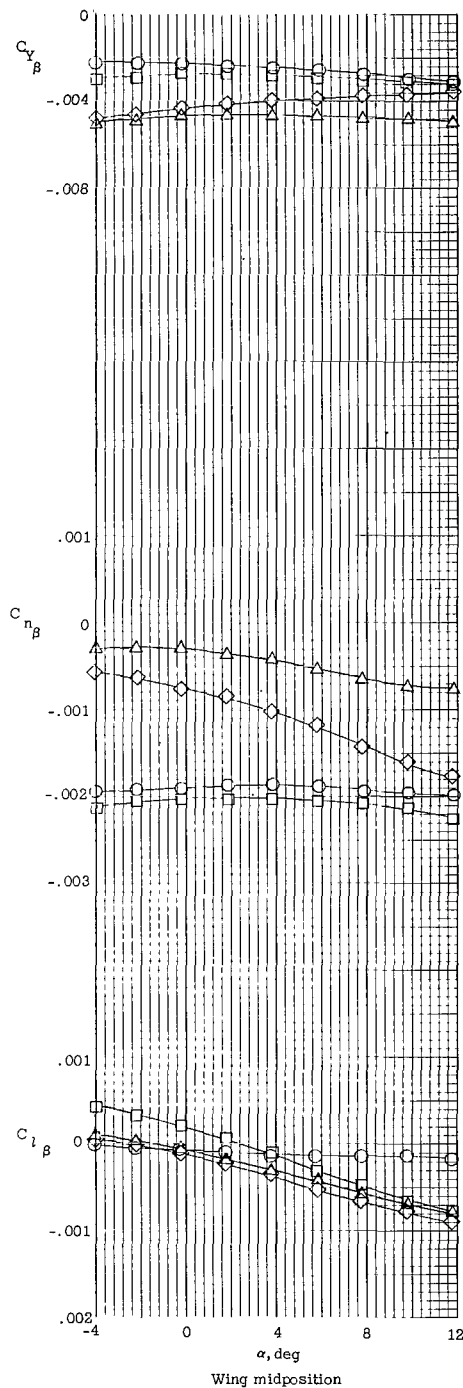
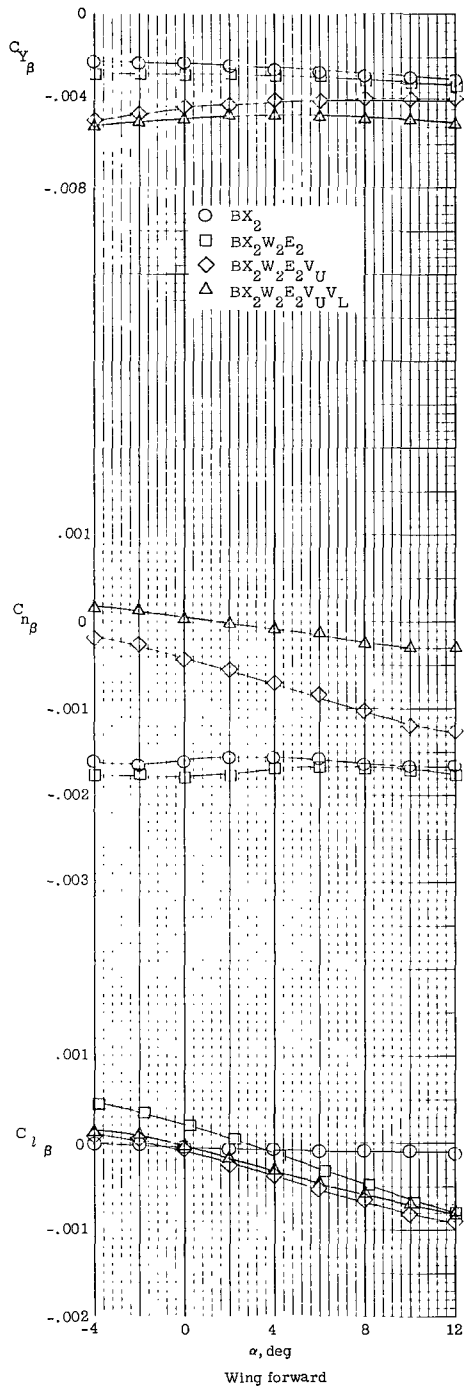
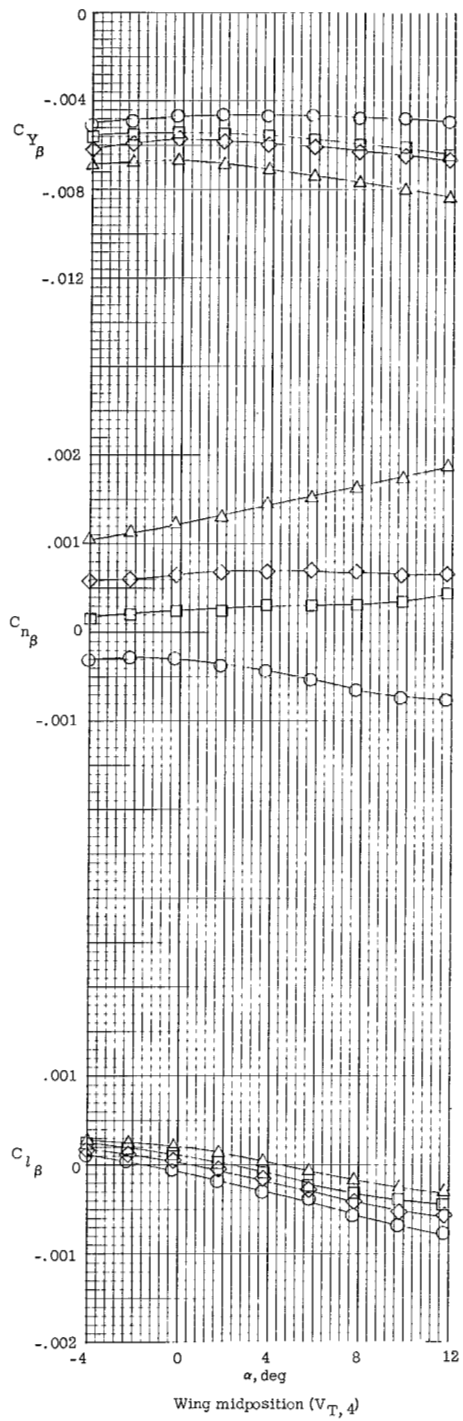
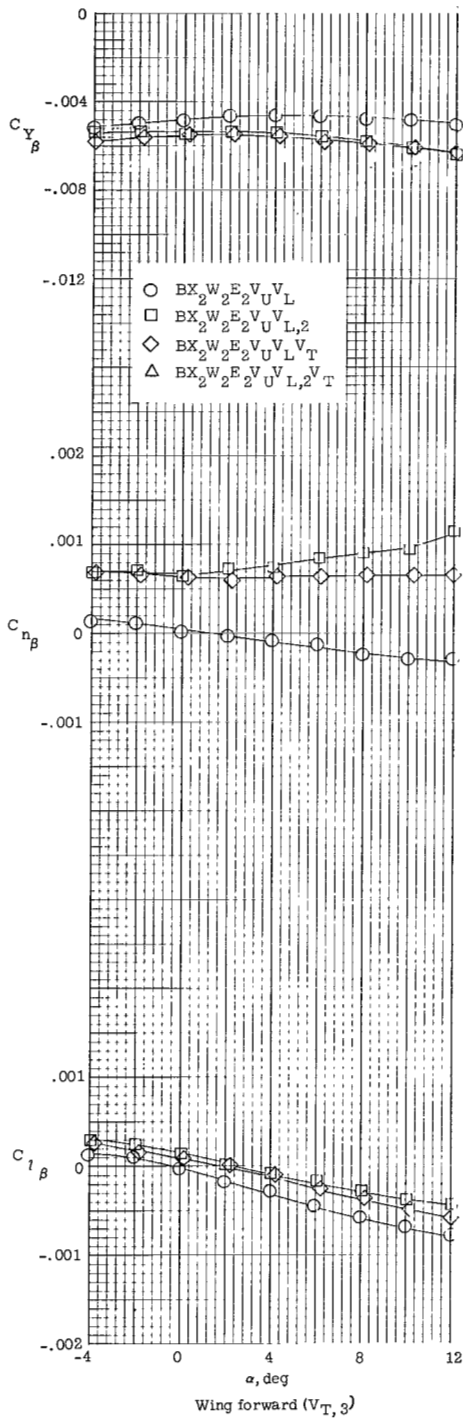


Figure 24.- Comparison of machine calculations and wind-tunnel data for effect of elevon deflection angle for model 2. Wing in midposition; center of gravity at 0.40C.



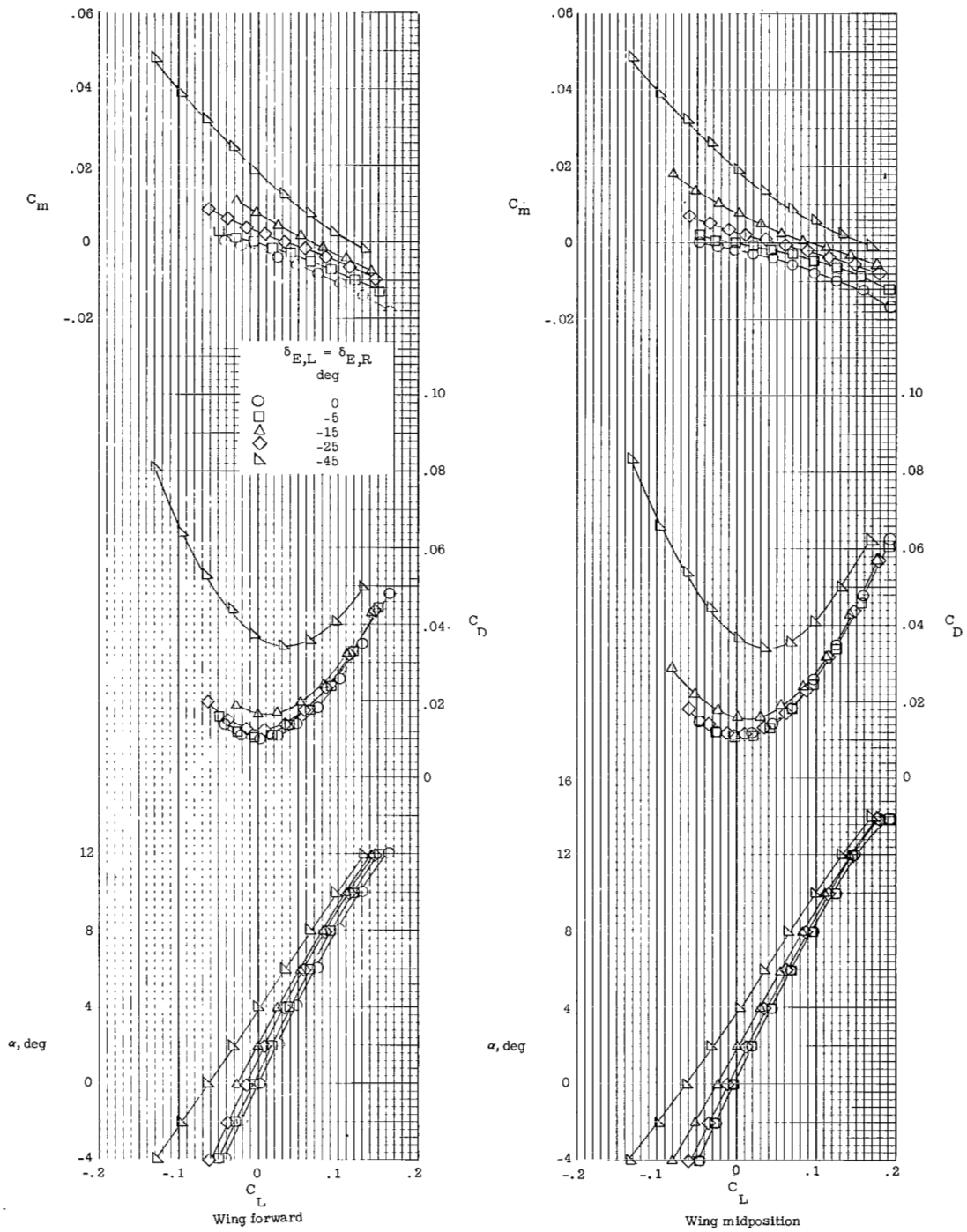
(a) Side fairing, wing, upper vertical tail, and lower vertical tail.

Figure 25.- Effect of component parts on lateral and directional stability characteristics of model 1. $M_\infty = 6$; $\delta_{E,L} = \delta_{E,R} = \delta_{V,U} = \delta_{V,L,2} = 0^\circ$.



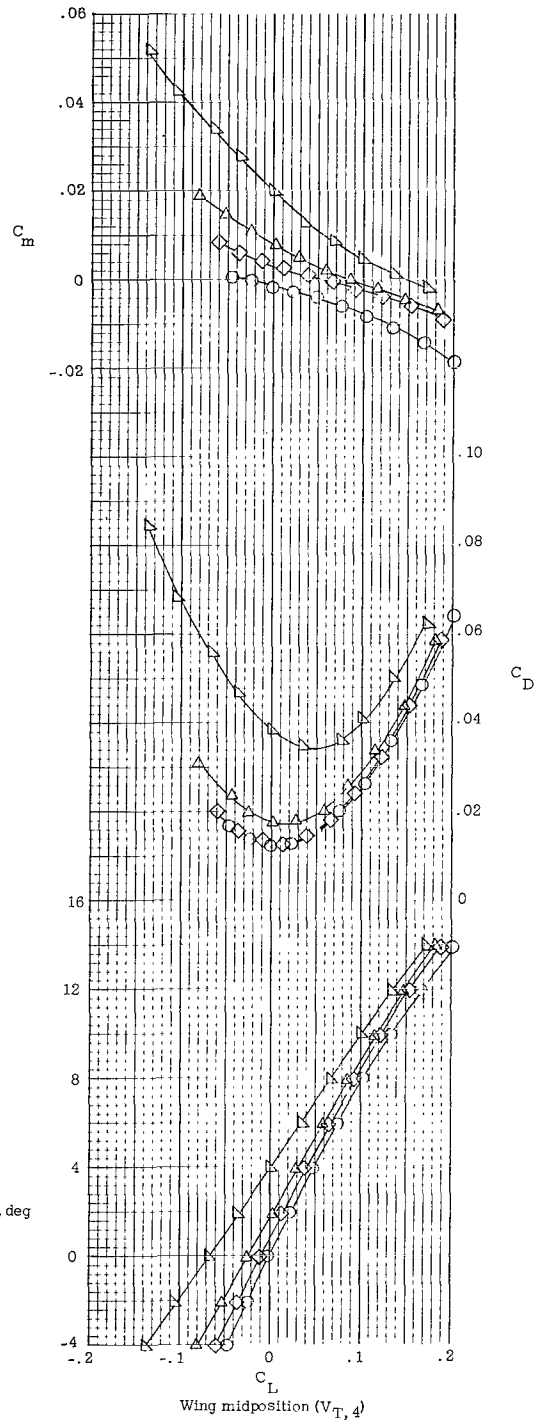
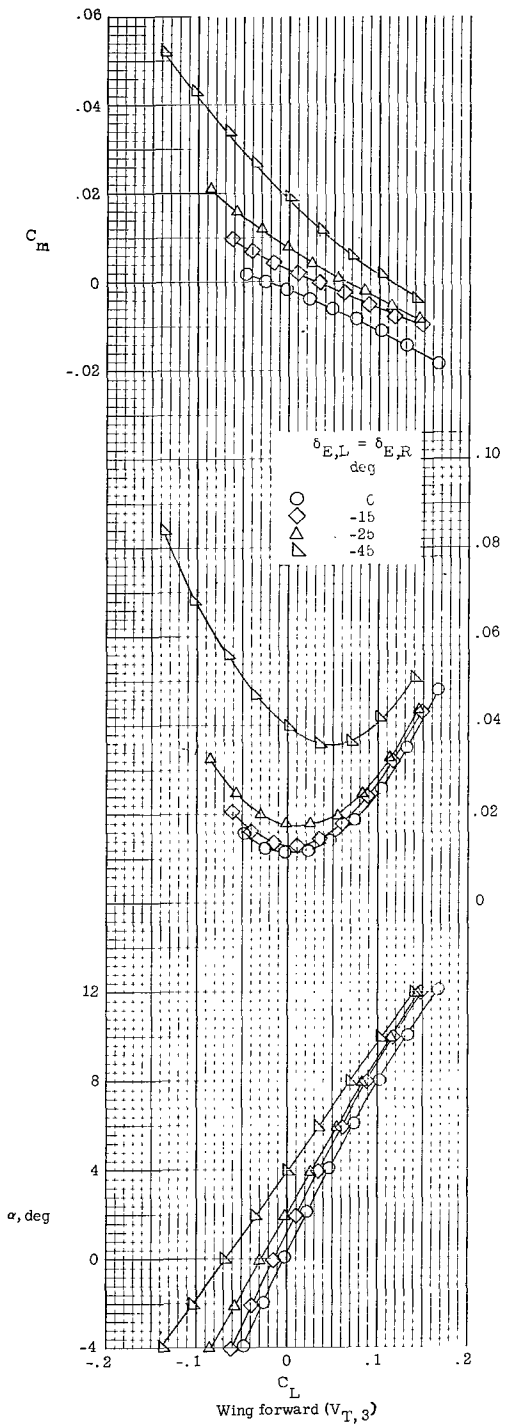
(b) Side fairing, wing, upper vertical tail, lower vertical tail, and tip fins.

Figure 25.- Concluded.



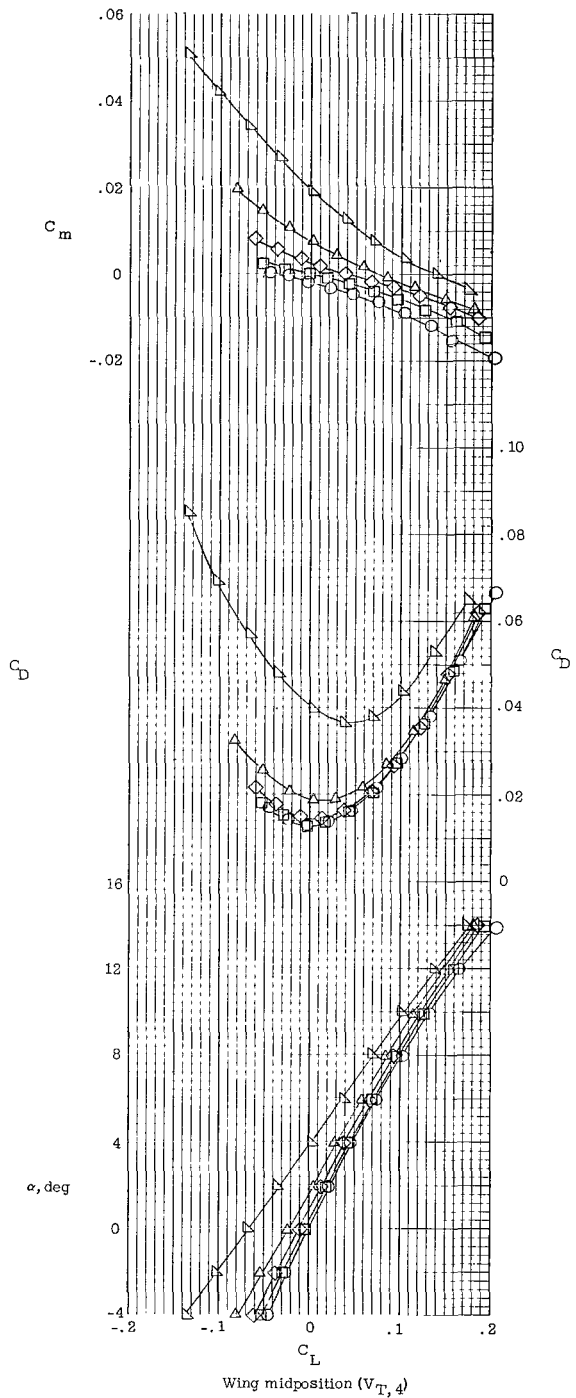
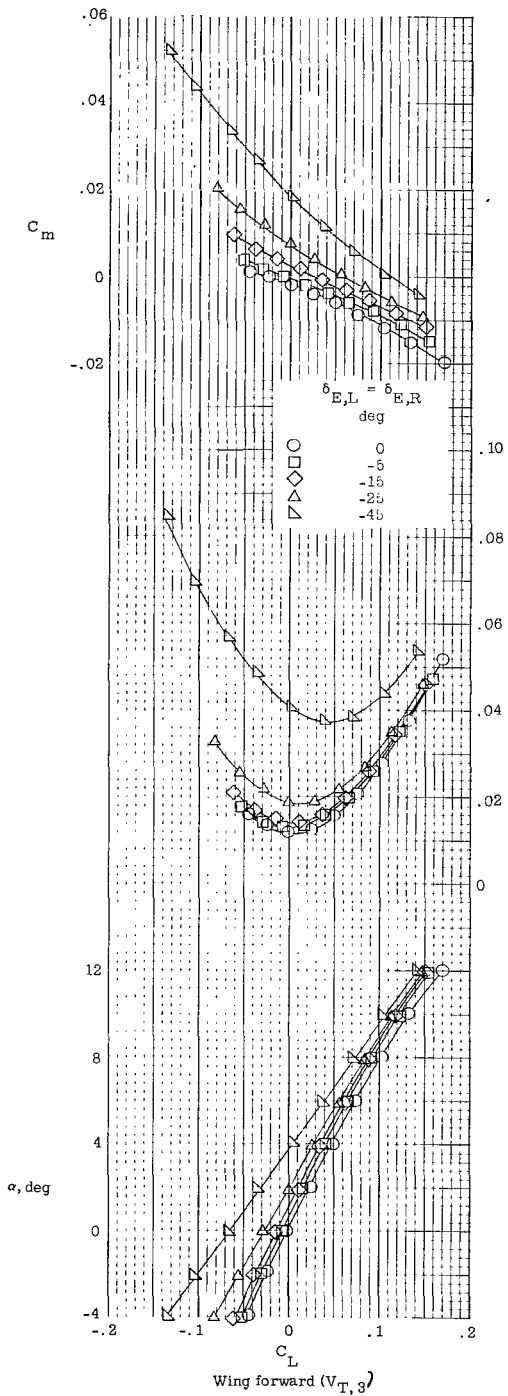
(a) $BX_2W_2E_2V_UV_{L,2}$.

Figure 26.- Effect of elevon deflection on longitudinal stability characteristics of model 1. $M_\infty = 6$; $\delta_{V_U} = \delta_{V_{L,2}} = 0^\circ$.



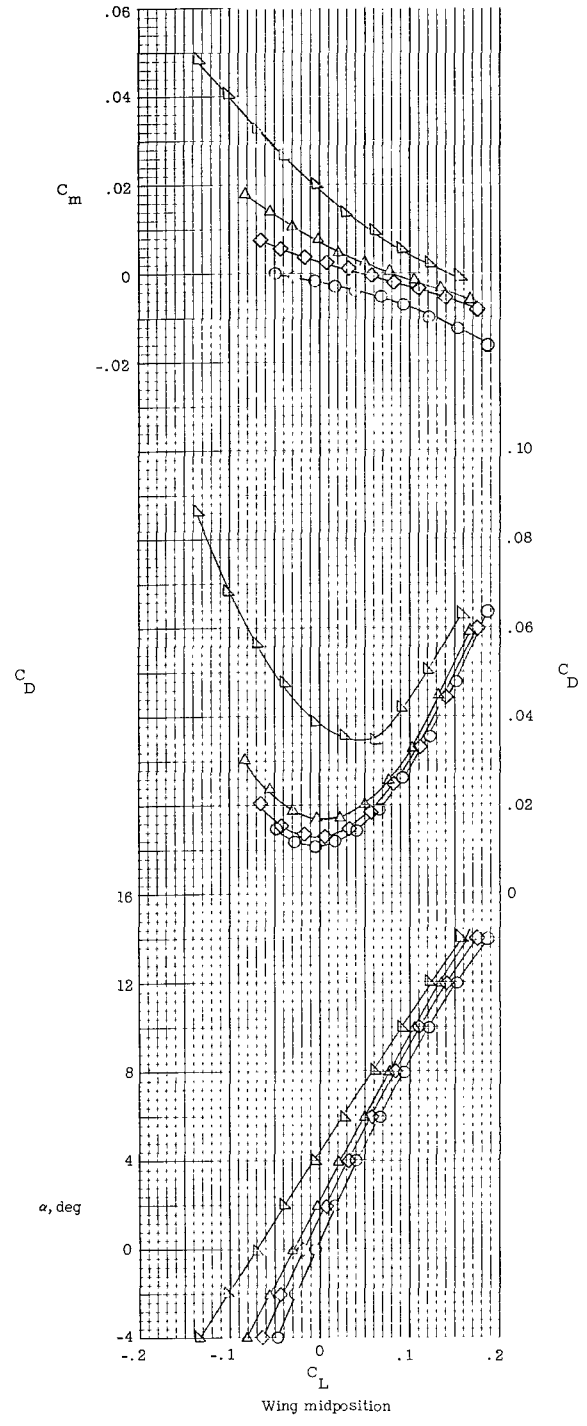
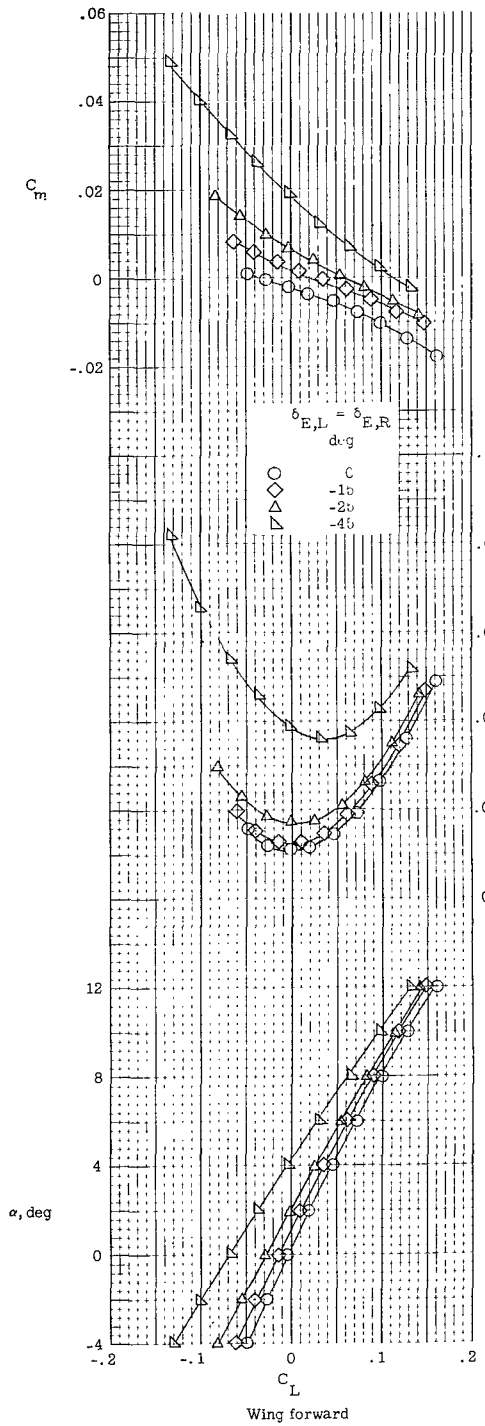
(b) $BX_2W_2E_2V_UV_LV_T$.

Figure 26.- Continued.

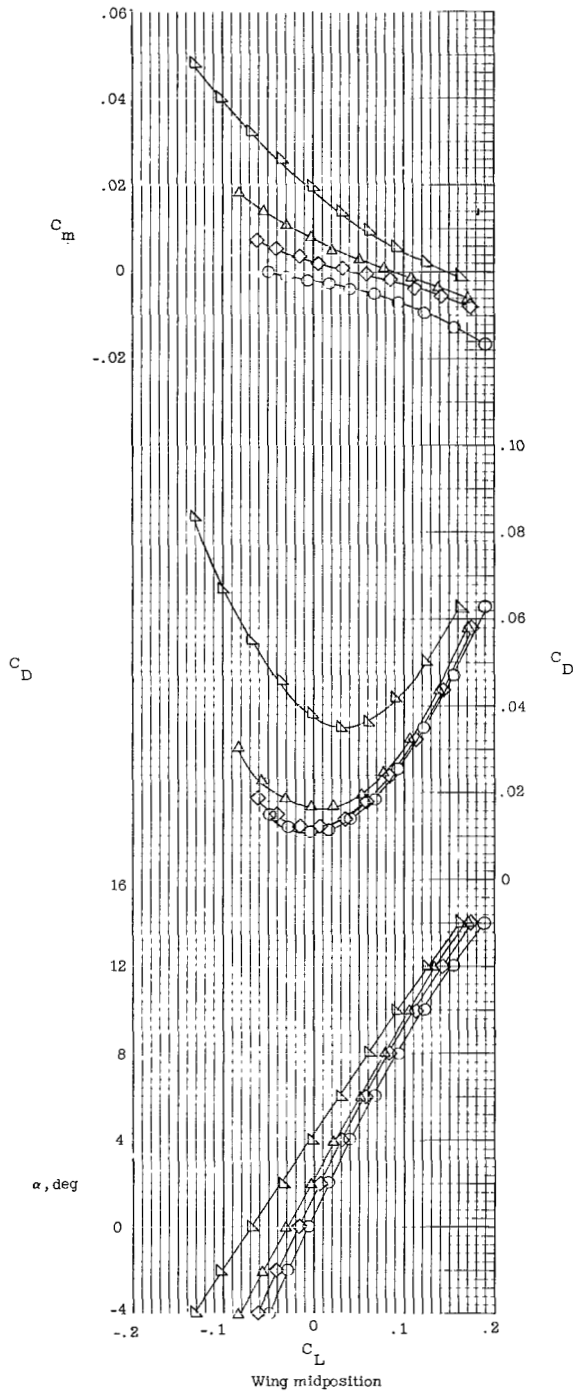
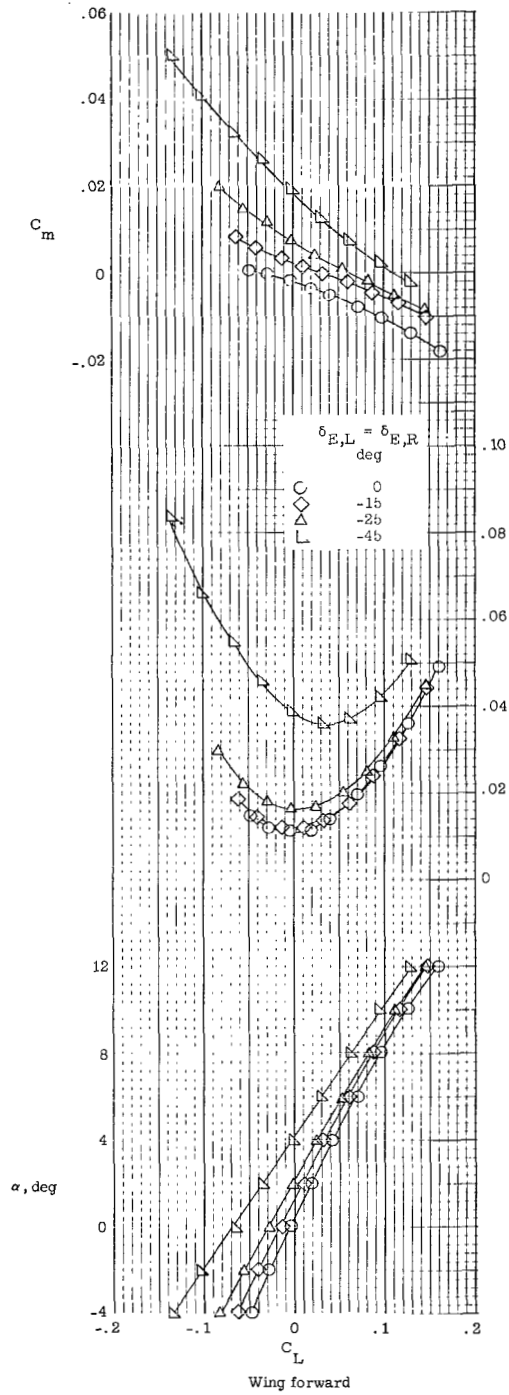


(c) $BX_2W_2E_2V_UV_{L,2}V_T$.

Figure 26.- Continued.

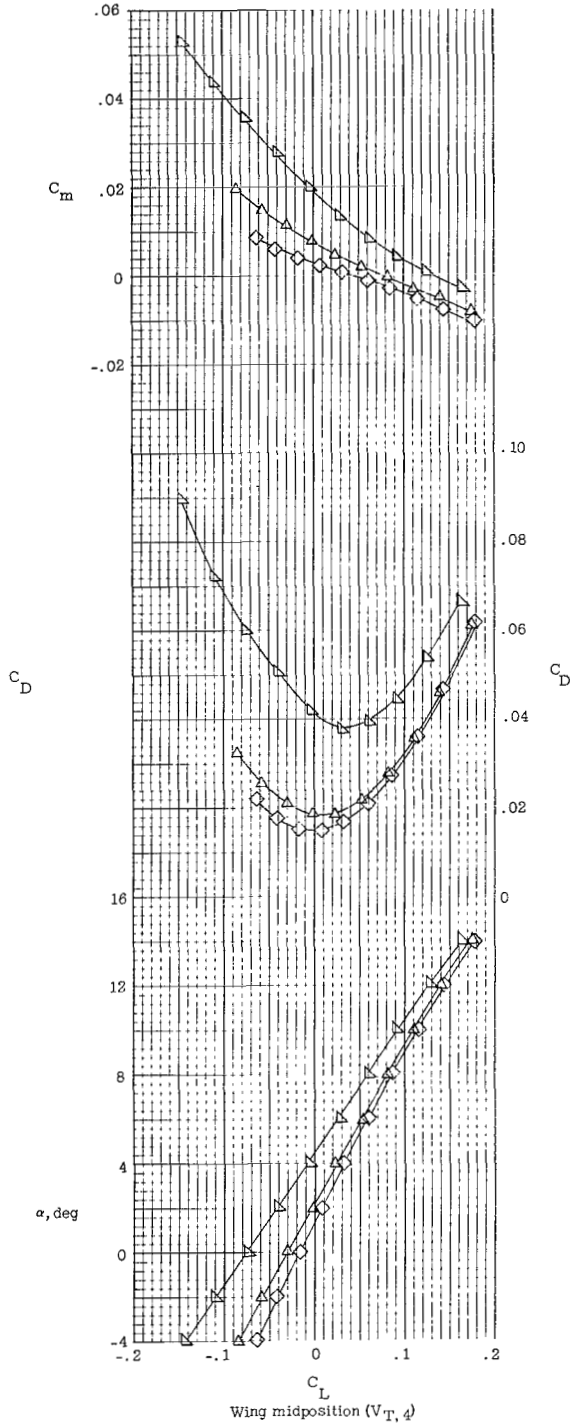
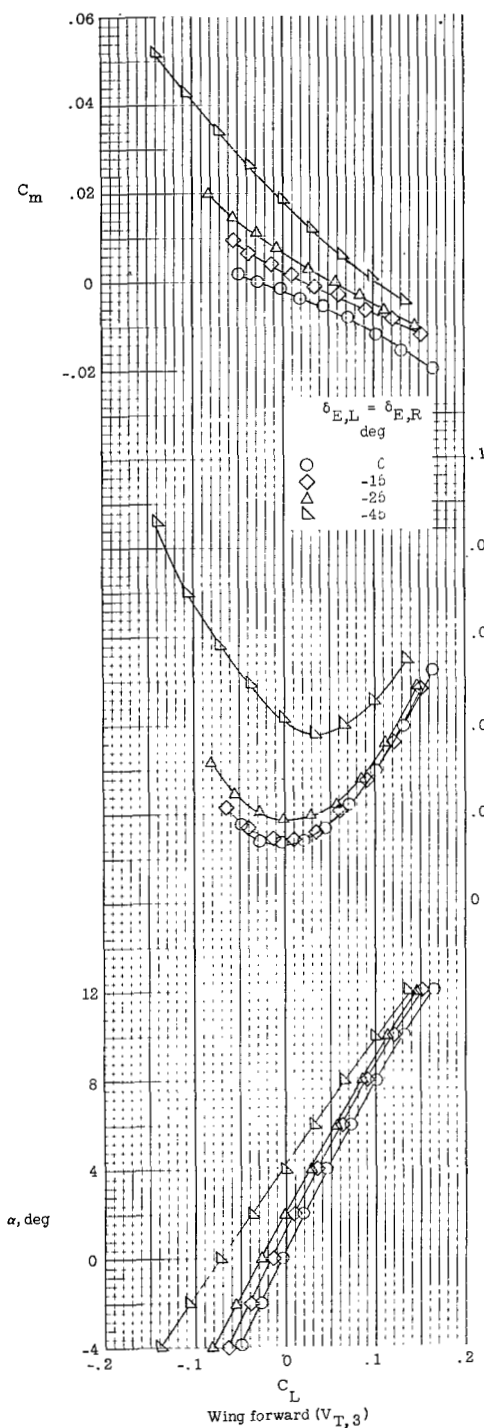


(d) BX₂W₂E₂V_UV_R,C
 Figure 26.- Continued.

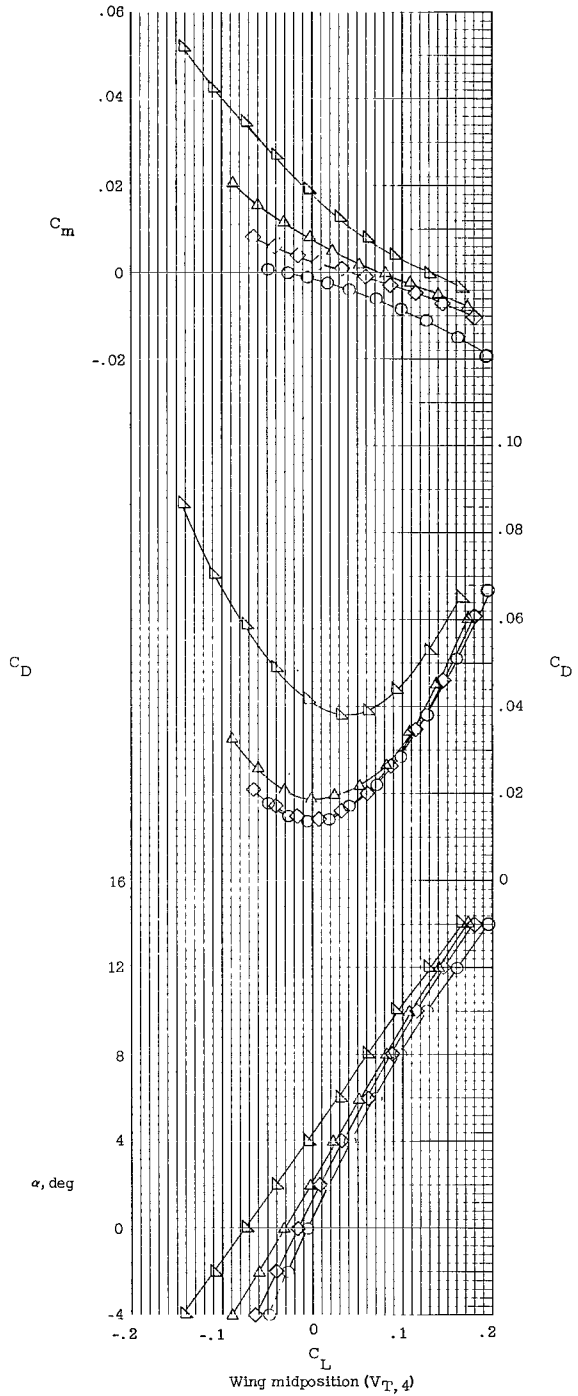
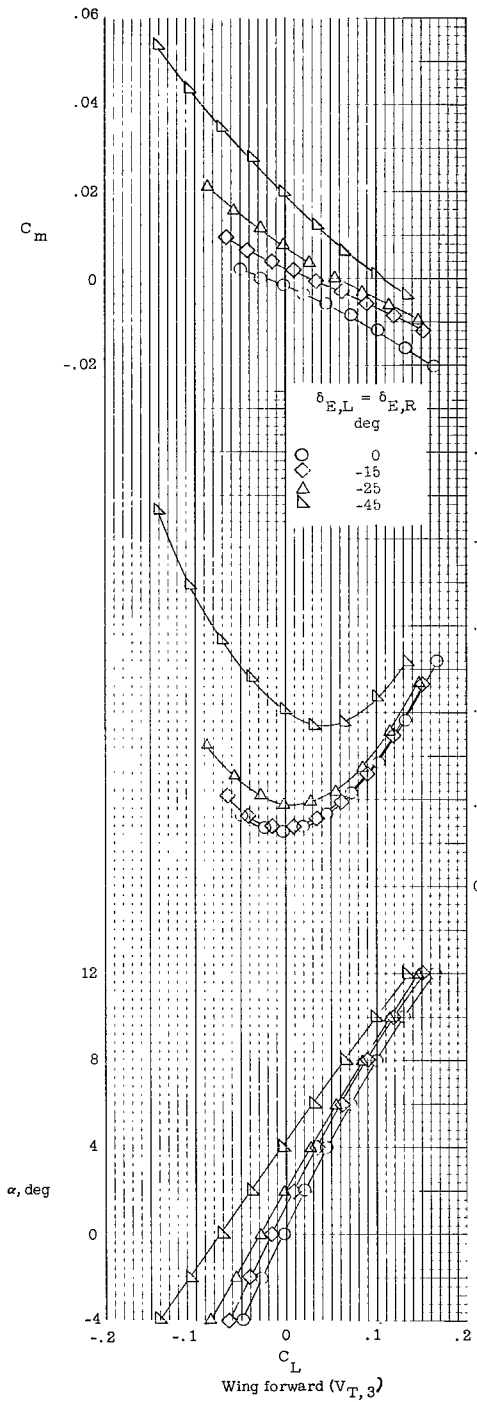


(e) $BX_2W_2E_2V_UV_R,0$

Figure 26.- Continued.

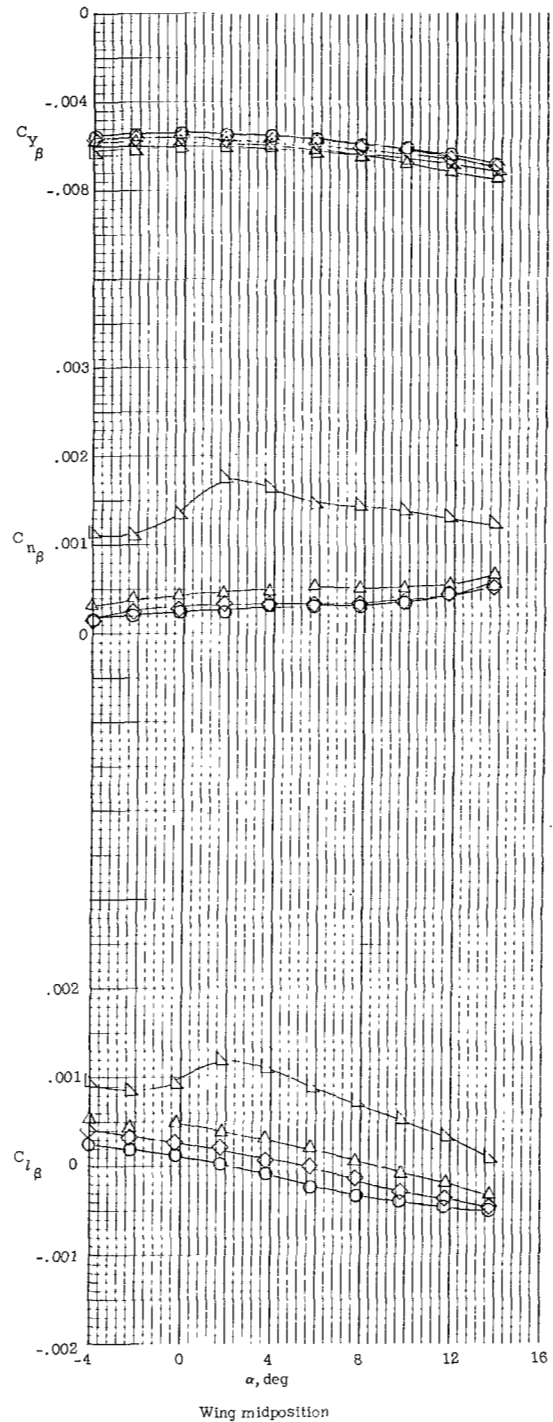
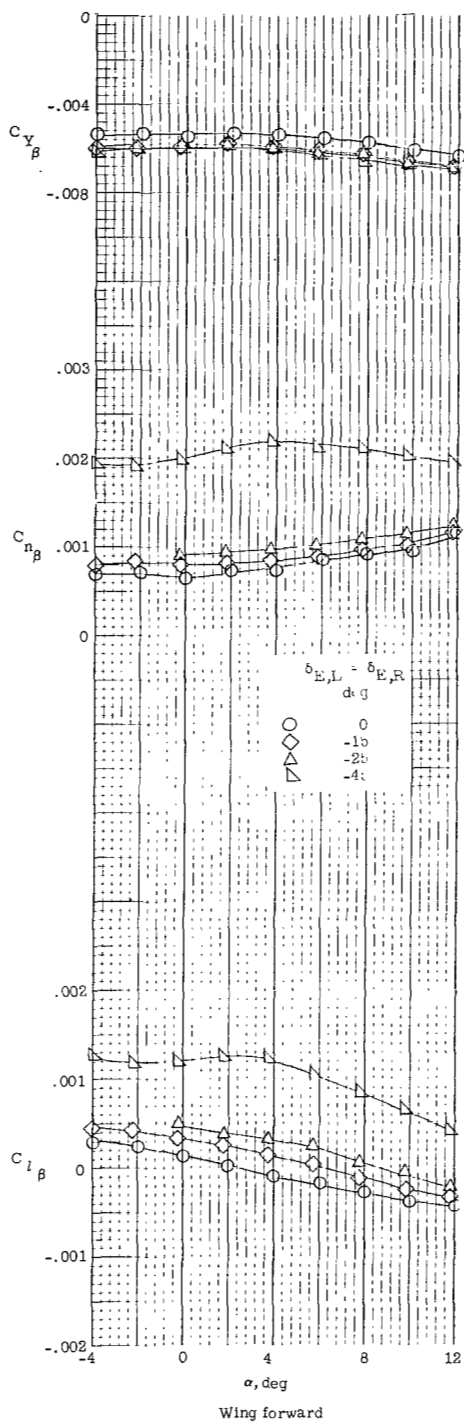


(f) $BX_2W_2E_2V_UV_R,CV_T$
 Figure 26.- Continued.



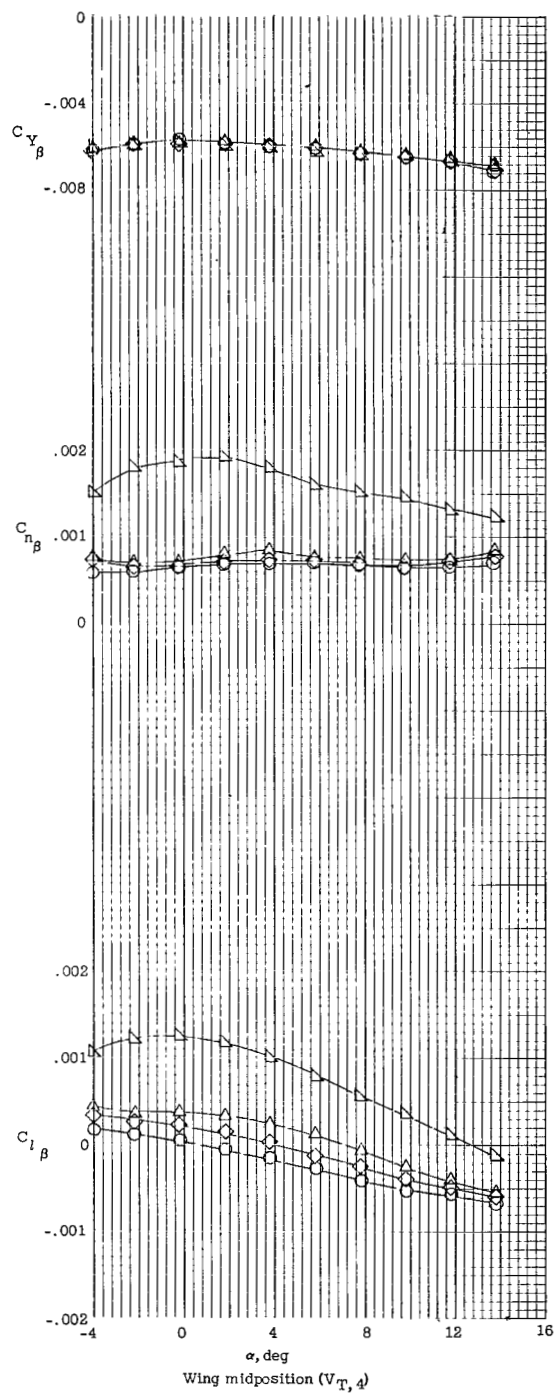
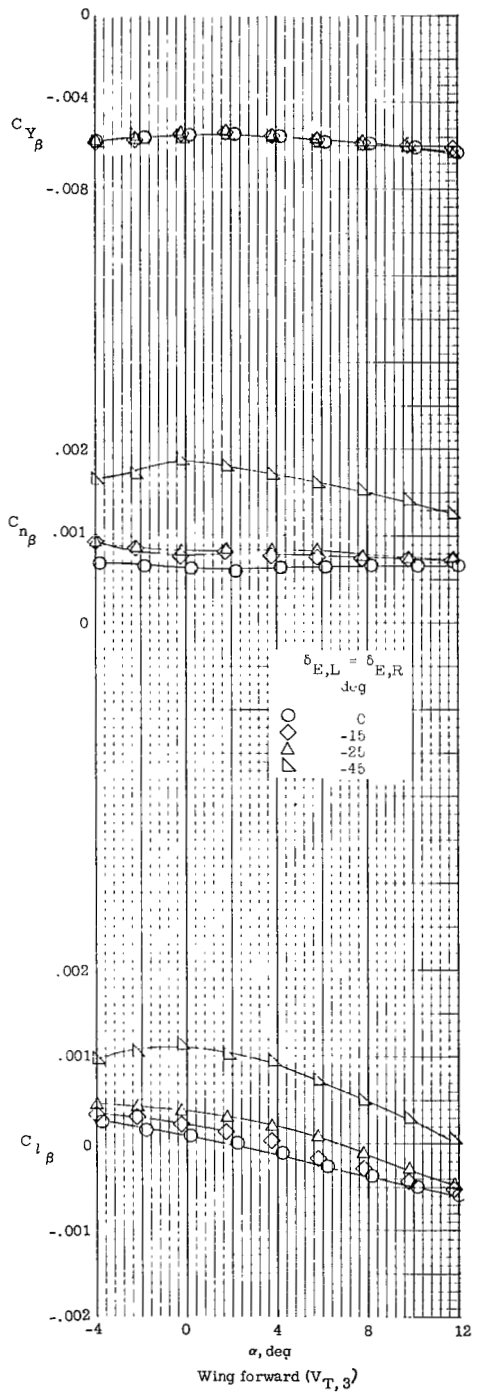
(g) $BX_2W_2E_2V_UV_R,0V_T$.

Figure 26.- Concluded.



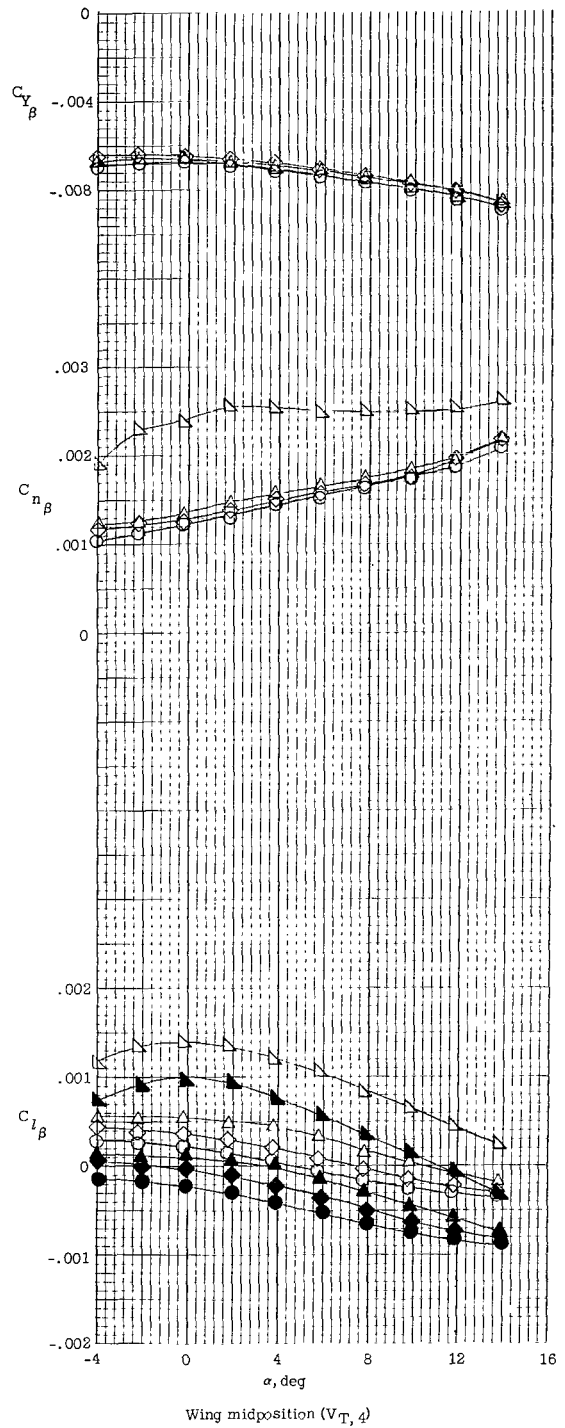
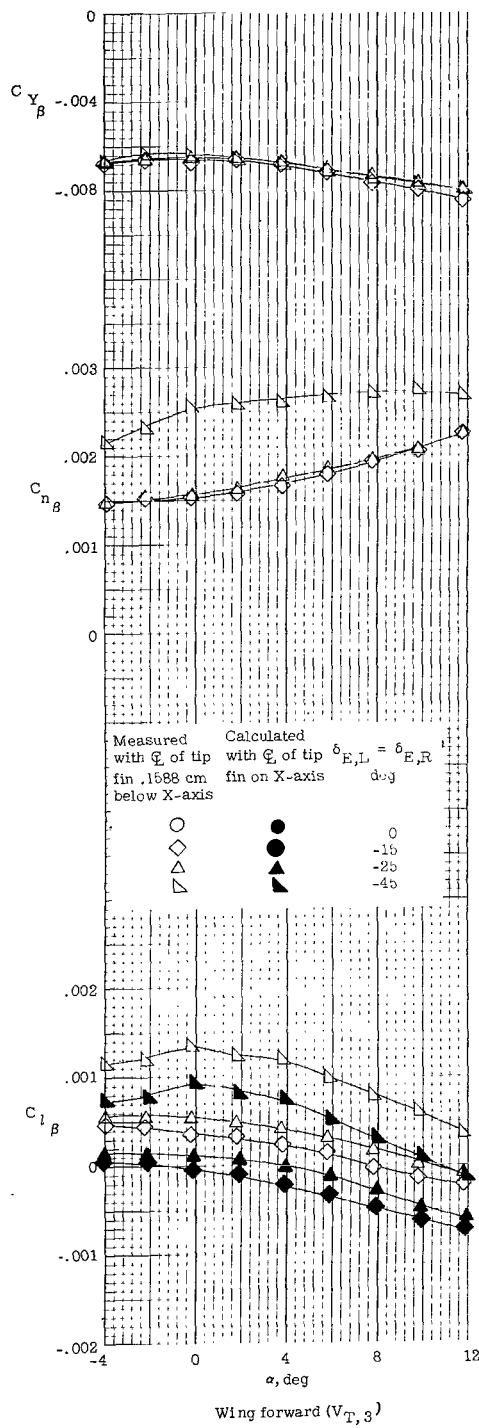
(a) $BX_2W_2E_2V_1V_{L,2}$.

Figure 27.- Effect of elevon deflection on lateral and directional stability characteristics of model 1. $M_\infty = 6$; $\delta_{VU} = \delta_{V_{L,2}} = 0^\circ$.

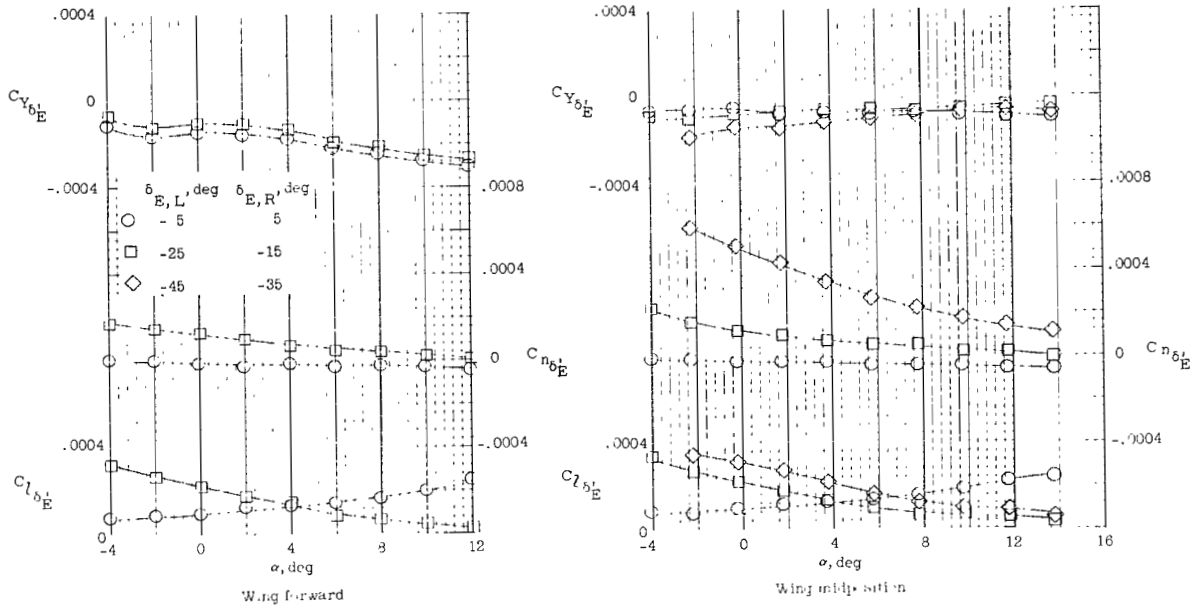


(b) $BX_2W_2E_2V_UV_LV_T$.

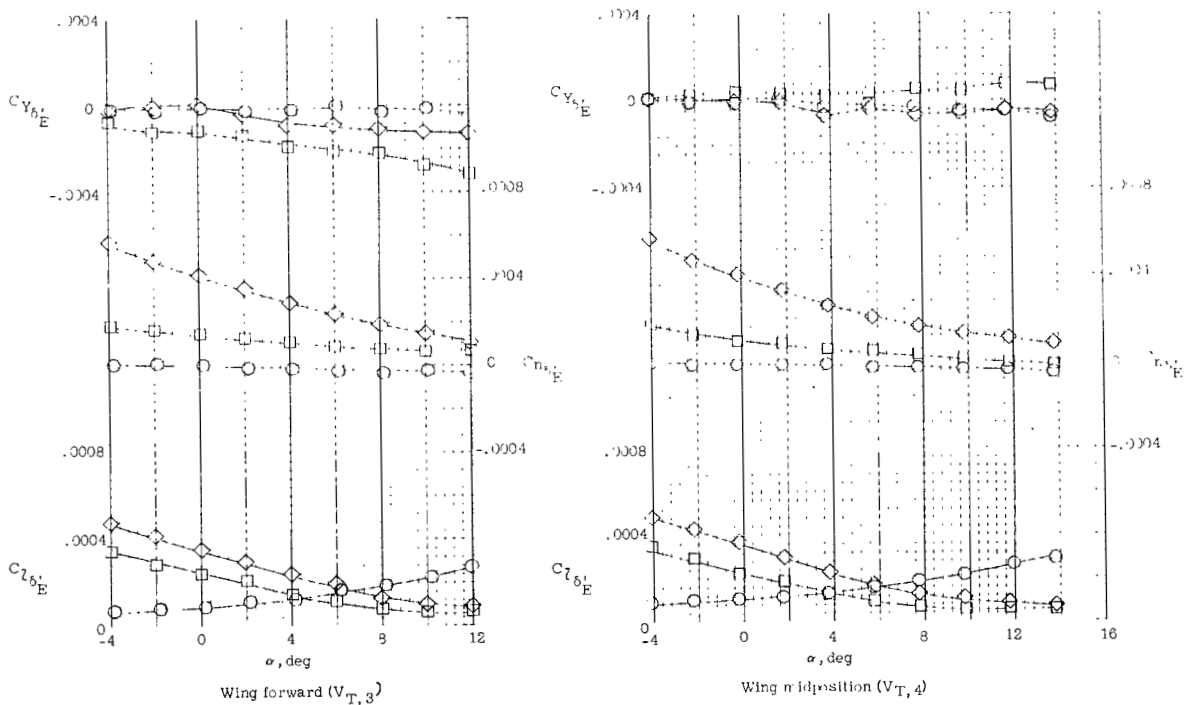
Figure 27.- Continued.



(c) $BX_2W_2E_2V_UV_L2V_T$.
Figure 27.- Concluded.



(a) $BX_2W_2E_2V_UV_{L,2}$.



(b) $BX_2W_2E_2V_UV_{L,2}V_T$.

Figure 28.- Effect of differential elevon deflection on lateral and directional control characteristics of model 1.
 $M_\infty = 6$; $\delta_{V_U} = \delta_{V_{L,2}} = 0^\circ$.

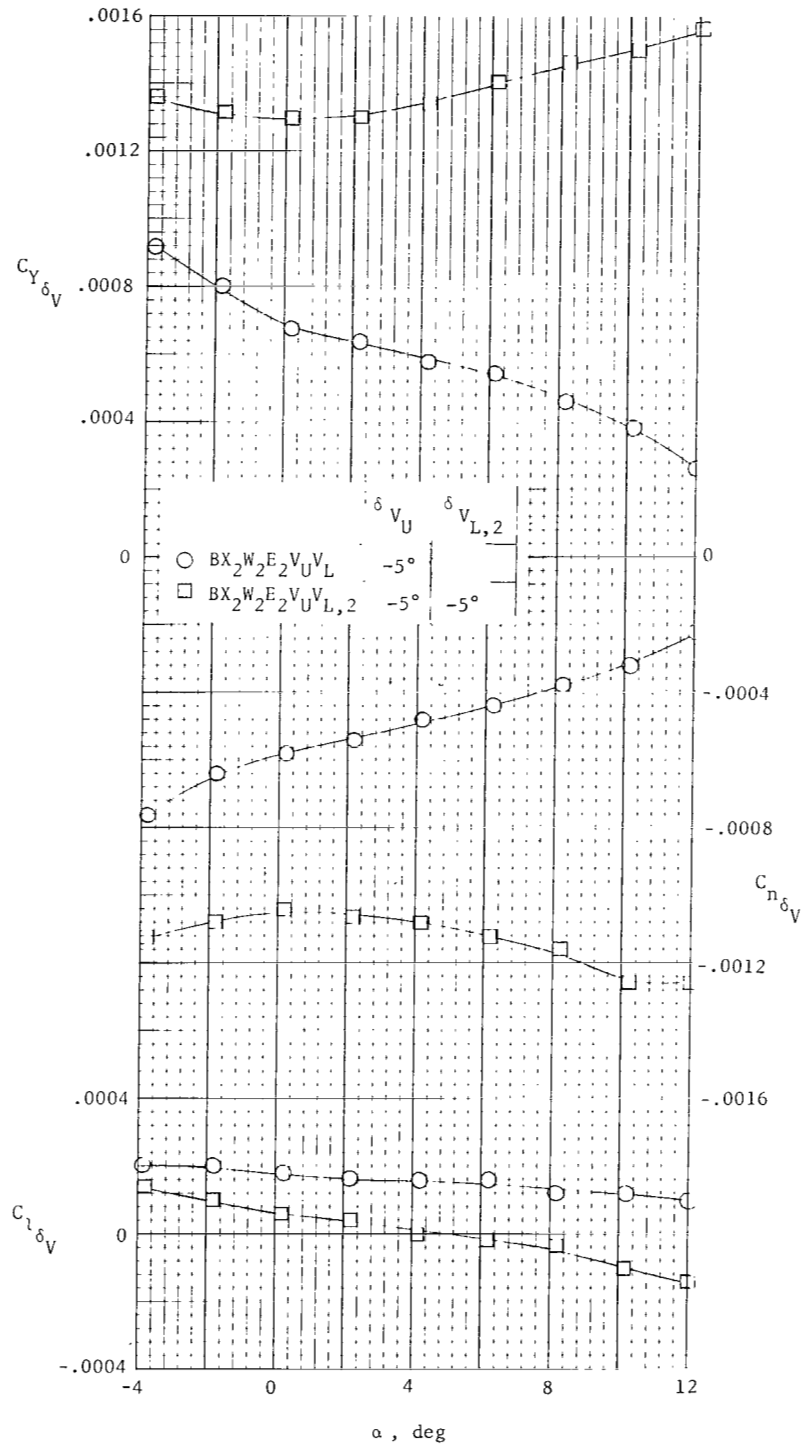
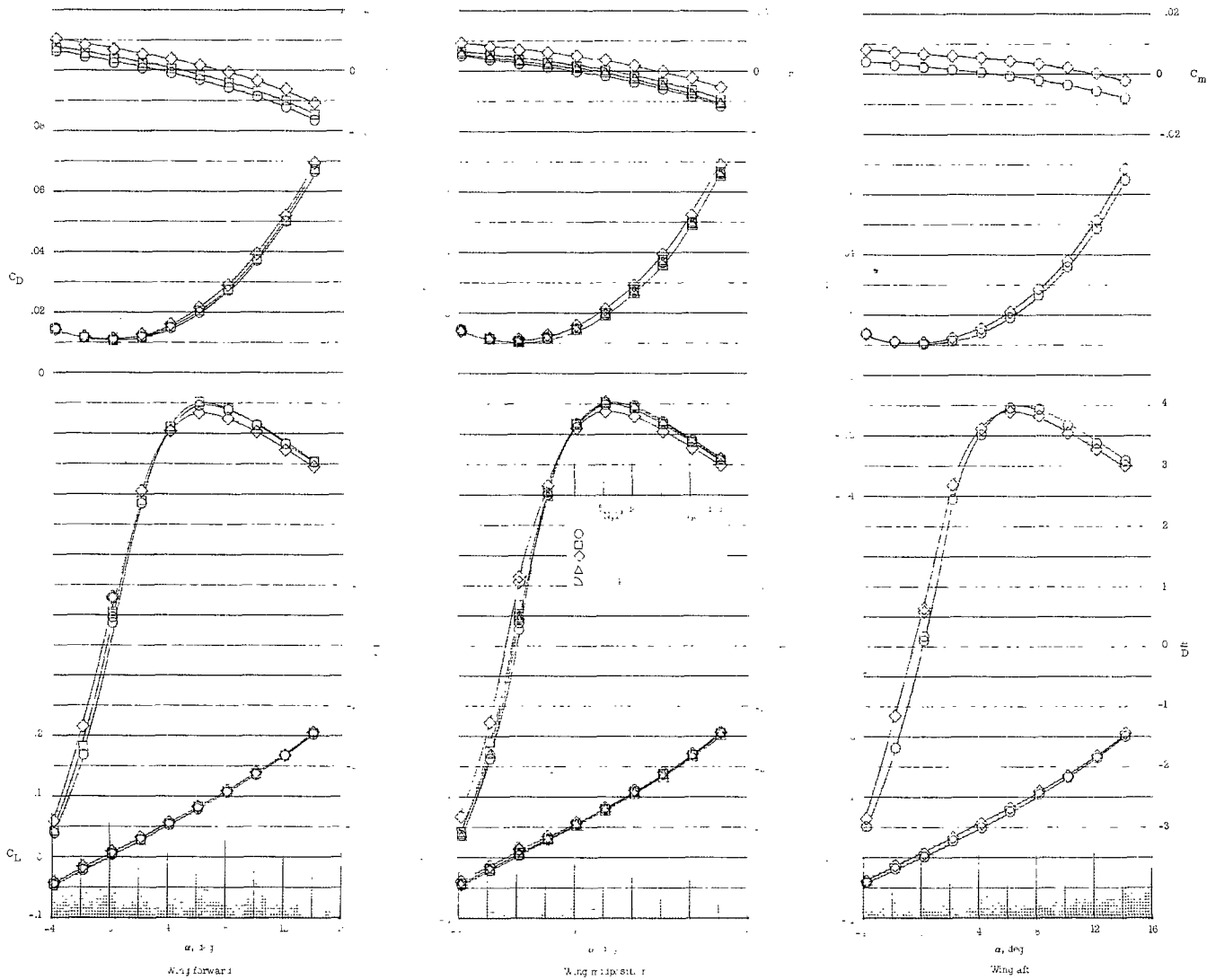
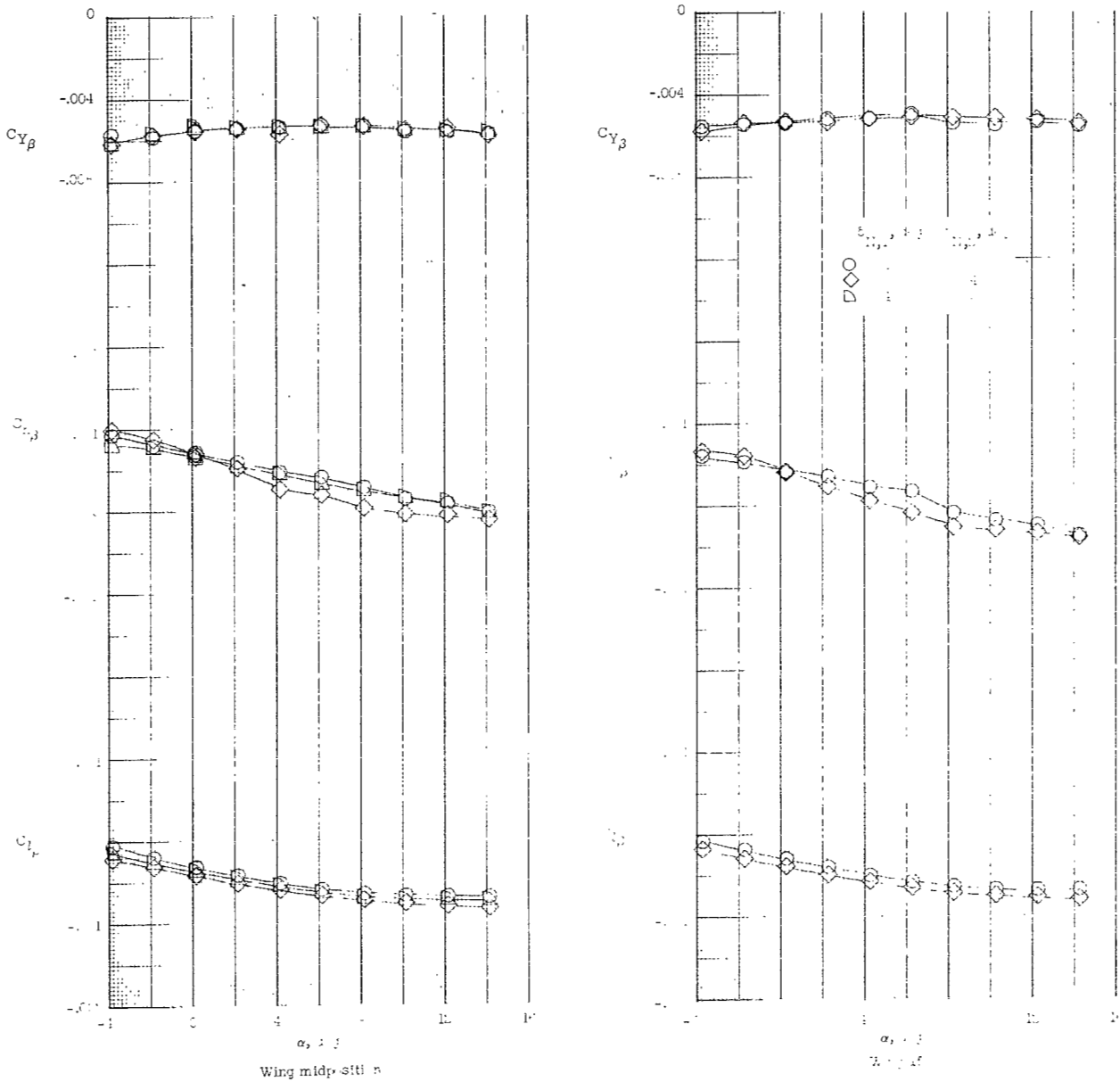


Figure 29.- Effect of vertical-tail deflection on directional control characteristics of model 1 with wing in forward position.
 $M_\infty = 6$; $\delta_{E,L} = \delta_{E,R} = 0^\circ$.



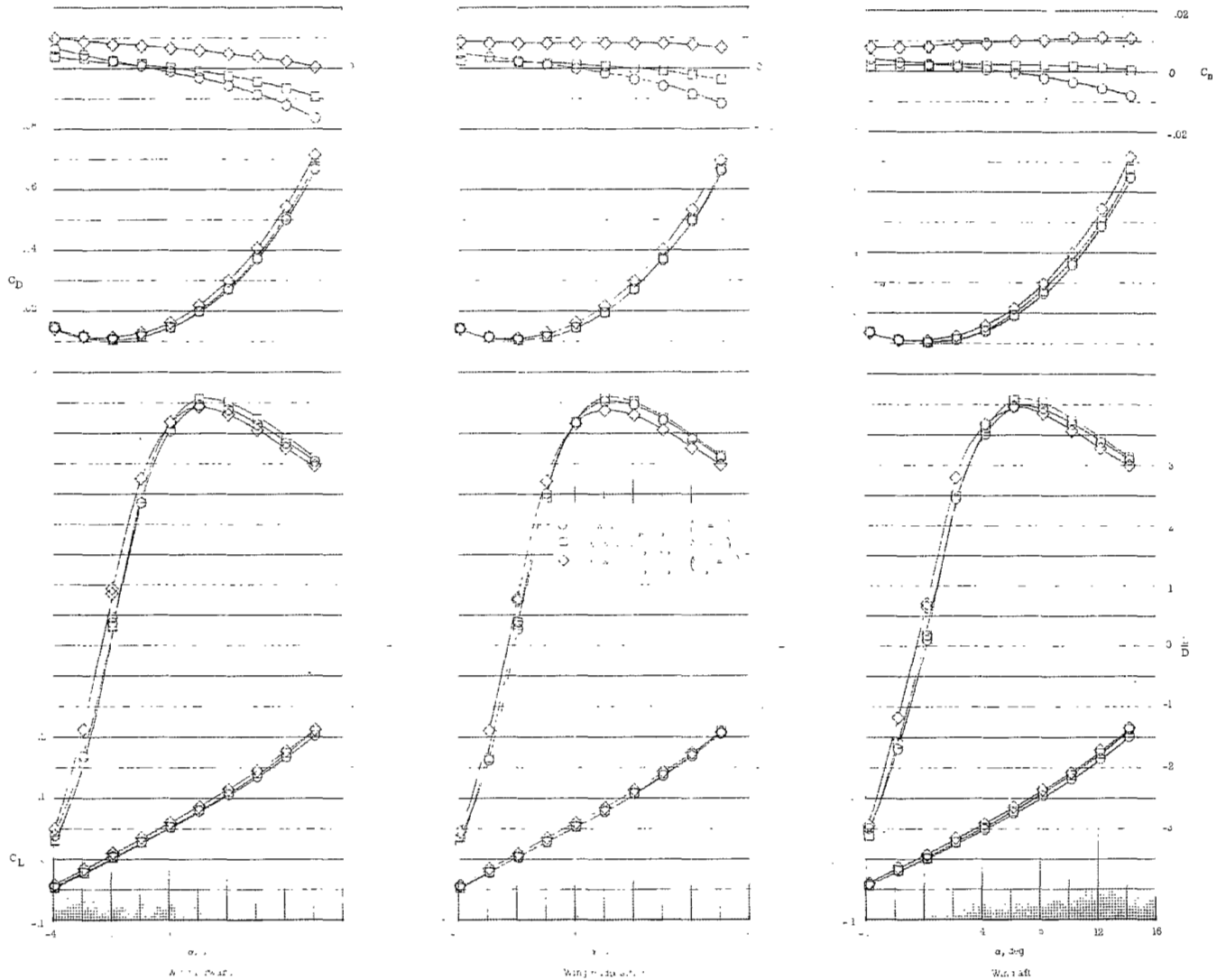
(a) Longitudinal characteristics.

Figure 30.- Effect of nose cant on aerodynamic characteristics of model 2 (BX₃W₃E₃V_{U,2}V_{L,6}). $M_\infty = 6$; $\delta_E = 0^\circ$.



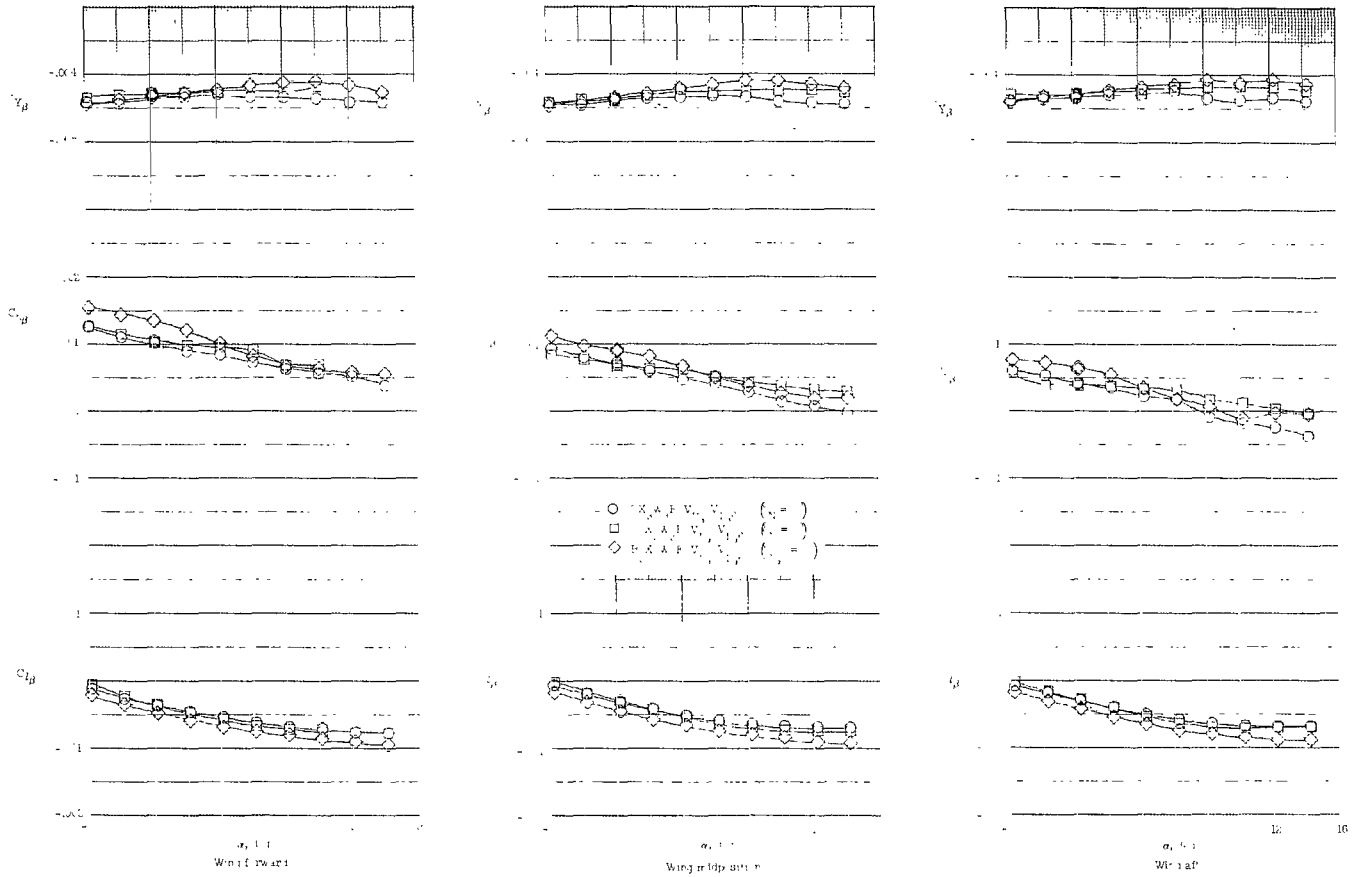
(b) Lateral and directional stability characteristics.

Figure 30.- Concluded.



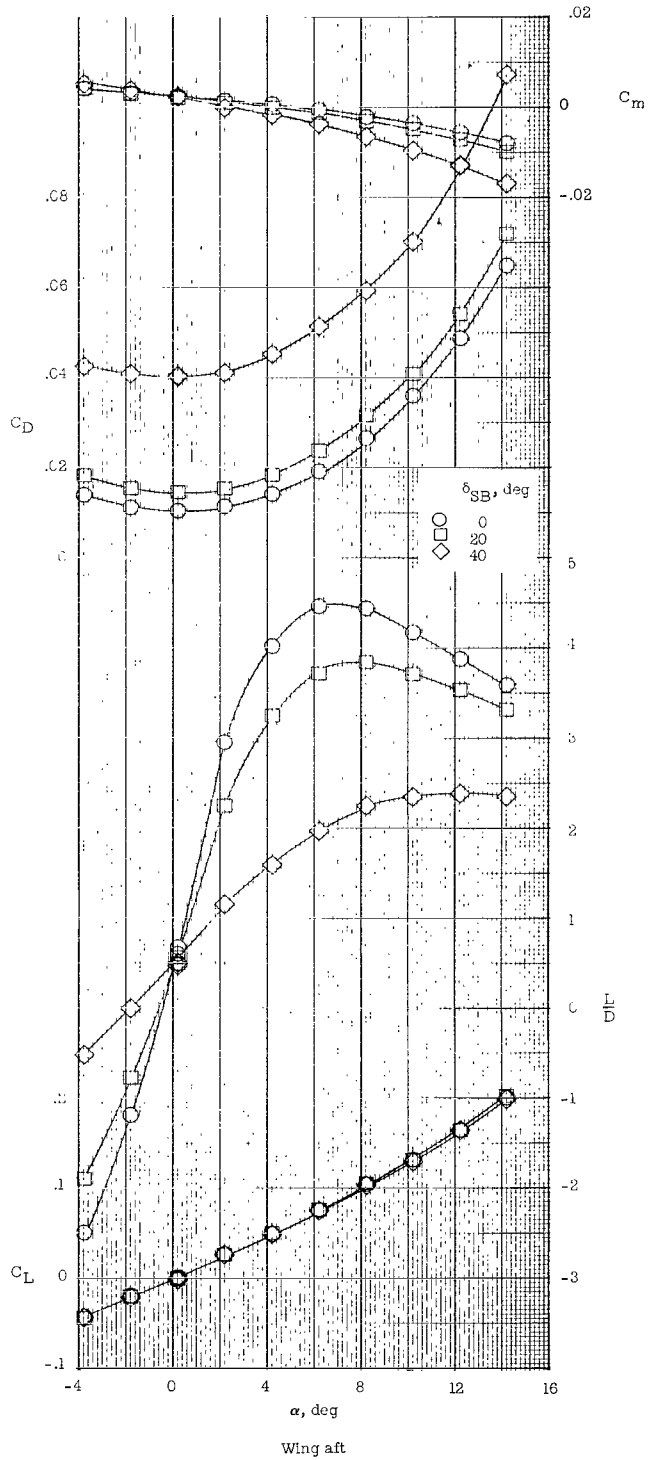
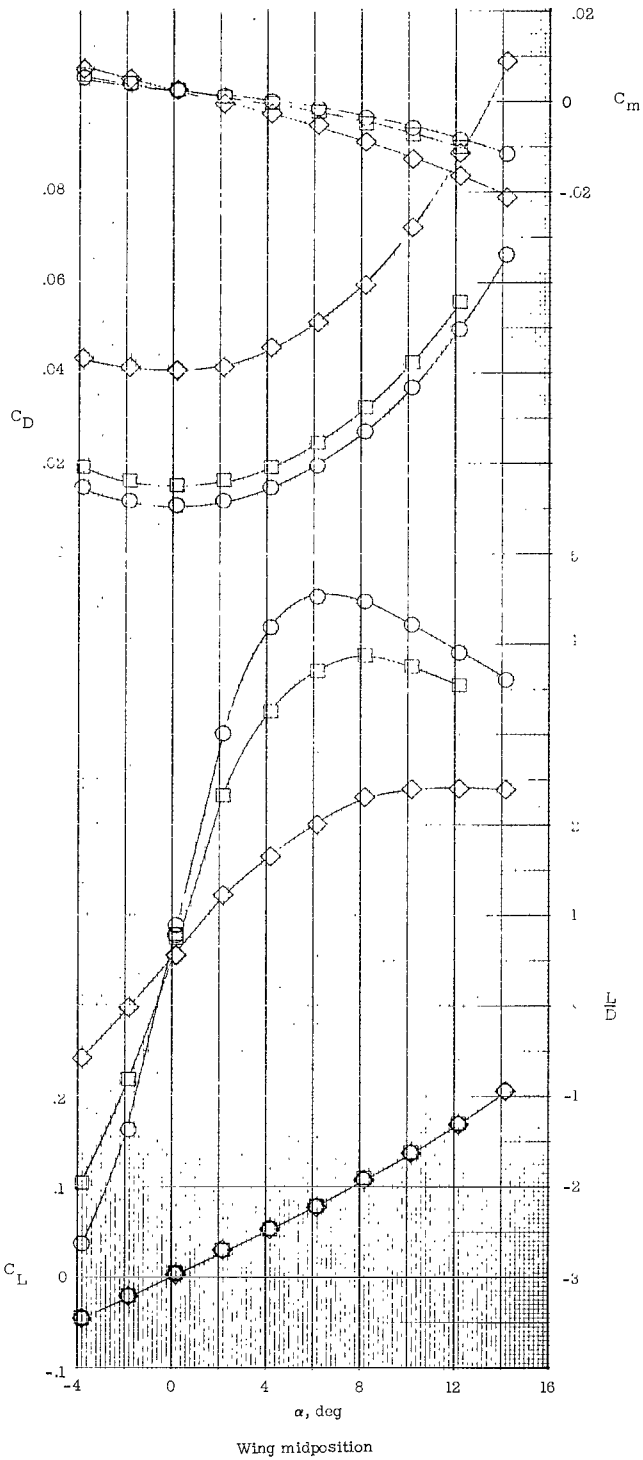
(a) Longitudinal characteristics.

Figure 31.- Effect of strakes on aerodynamic characteristics of model 2. $M_{\infty} = 6$; $\delta_E = 0^\circ$.



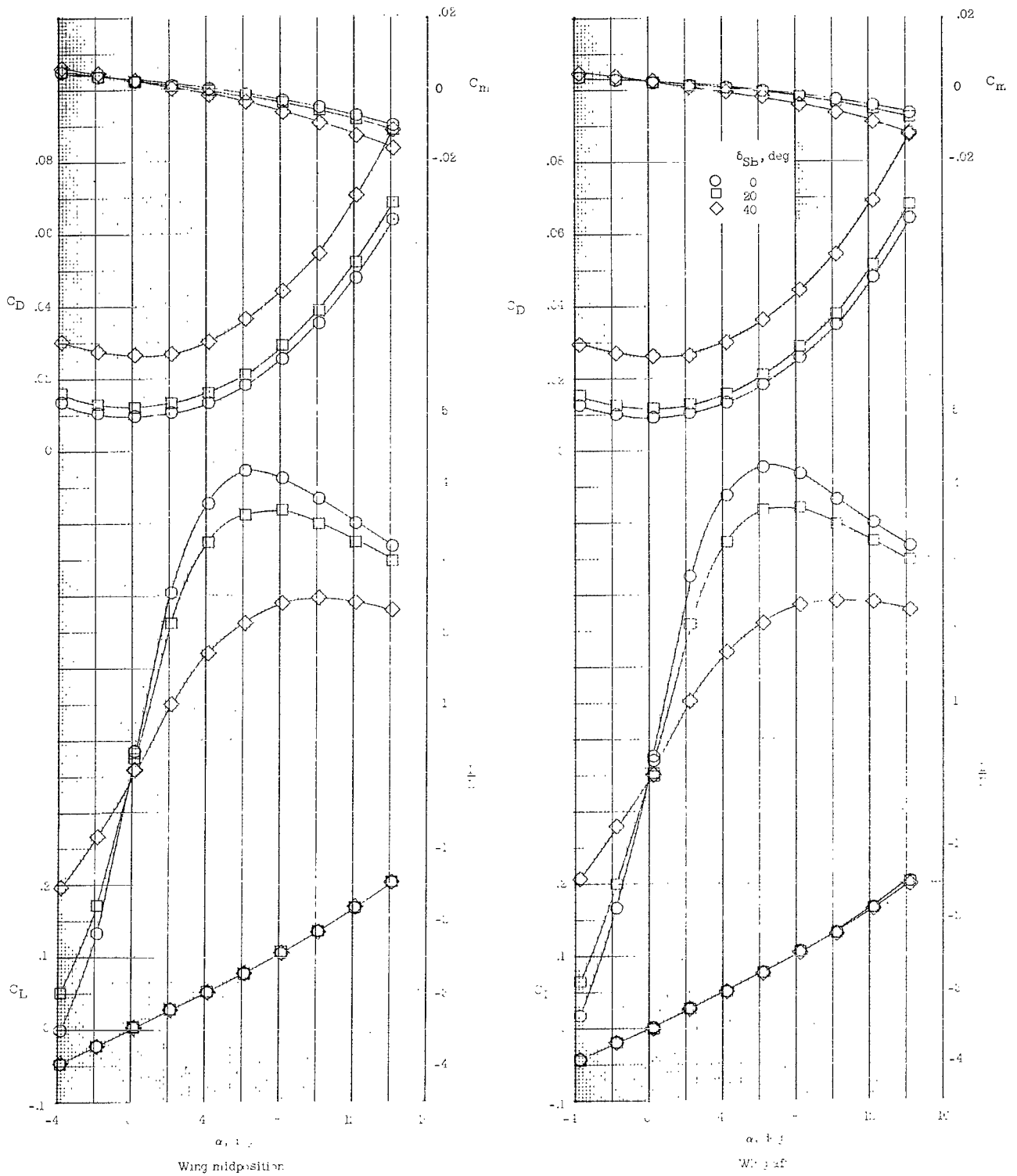
(b) Lateral and directional stability characteristics.

Figure 31.- Concluded.



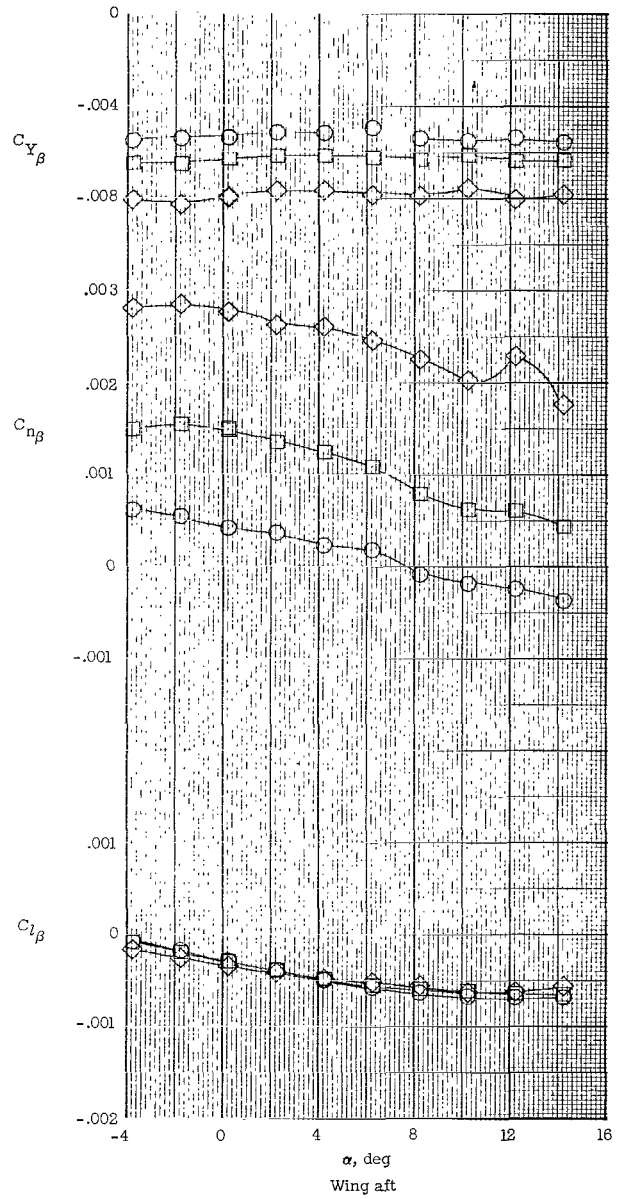
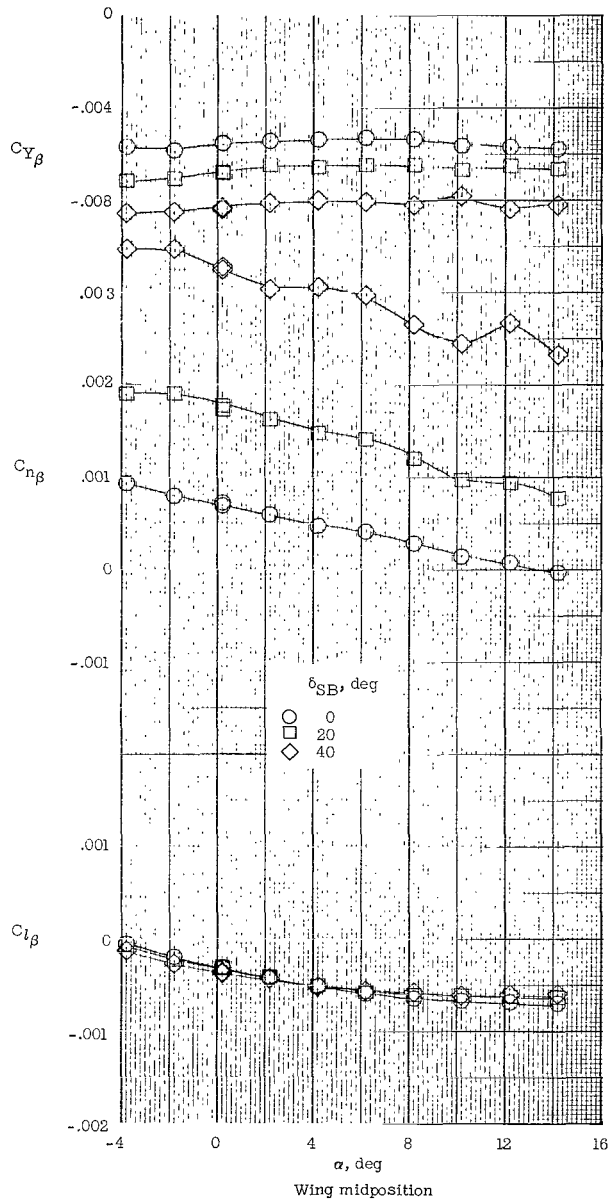
(a) Large vertical tails (BX3W3E3VU,2BV_L,6B).

Figure 32.- Effect of speed brakes on longitudinal aerodynamic characteristics of model 2. $M_\infty = 6$; $\delta_E = 0^\circ$.



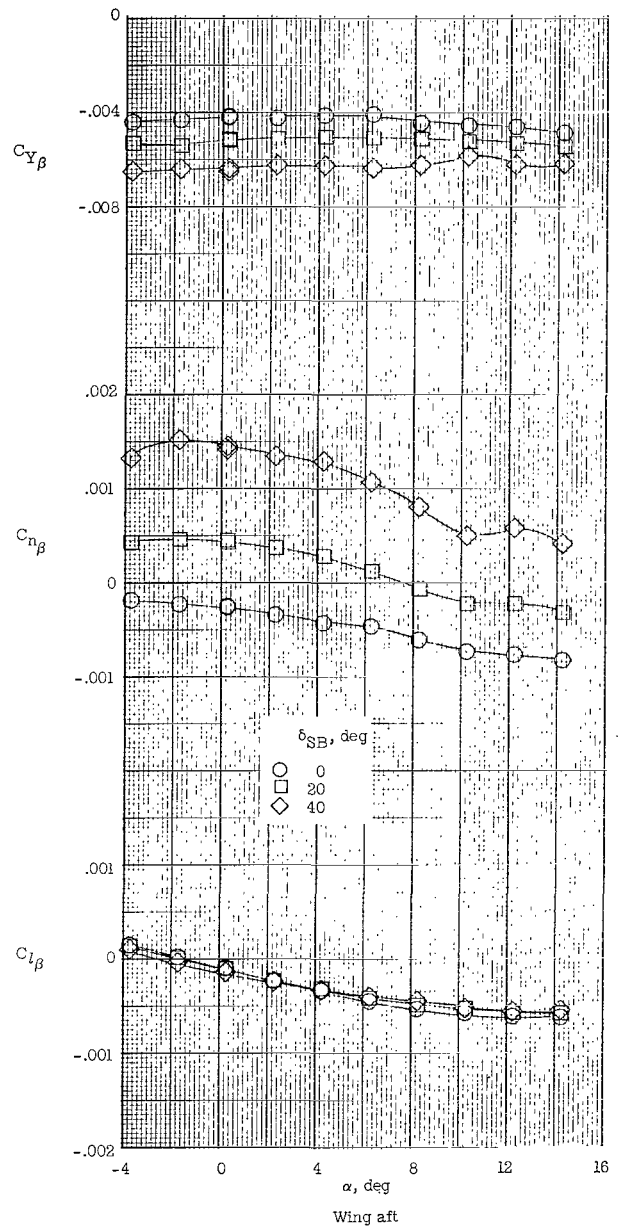
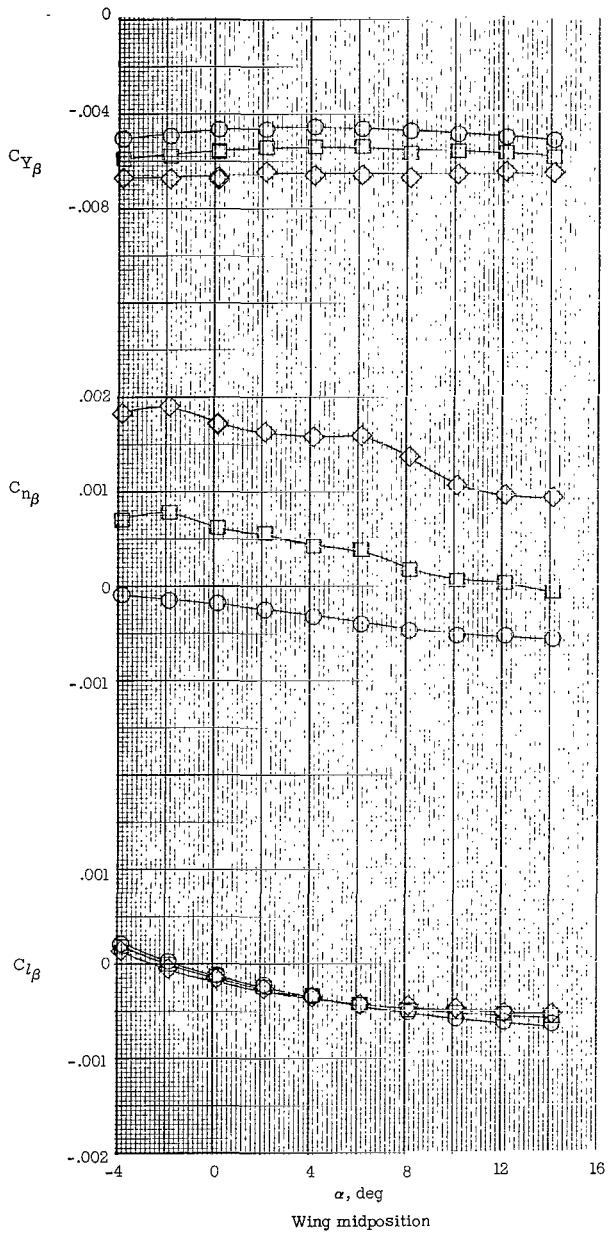
(b) Small vertical tails BX₃W₃E₃V_{U,B}V_{L,B}

Figure 32.- Concluded.



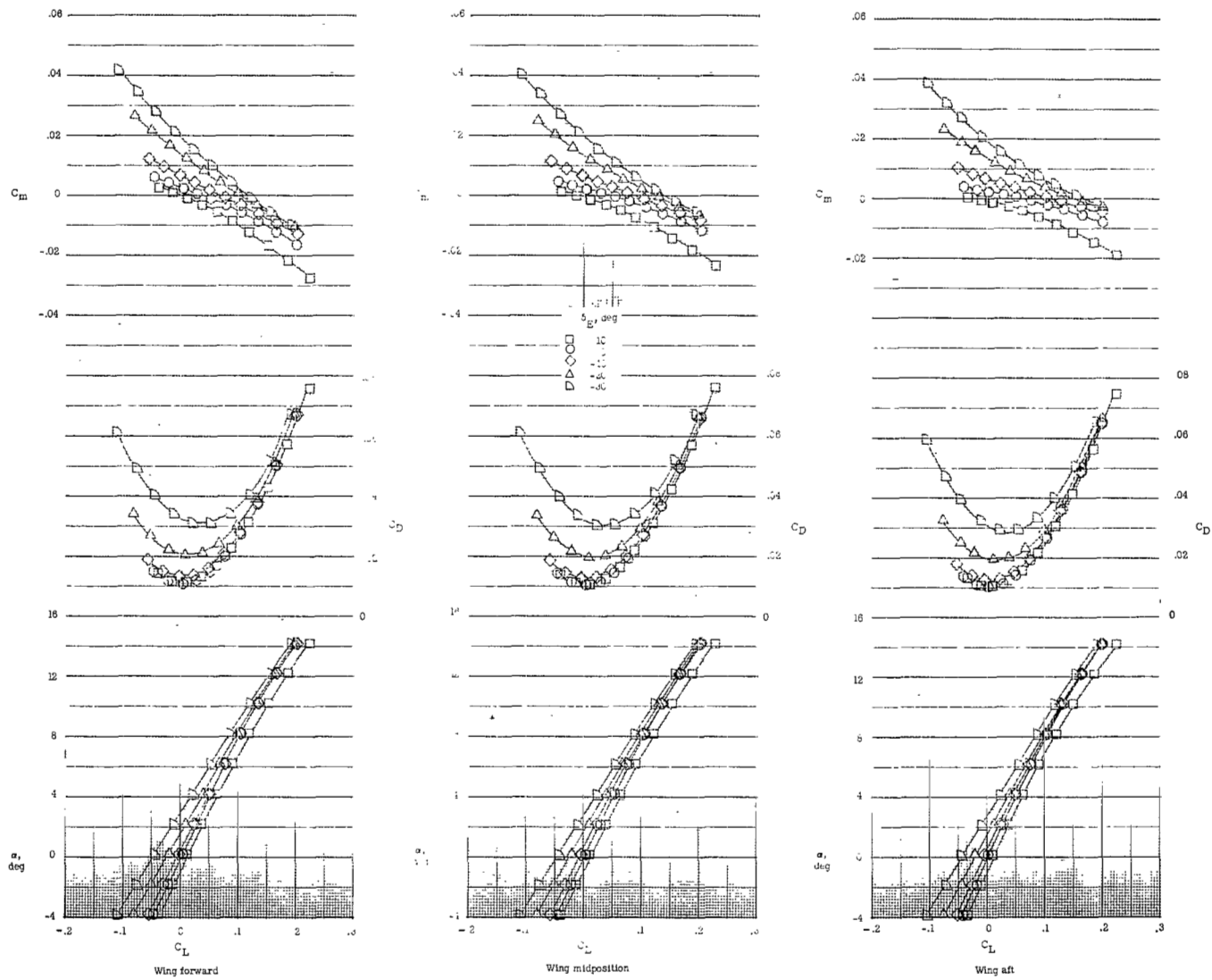
(a) Large vertical tails (BX3W3E3VU,2BV L,6B).

Figure 33.- Effect of speed brakes on lateral and directional stability characteristics of model 2. $M_{\infty} = 6$; $\delta_E = 0^\circ$.



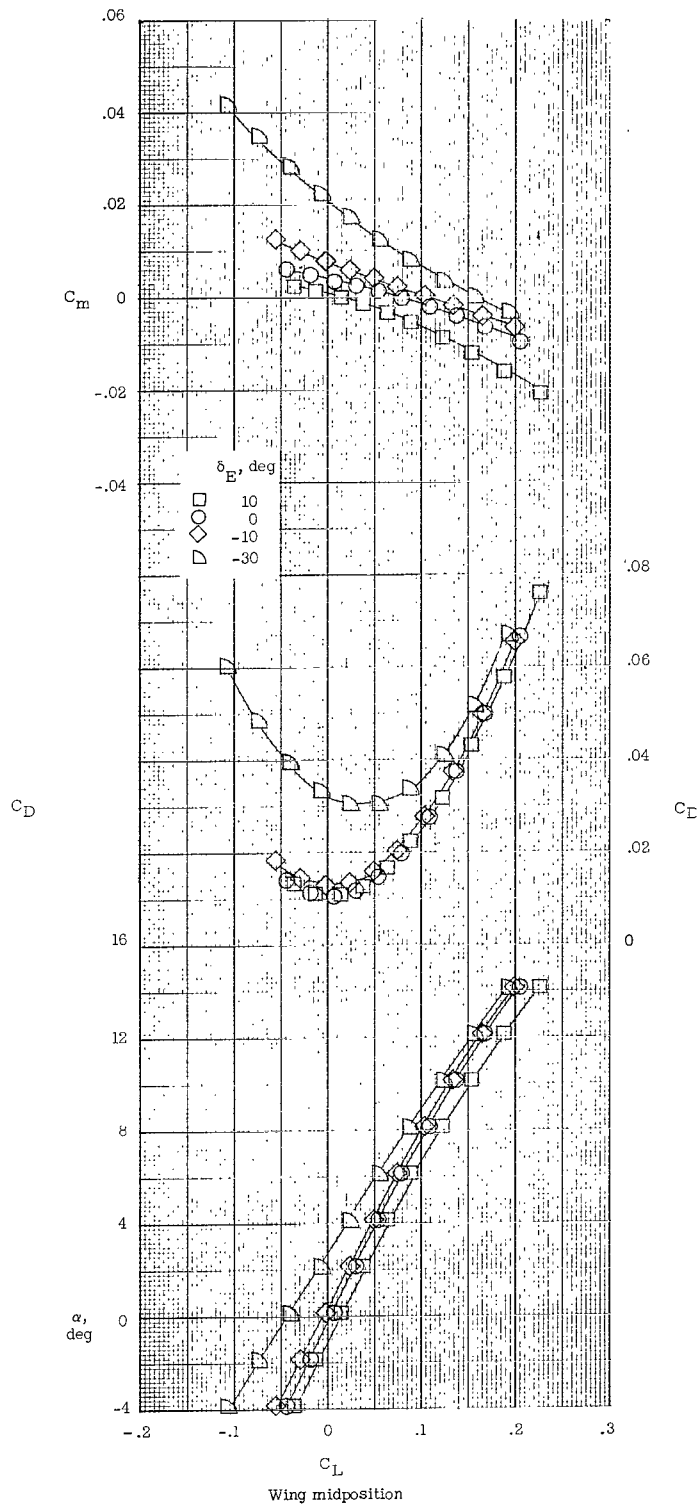
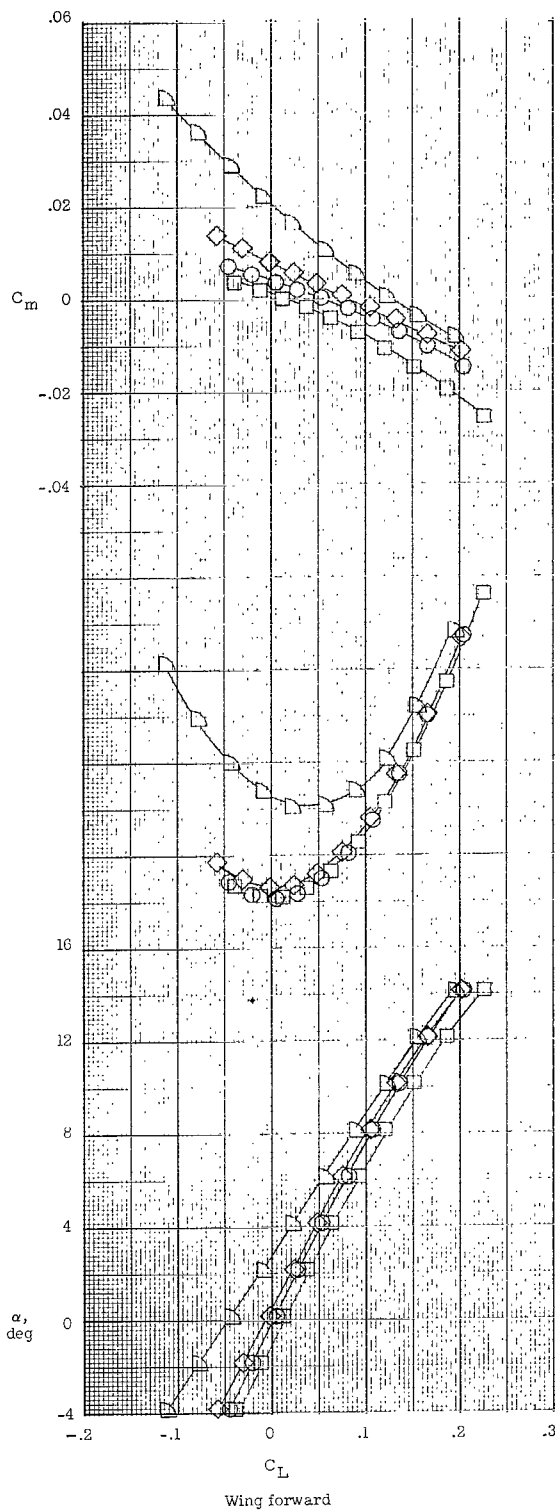
(b) Small vertical tails (BX₃W₃E₃V_{U,B}V_{L,B}).

Figure 33.- Concluded.



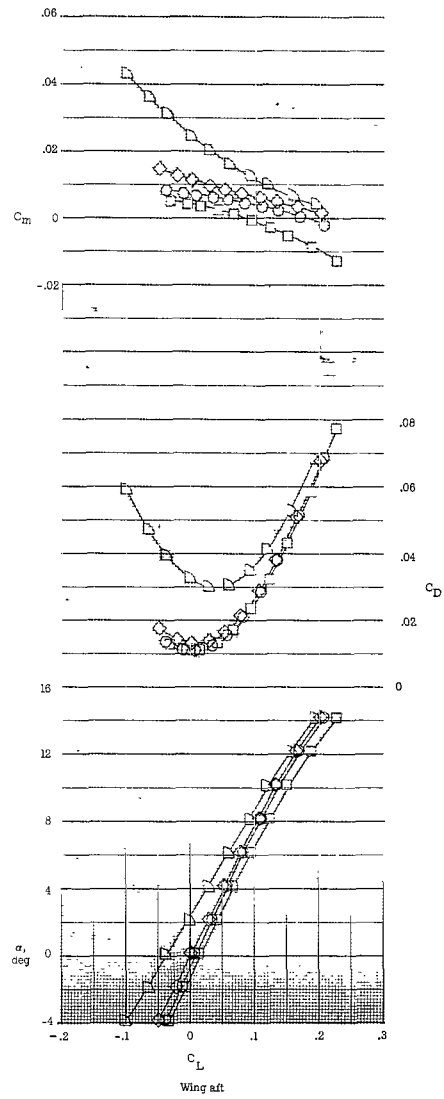
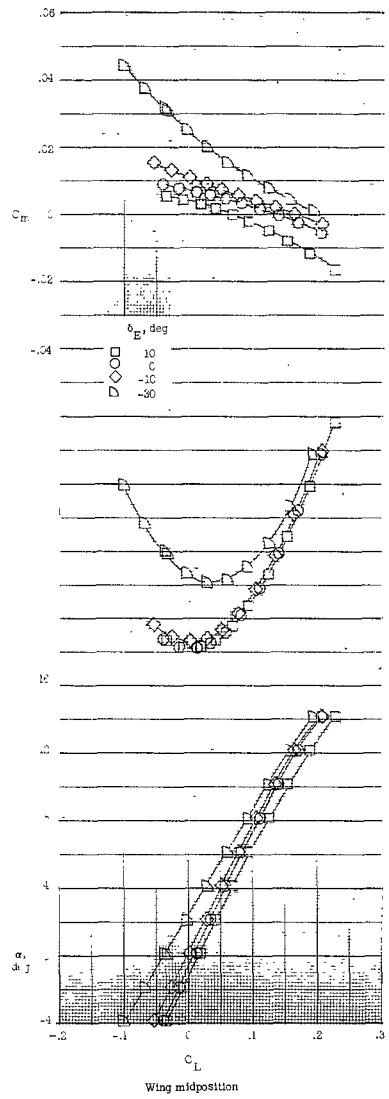
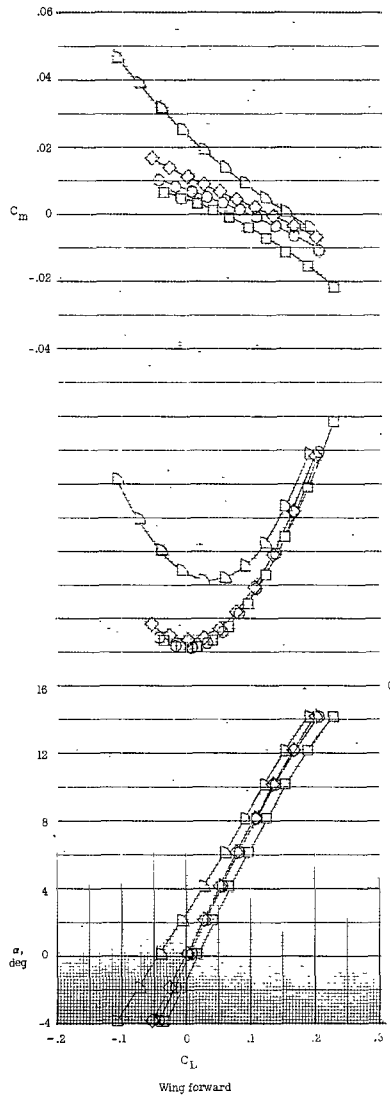
(a) $\delta_N = 0^\circ$.

Figure 34.- Effect of elevon deflection on longitudinal aerodynamic characteristics of model 2, basic configuration with nose cant (BX₃W₃E₃V_{U,2}V_{L,6}); $M_\infty = 6$.



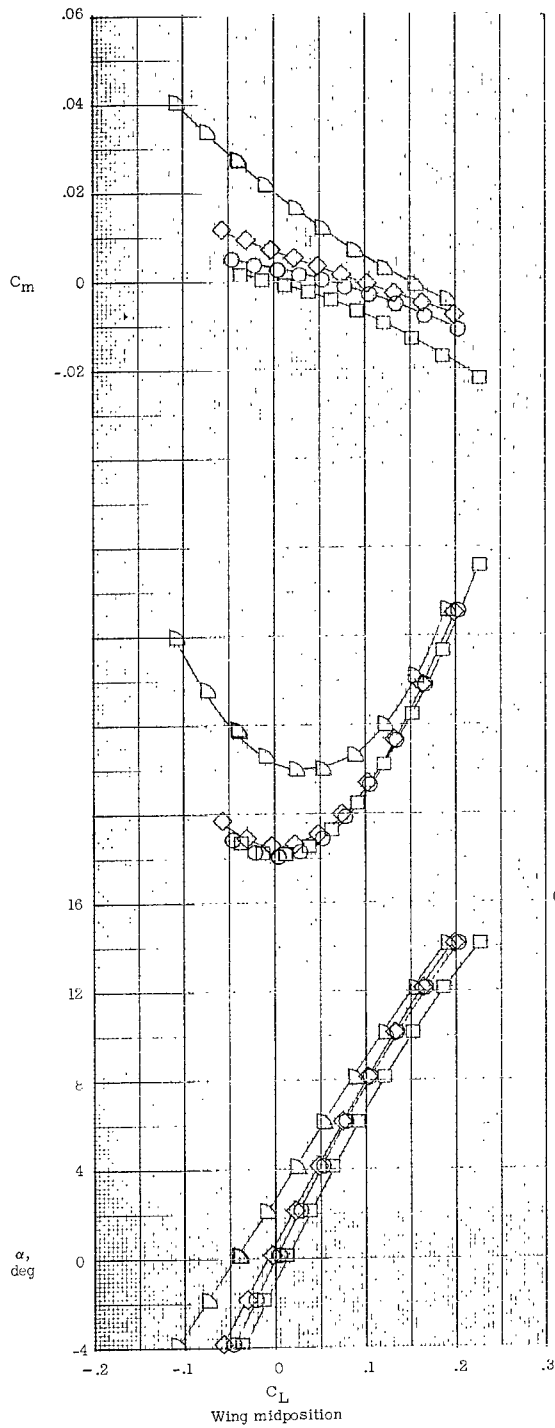
(b) $\delta_{N,2} = 2^\circ$.

Figure 34.- Continued.

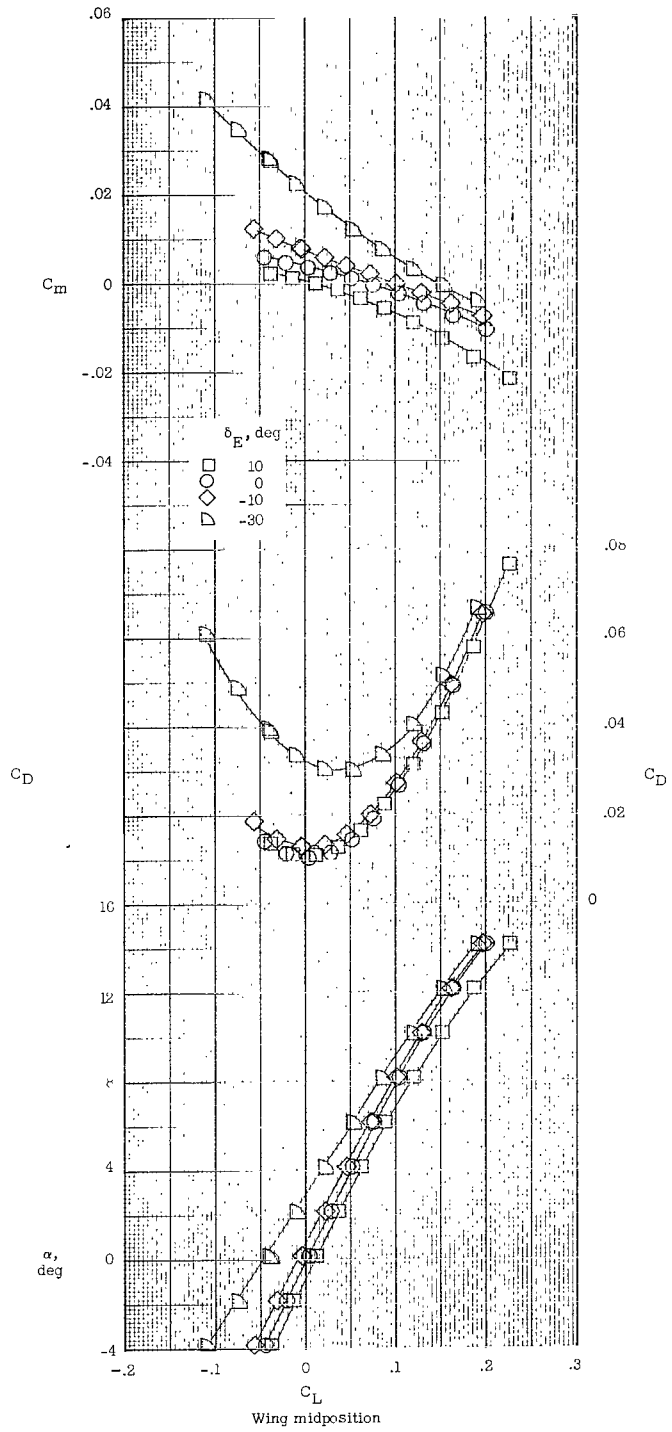


(c) $\delta_{N,2} = 4^\circ$.

Figure 34.- Continued.

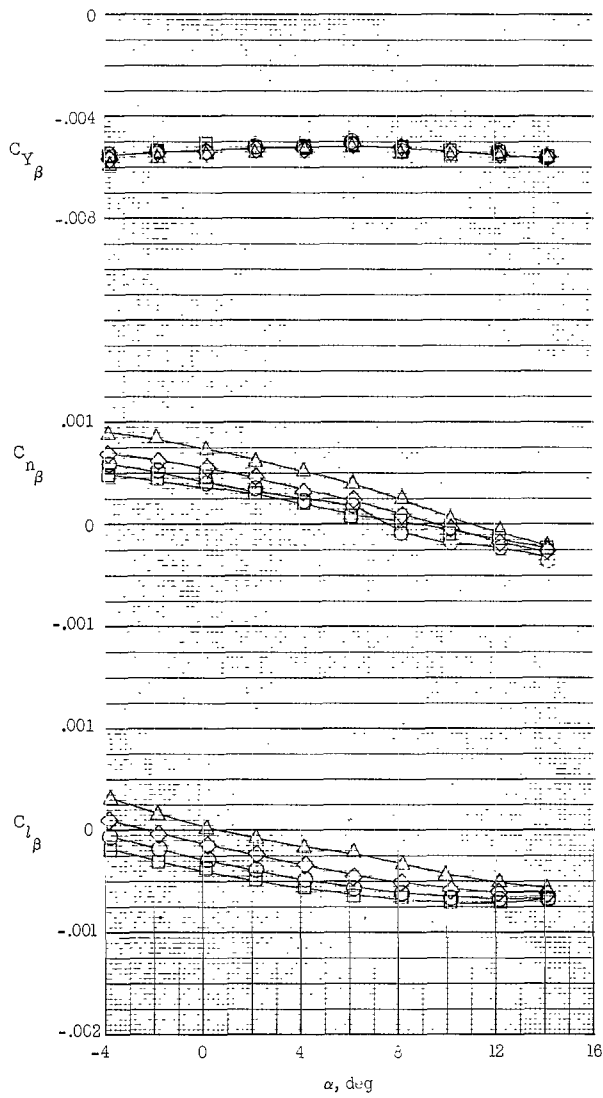


(d) $\delta_{N,1} = 2^\circ$.

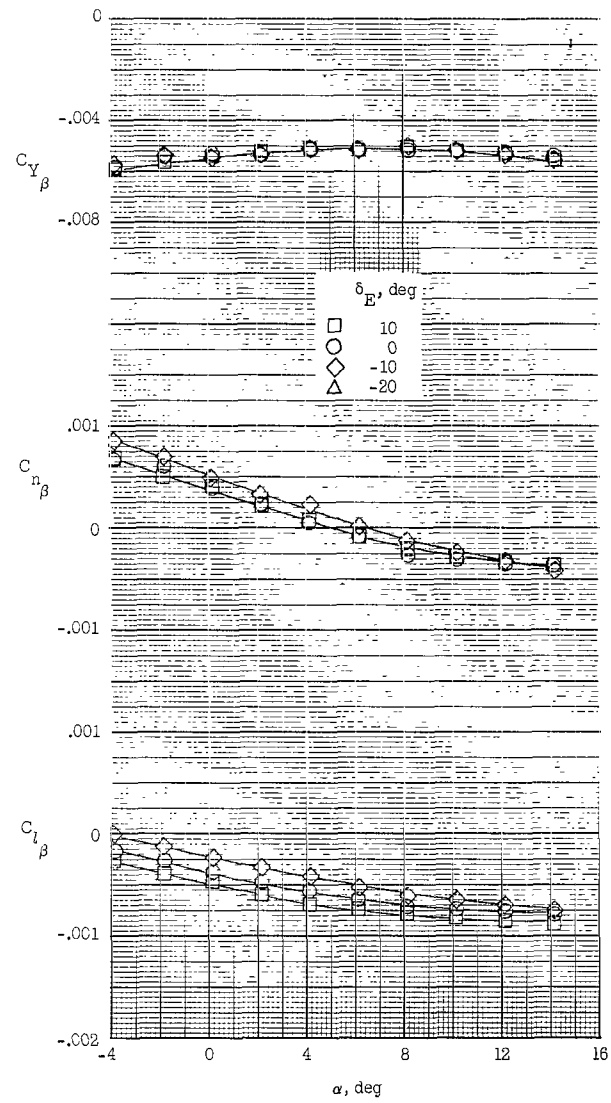


(e) $\delta_{N,1} = 4^\circ$.

Figure 34.- Concluded.

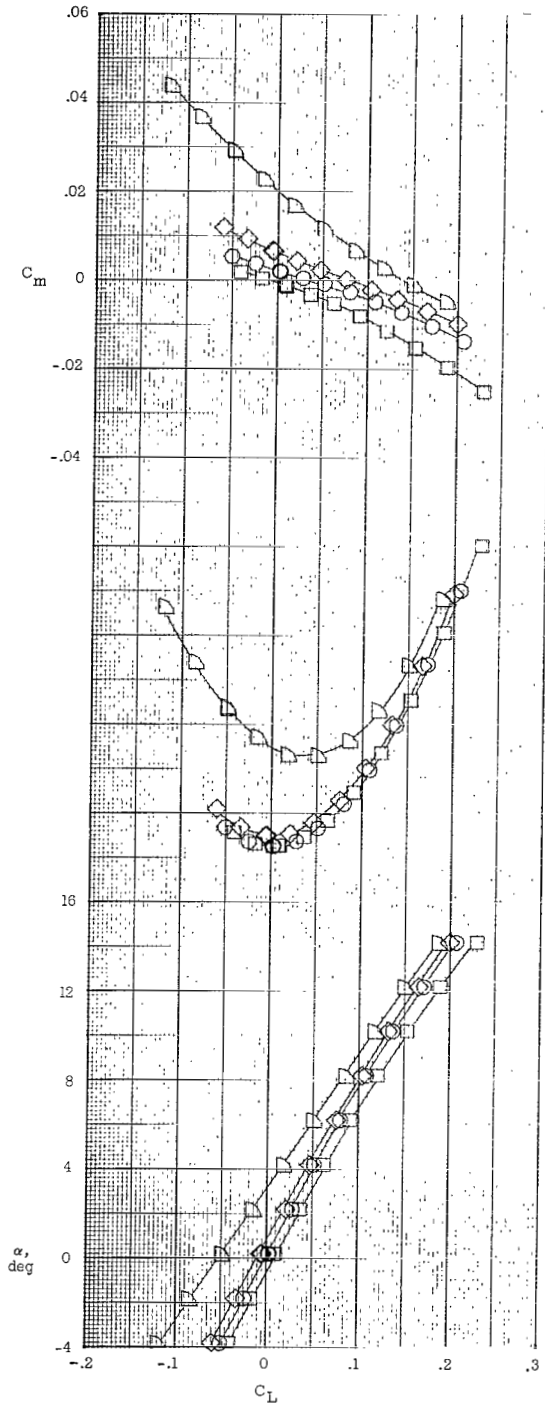


(a) $\delta_{N,2} = 0^\circ$.

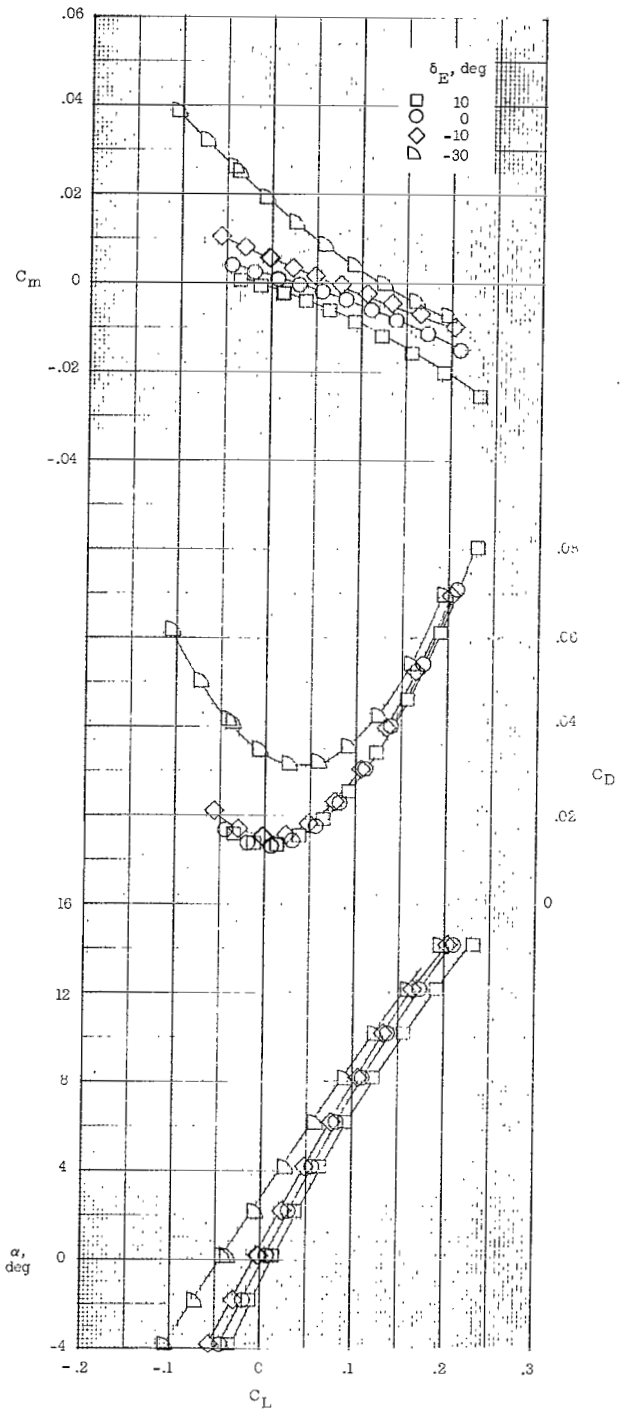


(b) $\delta_{N,2} = 4^\circ$.

Figure 35.- Effect of elevon deflection on lateral and directional stability characteristics of model 2, basic configuration with nose cant (BX3W3E3VU,2V,6). $M_\infty = 6$.

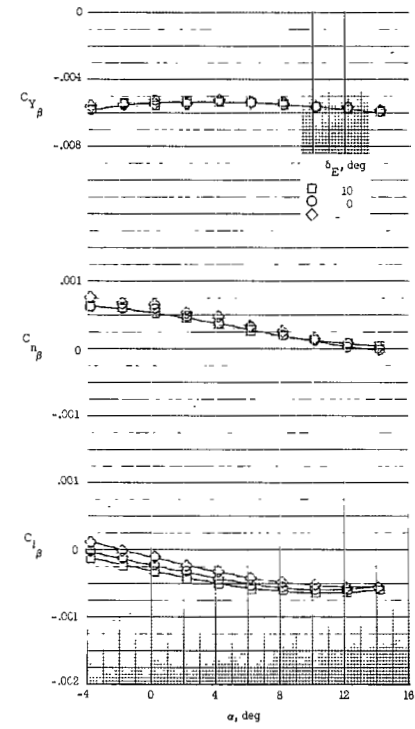
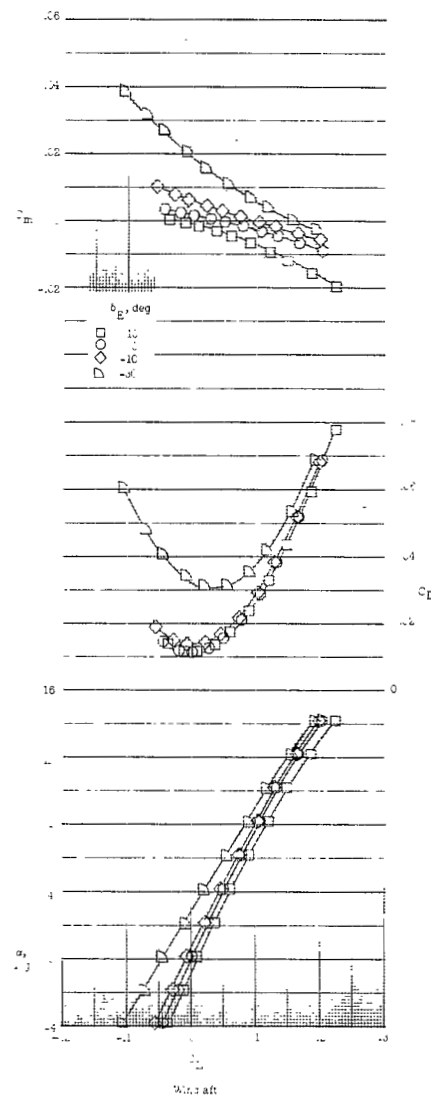
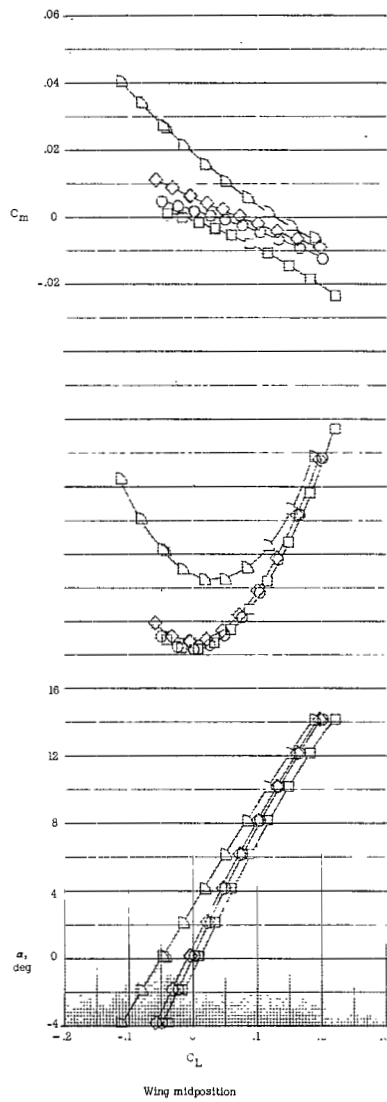


(a) $V_{T,6}$ (0° toe-in).



(b) $V_{T,7}$ (5° toe-in).

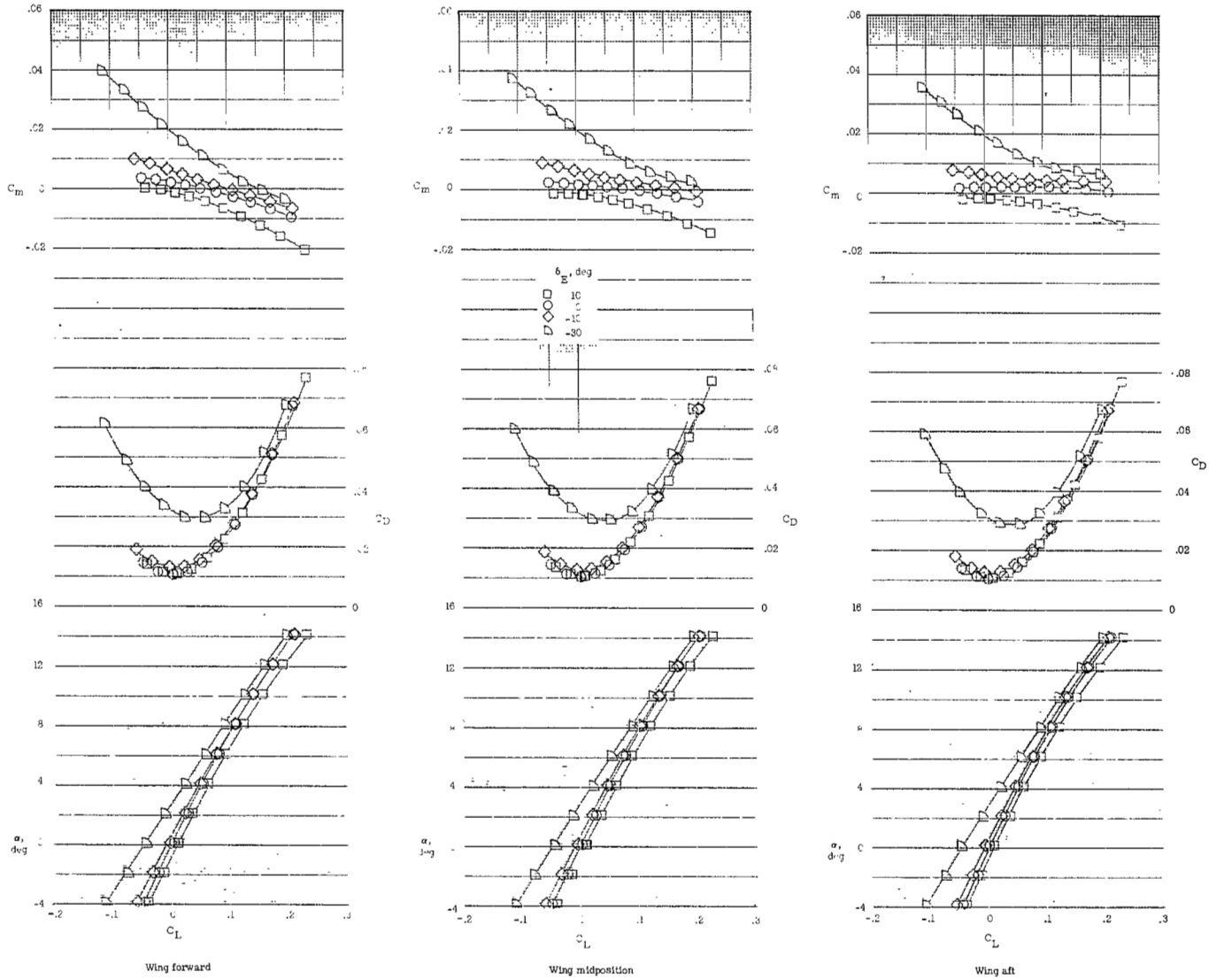
Figure 36.- Effect of elevon deflection on longitudinal aerodynamic characteristics of model 2, basic configuration with inboard fins ($BX_3W_3E_3V_{U,2}V_{L,6}V_T$) with wing in midposition. $M_\infty = 6$.



(a) Longitudinal characteristics.

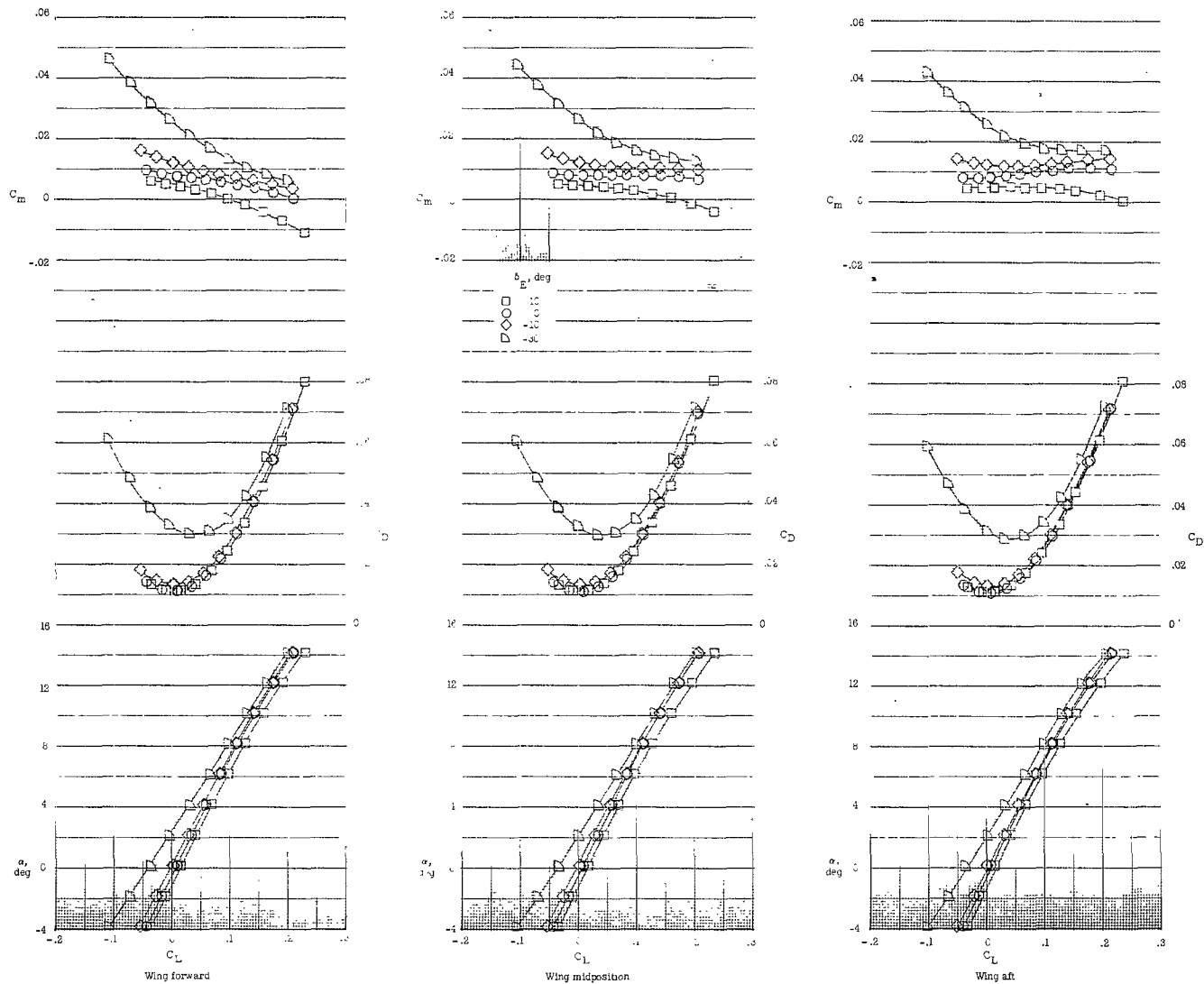
(b) Lateral and directional stability characteristics.

Figure 37.- Effect of elevon deflection on aerodynamic characteristics of model 2, basic configuration with ramjet (BX3W3E3VU,2VR,0). $M_\infty = 6$.



(a) $\delta_N = 0^\circ$.

Figure 38.- Effect of elevon deflection on longitudinal aerodynamic characteristics of model 2, basic configuration with strakes (B₂X₃W₃E₃V_{U,2}V_{L,6}). $M_\infty = 6$.



(b) $\delta_{N,2} = 4^\circ$.

Figure 38.- Concluded.

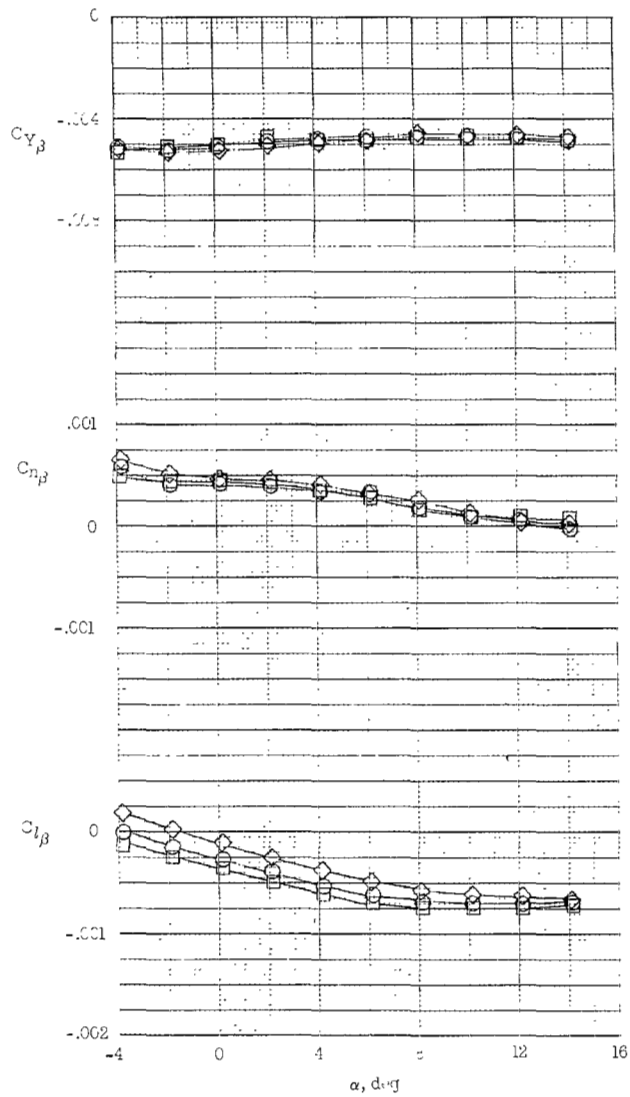
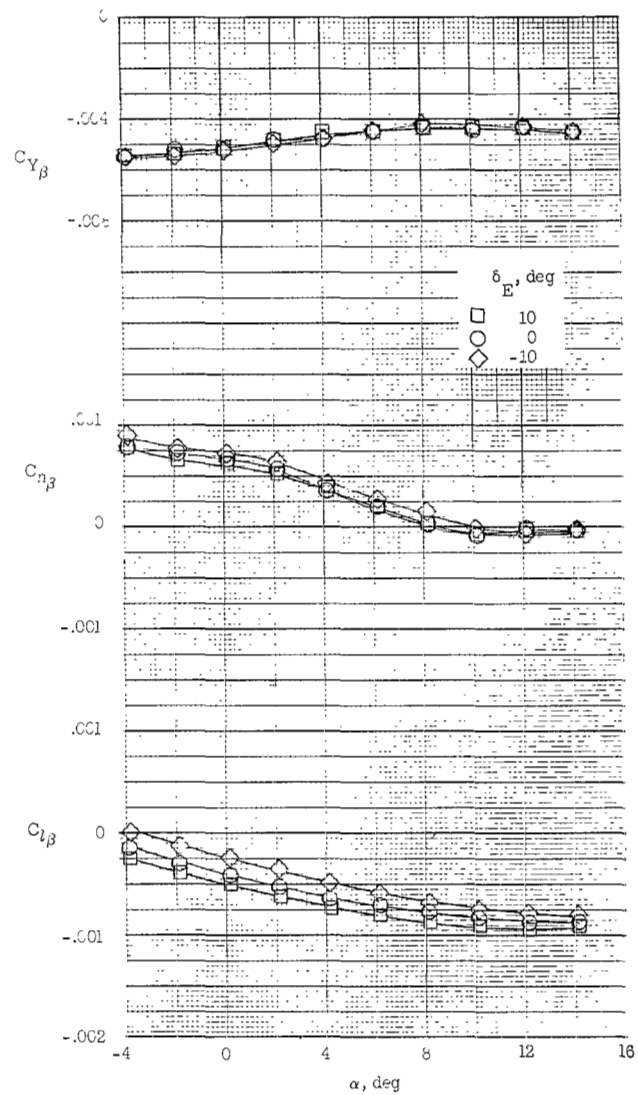
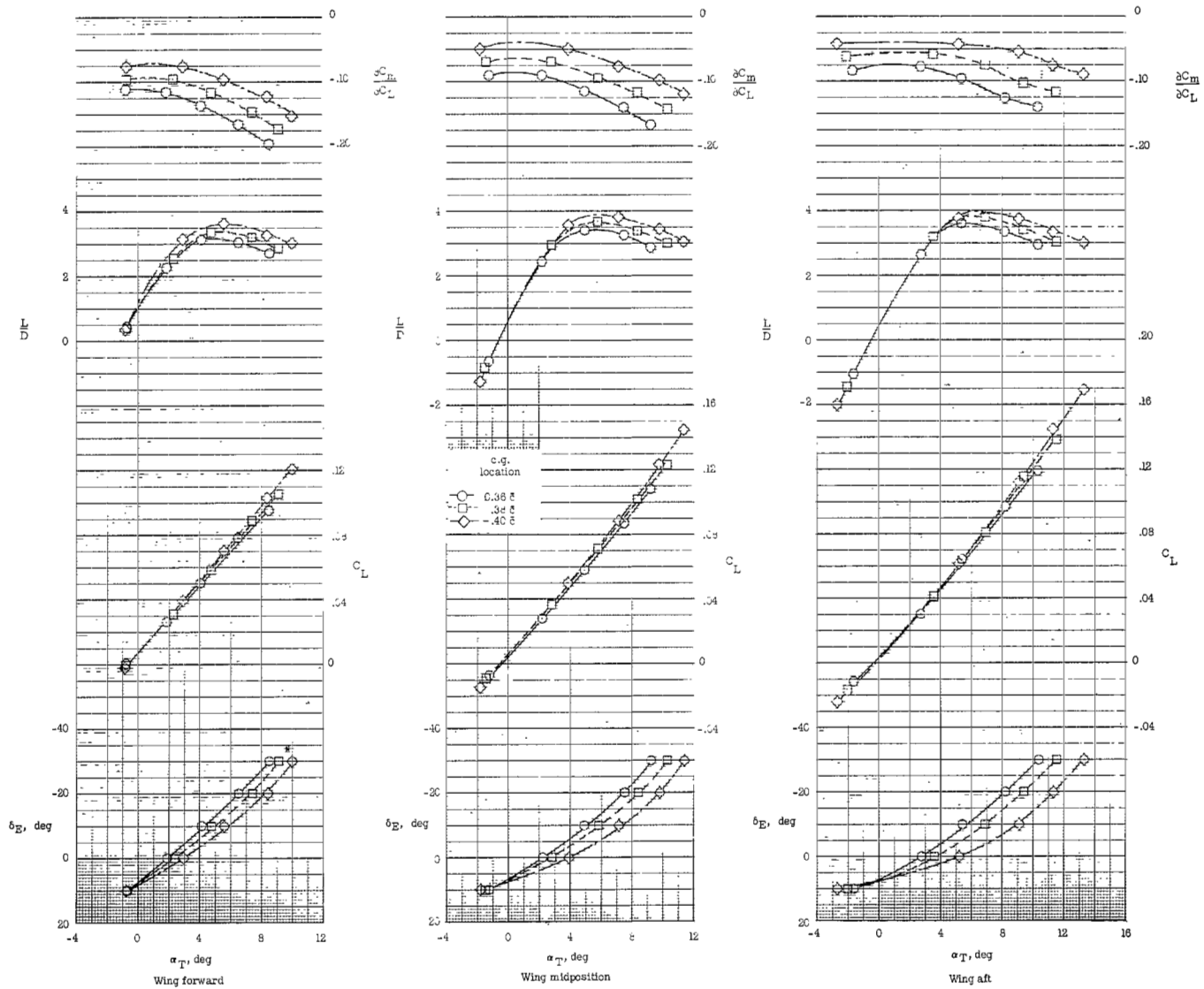
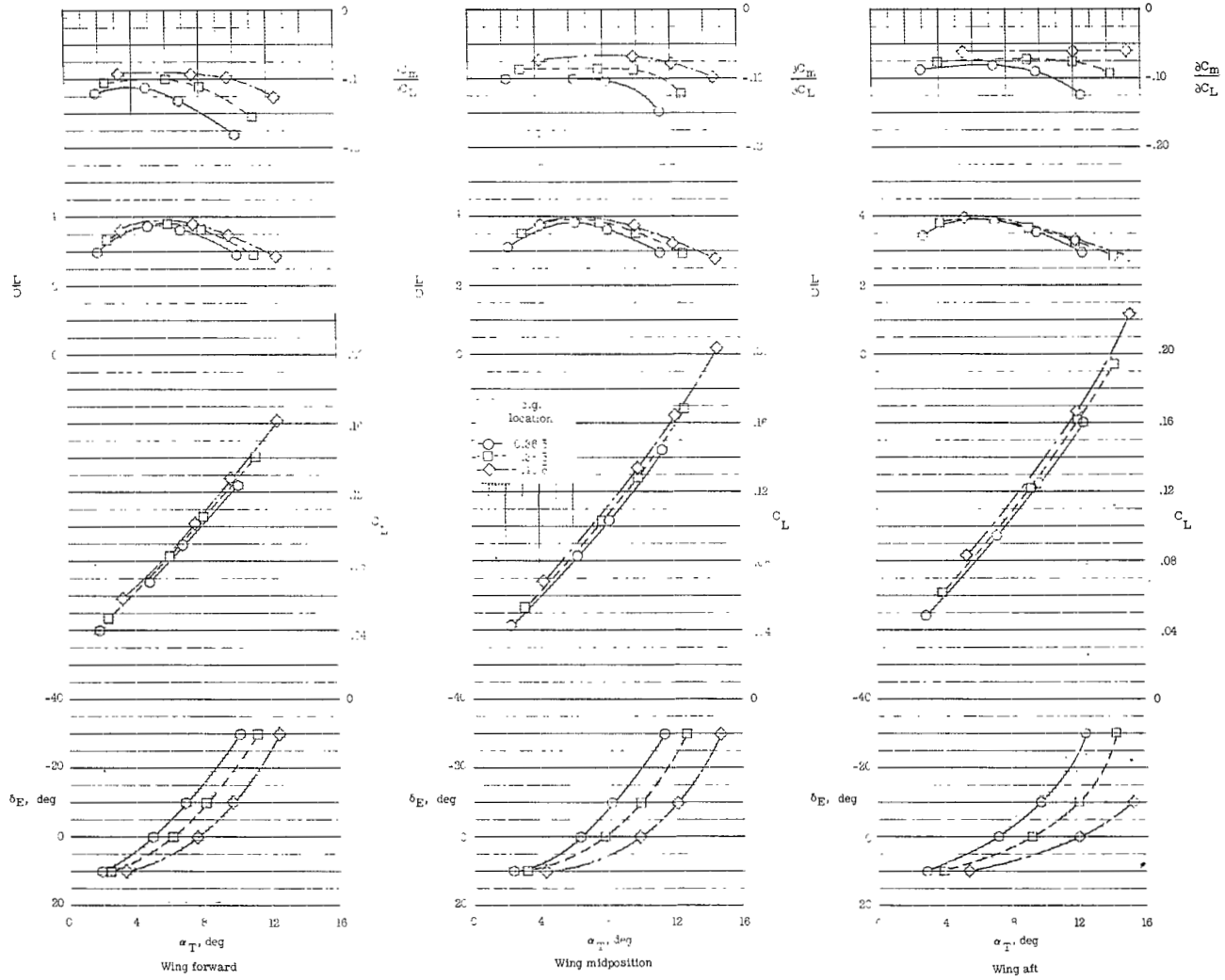
(a) $\delta_N = 0^\circ$.(b) $\delta_{N,2} = 4^\circ$.

Figure 39.- Effect of elevon deflection on lateral and directional stability characteristics of model 2, basic configuration with strakes ($B_2X_3W_3E_3V_{U,2}V_{L,6}$) with wing in aft position. $M_\infty = 6$.



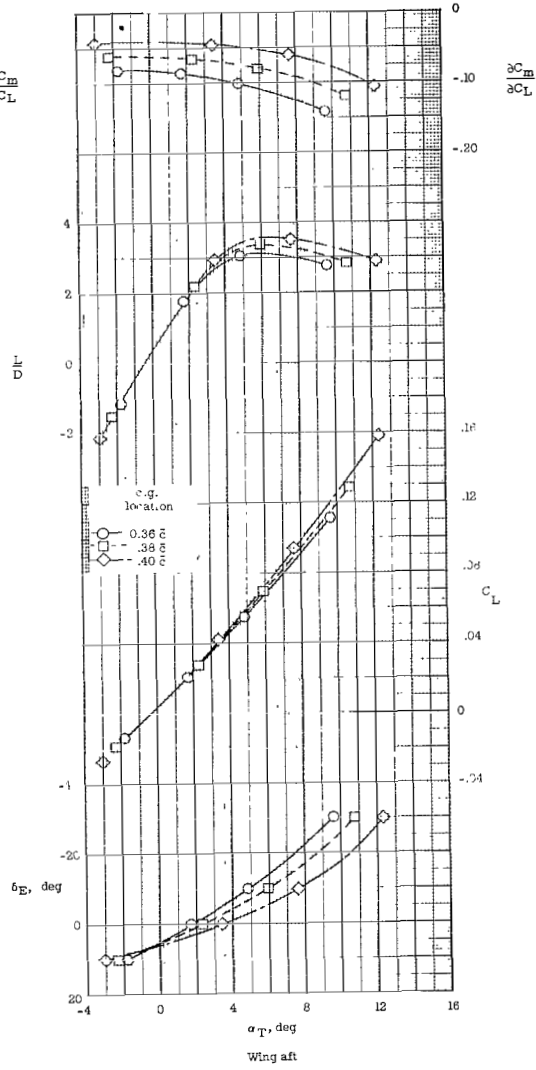
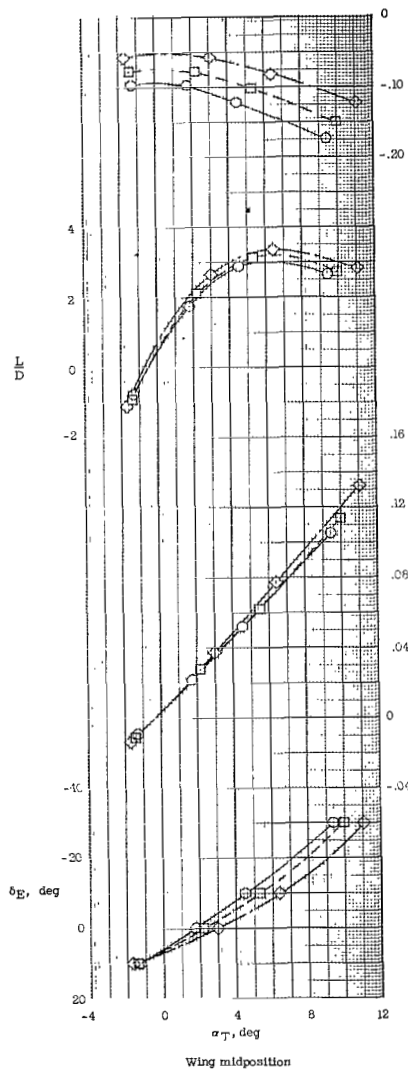
(a) Basic configuration (BX₃W₃E₃V_{U,2}V_{L,6}).

Figure 40.- Effect of center-of-gravity location on trimmed longitudinal aerodynamic characteristics of model 2. $M_\infty = 6$.



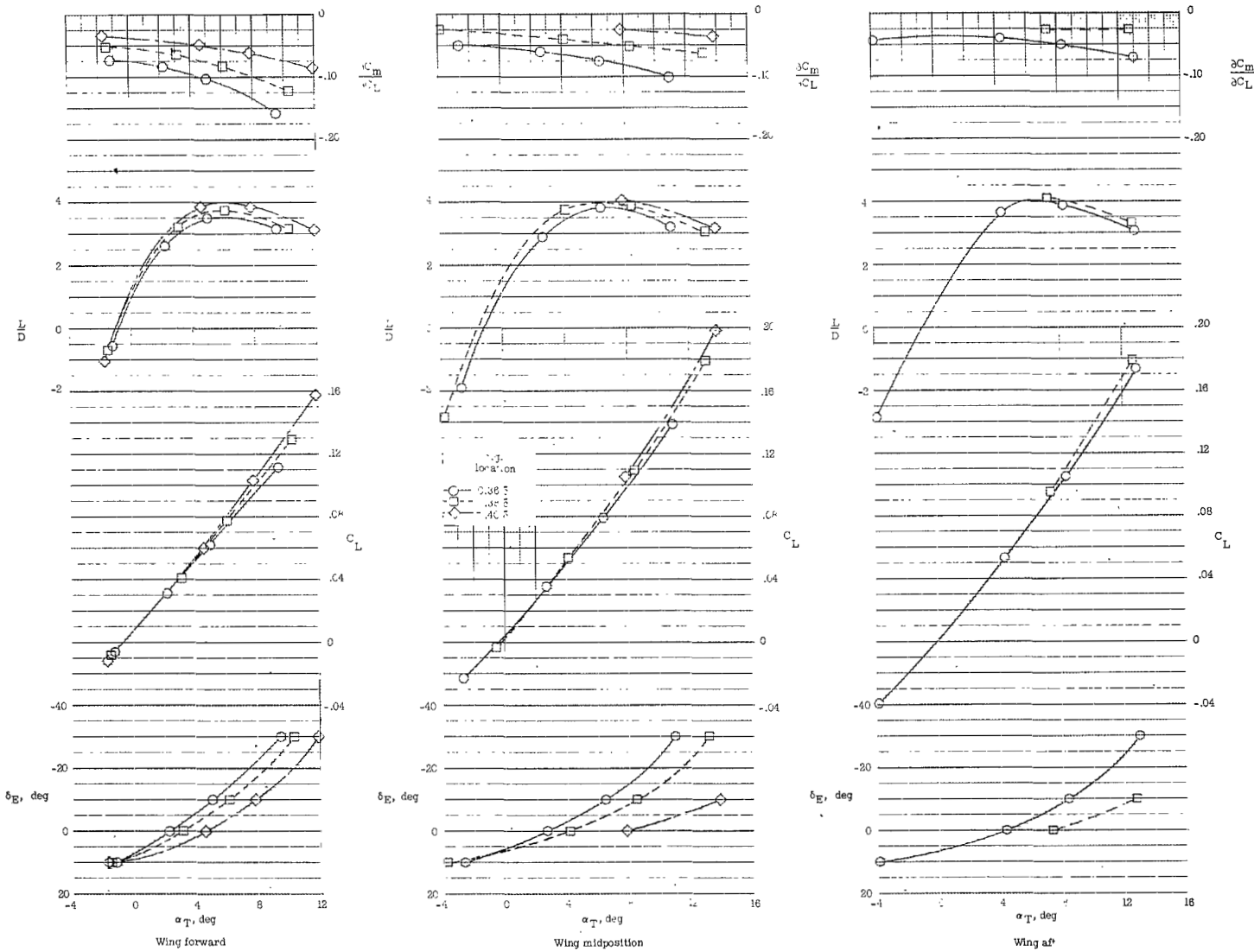
(b) BX₃W₃E₃V_{U,2}V_{L,6}; $\delta_{N,2} = 4^\circ$.

Figure 40.- Continued.



(c) BX₃W₃E₃V_{U,2}V_{R,0}

Figure 40.- Continued.



(d) $B_2X_3W_3E_3V_U, 2V_L, 6; \delta_N = 0^\circ$.

Figure 40.- Concluded.



041 001 26 51 305 69276 00904
AERONAUTICAL ENGINEERING LABORATORY/BL117
WRIGHT AIR FORCE BASE, NEW MEXICO 87117

POSTMASTER: If Undeliverable (Section 1
Postal Manual) Do Not Re

"The aeronautical and space activities of the United States shall be conducted so as to contribute . . . to the expansion of human knowledge of phenomena in the atmosphere and space. The Administration shall provide for the widest practicable and appropriate dissemination of information concerning its activities and the results thereof."

— NATIONAL AERONAUTICS AND SPACE ACT OF 1958

NASA SCIENTIFIC AND TECHNICAL PUBLICATIONS

TECHNICAL REPORTS: Scientific and technical information considered important, complete, and a lasting contribution to existing knowledge.

TECHNICAL NOTES: Information less broad in scope but nevertheless of importance as a contribution to existing knowledge.

TECHNICAL MEMORANDUMS: Information receiving limited distribution because of preliminary data, security classification, or other reasons.

CONTRACTOR REPORTS: Scientific and technical information generated under a NASA contract or grant and considered an important contribution to existing knowledge.

TECHNICAL TRANSLATIONS: Information published in a foreign language considered to merit NASA distribution in English.

SPECIAL PUBLICATIONS: Information derived from or of value to NASA activities. Publications include conference proceedings, monographs, data compilations, handbooks, sourcebooks, and special bibliographies.

TECHNOLOGY UTILIZATION PUBLICATIONS: Information on technology used by NASA that may be of particular interest in commercial and other non-aerospace applications. Publications include Tech Briefs, Technology Utilization Reports and Technology Surveys.

Details on the availability of these publications may be obtained from:

**SCIENTIFIC AND TECHNICAL INFORMATION DIVISION
NATIONAL AERONAUTICS AND SPACE ADMINISTRATION
Washington, D.C. 20546**